

New statistical techniques for the analysis of eruption data

Dissertation

zur Erlangung des Doktorgrades
der Mathematisch-Naturwissenschaftliche Fakultät
der Christian-Albrechts-Universität
zu Kiel

vorgelegt von
José Carlos Fontanesi Kling

Kiel
April 2025

- | | |
|---------------|-----------------------------|
| 1. Gutachter: | Prof. Dr. Mathias Vetter |
| 2. Gutachter: | Prof. Dr. Thorsten Dickhaus |

Tag der mündlichen Prüfung: 22. April 2025

Contents

Preface	1
1 Introduction	3
1.1 Models for eruption rates	5
1.2 Goodness-of-fit test for general point processes	6
1.3 Frequency analysis in event records	7
1.4 Evidence for coupling between glacial cycles and explosive eruptions in the Izu-bonin arc	8
1.5 Development of software packages for the analysis of point process data	10
2 A goodness-of-fit test for the analysis of the temporal distribution of explosive eruptions	17
2.1 Data	20
2.1.1 Tephra Data	20
2.1.2 Climate Proxy Data	21
2.2 Models for time dependent eruption rate	23
2.2.1 Model parametrization	24
2.3 Goodness-of-fit test	28
2.3.1 Testing conditional intensity function with known parameters	29
2.3.2 Testing conditional intensity function with unknown parameters	32
2.3.3 Simulation Tests	33
2.4 Results	35
2.4.1 Complete eruption record	35
2.4.2 Mafic and felsic eruptions	36
2.5 Discussion and closing remarks	38
2.5.1 Analysis of the results	38

2.5.2	Advantages and limitations of the methodology	40
2.5.3	Conclusion	41
3	On goodness-of-fit testing for self-exciting point processes	49
3.1	Setting	52
3.2	Results	55
3.3	Simulation study	61
3.3.1	Type I error	61
3.3.2	Power	62
3.4	Empirical application	64
3.5	Proofs	65
3.5.1	Proof of Lemma 3.2.3	65
3.5.2	Proof of Theorem 3.2.4	67
3.6	Omitted proofs	74
3.6.1	Proof of Lemma 3.5.1	74
3.6.2	Proof of Lemma 3.5.2	75
3.6.3	Proof of Lemma 3.5.5	75
3.6.4	Proof of Lemma 3.5.6	77
3.6.5	Proof of Lemma 3.5.7	78
3.6.6	Proof of Lemma 3.5.8	81
3.6.7	Proof of Theorem 3.5.9	84
4	Cyclicity and distinction of geological processes from thickness and frequency of event beds: A compilation of international drilling legacy datasets	93
4.1	Geological background	96
4.1.1	Montserrat, Lesser Antilles arc	99
4.1.2	Izu arc	99
4.1.3	Kyushu-Palau ridge	100
4.1.4	Gran Canaria, Canarian archipelago	102
4.2	Materials and methods	103
4.2.1	Rationale of event bed discrimination	103
4.2.2	Data quality check - validity rates of sediment records . . .	103
4.2.3	Data processing	104
4.2.4	Statistical analyses	105
4.3	Results	107
4.3.1	Logistics of data set grouping	107
4.3.2	Box-and-whisker plot	115

4.3.3	Scatter plots with marginal histograms	115
4.3.4	Thickness-frequency distributions	116
4.3.5	T-test analysis	117
4.3.6	Time-dependent frequency analysis	118
4.4	Discussion	119
4.4.1	Factors that can modify thickness-frequency distributions .	119
4.4.2	Implications of the t-test analysis	122
4.4.3	Alternative interpretations for differences in thickness-frequency distributions	125
4.4.4	Periods of event frequency	126
4.5	Conclusions	128
5	Conclusion	147
5.1	Analysis of additional eruption records	148
5.2	Models including underreporting	148
5.3	Test for marked point processes	149

Acknowledgments

First and foremost, I want to thank my supervisors, Mathias Vetter and Julie Belo. Their support and commitment to this work were essential. I appreciate that they have always been open and encouraging of my ideas and placed a lot of trust in what I do. Lastly, I am thankful that they took a chance on me for this project, and I hope it was a rewarding experience for them as well.

I also thank the support from Marion Jegen and Steffen Kutterolf. Our numerous meetings and discussions were very helpful, and I appreciate all the revisions and help with defending this work, which was probably more needed than we had hoped.

The MarDATA School for Marine Data Science is what made this project possible, and I am glad to be a part of it. In special, I want to thank Enno Prigge for all the encouragement and for always being there for us students. I hope his efforts for the school continue to pay off.

In short, I am grateful for having the opportunity to work on this project. I not only learned a lot from different (and unexpected) topics, but enjoyed working on it and with all the people involved. Hopefully the end of this project is the beginning of other collaborations.

Abstract

This thesis is composed of three independent manuscripts. The common thread among them is the goal to improve and expand on the limited statistical methods available in the literature for the analysis of the temporal distribution of volcanic eruptions, especially when assessing if it is influenced by external factors, such as climate proxies.

The first manuscript (Section 2) aims to present some of our newly developed methodology with an application to the analysis of the eruption record derived from IODP Hole 350-1437B, from the Izu-Bonin arc, in conjunction with the LR04 $\delta^{18}O$ global stack as a climate proxy. Based on point processes, we develop models for eruption rate that incorporate information from external factors and propose a novel bootstrap based goodness-of-fit test for parametric point processes. This test is used to evaluate the hypothesis that the $\delta^{18}O$ record affects the occurrence of eruptions, and the results suggest that the response to climate change may depend significantly on the magma composition of the events.

The second manuscript (Section 3) provides the mathematical theory behind the goodness-of-fit test mentioned above. Based on recently developed bootstrap techniques and previous works on the asymptotic normality of the maximum likelihood estimator for point processes, the consistency of our test can be proved for the class of inhomogeneous Poisson processes. Nevertheless, it has been empirically verified that this procedures is valid for a much broader range of processes.

The third, and last, manuscript (Section 4) analyzes the thickness and frequency of event beds from different sites to assess possible physical mechanisms modulating their distributions. In particular, the detection of periodicities in the event bed records were evaluated using methods developed in this project, leveraging the use of simulation to address the significance of the findings.

The methodological advancements achieved during this project, with foundations on sound statistical theory, have been shown to significantly improve the robustness of results when compared to existing methods. Moreover, as a mathematical abstrac-

tion, they can be applied to a broad range of areas, with virtually no restrictions on time scale nor on which functions can be incorporated as possible external factors. Additionally, the implementations of these procedures are openly available for the general scientific community.

Zusammenfassung

Diese Arbeit besteht aus drei unabhängigen Manuskripten. Ihr gemeinsamer Nenner ist das Ziel, die begrenzten statistischen Methoden, die in der Literatur für die Analyse der zeitlichen Verteilung von Vulkaneruptionen zur Verfügung stehen, zu verbessern und zu erweitern, insbesondere wenn es darum geht, zu beurteilen, ob sie von externen Faktoren, wie z. B. Klimaproxies, beeinflusst wird.

Das erste Manuskript (Abschnitt 2) zielt darauf ab, einige unserer neu entwickelten Methoden mit einer Anwendung auf die Analyse der Eruptionsaufzeichnungen aus dem IODP-Loch 350-1437B aus dem Izu-Bonin-Bogen in Verbindung mit dem LR04 $\delta^{18}O$ Global Stack als Klimaproxy vorzustellen. Auf der Grundlage von Punktprozessen entwickeln wir Modelle für die Eruptionsrate, die Informationen von externen Faktoren einbeziehen, und schlagen einen neuartigen Bootstrap-basierten Goodness-of-fit-test für parametrische Punktprozesse vor. Dieser Test wird verwendet, um die Hypothese zu bewerten, dass der $\delta^{18}O$ -Datensatz das Auftreten von Eruptionen beeinflusst, wobei wir zu dem Eindruck kommen, dass die Reaktion auf den Klimawandel wesentlich von der Magmazusammensetzung der Ereignisse abhängen könnte.

Das zweite Manuskript (Abschnitt 3) liefert die mathematische Theorie hinter dem oben erwähnten Goodness-of-fit-test. Auf der Grundlage kürzlich entwickelter Bootstrap-Techniken und früherer Arbeiten über die asymptotische Normalität des Maximum-Likelihood-Estimators für Punktprozesse kann die Konsistenz unseres Tests für die Klasse der inhomogenen Poisson-Prozesse nachgewiesen werden. Es wurde zudem empirisch überprüft, dass dieses Verfahren für eine viel breitere Palette von Prozessen gültig ist.

Das dritte und letzte Manuskript (Abschnitt 4) analysiert die Mächtigkeit und Häufigkeit von Ereignisbetten an verschiedenen Standorten, um zu bewerten, inwieweit mögliche physikalische Mechanismen ihre Verteilungen modulieren. Insbesondere wurde die Erkennung von Periodizitäten in den Ereignisbettaufzeichnungen mit Hilfe von Methoden bewertet, die im Rahmen dieses Projekts entwickelt

wurden, wobei die Signifikanz der Ergebnisse durch den Einsatz von Simulationen untersucht wurde.

Die im Rahmen dieses Projekts erzielten methodischen Fortschritte, die sich auf eine solide statistische Theorie stützen, verbessern nachweislich die Robustheit der Ergebnisse im Vergleich zu bestehenden Methoden erheblich. Darüber hinaus können sie aufgrund der mathematischen Abstraktion auf ein breites Spektrum von Bereichen angewandt werden, wobei es praktisch keine Einschränkungen hinsichtlich der Zeitskala oder der Funktionen gibt, die als mögliche externe Faktoren einbezogen werden können. Darüber hinaus ist die Implementierung dieser Verfahren für die allgemeine wissenschaftliche Gemeinschaft offen zugänglich.

Preface

This thesis is the result of the project originally named ‘links between climate and volcanism’, carried out in the context of MarDATA - Helmholtz School for Marine Data Science. The goal of the school is to train scientists in the frontier between data science and the domain sciences, therefore, this work was supervised by two researchers. Julie Christin Belo, researcher at GEOMAR in the field of Volcanology, and Mathias Vetter, professor of mathematical statistics at Kiel University.

This is a cumulative work, containing three manuscripts with direct results from the project. These are preceded by an introduction, where I map some of the important works related to the analysis of the temporal distribution of eruptive events and briefly present the contributions developed in this project. The conclusions close the thesis, and briefly describes possible extensions of our results.

The following three manuscripts are included here. I, together with the other authors, contributed with the conceptualization of the methods, while I was the main responsible for their implementation and testing. In the first manuscript, I am the main writer. In the second, I was in charge of the proofs for Lemma 3.2.3 and Sections 3.3 and 3.4. For the third, I substantially contributed with the sections on the frequency analysis of the data and the writing of the manuscript.

1. **Kling, J.C.F.**, Schindlbeck-Belo, J.C., Vetter, M., Jegen, M., Kutterolf, S. (submitted to *Volcanica*) **A goodness-of-fit test for the analysis of the temporal distribution of explosive eruptions**
2. **Kling, J.C.F.**, Vetter, M. (2024 - Preprint - submitted to *Scandinavian Journal of Statistics*) **On goodness-of-fit testing for self-exciting point processes**
3. Chang, Y., **Kling, J.C.F.**, Schindlbeck-Belo, J.C., Mitchel, N., Hsiung, K., Kanamatsu, T. (to be submitted) **Cyclicity and Distinction of Geological Processes from Thickness and Frequency of Event Beds: A Compilation of International Drilling Legacy Datasets**

In addition to these works, I also participated as coauthor in Cisneros de León et al. (2023), contributing with the statistical analysis and writing of the Section ‘eruption recurrence intervals’.

Lastly, two software packages were implemented and are openly available at GEOMAR repository OceanRep. The first is a package for MATLAB (The MathWorks Inc., 2022), covering all necessary procedures to apply the goodness-of-fit test from Section 2.3 to the models described in Section 2.2 (Kling et al., 2023). The second is an implementation for the Julia programming language (Bezanson et al., 2017), including all the methods from the MATLAB package and the method for detection of periodicities described in Section 4.3.6 (Kling et al., 2024).

This study was funded through the Helmholtz School for Marine Data Science (MarDATA), Grant No. HIDSS-0005.

References

- Jeff Bezanson, Alan Edelman, Stefan Karpinski, and Viral B Shah. Julia: A fresh approach to numerical computing. *SIAM Review*, 59(1):65–98, 2017. doi: 10.1137/141000671. URL <https://epubs.siam.org/doi/10.1137/141000671>.
- A. Cisneros de León, M. Danišík, J.C. Schindlbeck-Belo, S. Kutterolf, A.K. Schmitt, A. Freundt, J. Kling, K.-L. Wang, and H.-Y. Lee. Timing and recurrence intervals for voluminous silicic eruptions from amatitlán caldera (guatemala). *Quaternary Science Reviews*, 301:107935, February 2023. ISSN 0277-3791. doi: 10.1016/j.quascirev.2022.107935.
- José Kling, Mathias Vetter, Julie Schindlbeck-Belo, Marion Jegen, and Steffen Kutterolf. Pointprocesstools (software), 2023.
- José Kling, Mathias Vetter, Julie Schindlbeck-Belo, Marion Jegen, and Steffen Kutterolf. Pointprocesstools.jl (software), 2024.
- The MathWorks Inc. Matlab version: 9.13.0 (r2022b), 2022. URL <https://www.mathworks.com>.

Chapter 1

Introduction

It is well known that large volcanic eruptions can impact local and global climate (Robock, 2000). One of the most well studied example of this phenomenon is the 1991 eruption of Mount Pinatubo, which ejected an estimated 20 million tons of SO_2 into the stratosphere (Molineaux and Ineichen, 1996) and caused a decrease in the global mean air temperature of 0.2° to 0.5° lasting from 12 to 36 months after the eruption (Parker et al., 1996; Boretti, 2024).

In contrast, the effect of climate on the occurrence of large explosive eruptions is a relatively recent and controversial topic. One of the first works to suggest that climatic change may cause volcanic eruptions is Rampino et al. (1979), which compiled the timings of major explosive eruptions and observed that many of them occurred after a cooling trend was already initiated and suggested that cooling periods may favor volcanism, opposing the hypothesis of major eruptions as drivers of global glaciation.

Analysis of local records from Iceland (Sigvaldason et al., 1992), Alaska (Praetorius et al., 2016), and Chile (Rawson et al., 2016) show increased volcanic activity following the last deglaciation compared to the last millennia. All these regions have been glaciated, indicating that the retreat of ice sheets might be a important modulator for the occurrence of eruptions. Supporting evidence from a global compilation is given in Huybers and Langmuir (2009), which detected a 2 to 6 times increase in volcanism during the last deglaciation, mainly driven by previously glaciated regions, although a critical reexamination in Watt et al. (2013) questioned the significance of the results.

A number of works resorted to records covering multiple glacial cycles to better assess the relation between volcanism and climate. Paterne et al. (1990), Jellinek et al. (2004) and Schindlbeck et al. (2018) show periodicities in local eruption

records coinciding with the Milankovitch cycles of precession (23 kyr), obliquity (41 kyr) and eccentricity (100 kyr), respectively, while Kutterolf et al. (2013) observed a 41 kyr cyclicity in records compiled from the Pacific Ring of Fire. In these works the methodological approach is to first apply a filter to the eruption records, such as a moving average, to transform the data into a proper continuous time series, then assess the frequency content of this new series via standard Fourier transforms.

More direct correlations between eruption timing and climate records are presented in Glazner et al. (1999) and Nowell et al. (2006). These works compared the values of $\delta^{18}O$ isotope ratios at the times of the events with those of simulated random datasets. Most notably, Nowell et al. (2006) observed a significant correlation between timing of eruptions in Western Europe and the slope of the $\delta^{18}O$ record, that is, the rate of change in temperature, specifically during the onset of interglacial periods.

The statistical methods employed in the works mentioned above differ greatly due to the lack of specific procedures for testing the influence of external factors on eruption rate. Additionally, there is usually no explicit formal models for the timing of eruptions, making it less clear how all these methods relate to each other. A possible unifying framework is the concept of point processes. The idea of modeling eruption records as point processes is not new and is used extensively in the literature (e.g., De la Cruz-Reyna, 1991; Bebbington, 2013; Ignatieva et al., 2018; Selva et al., 2022; Deligne et al., 2010), although not for our specific context, in which the effect of some external function must be accounted for.

The primary aim of these studies is to estimate how the eruption rate changed over time and test whether this estimation is actually compatible with the data. Among the most widely used approaches is a Kolmogorov-Smirnov type statistic presented in Ogata (1988) (e.g., Bebbington, 2010; Bevilacqua et al., 2016; Marzocchi and Bebbington, 2012; Bantidi and Mavonga, 2023). These methods, however, fail to account for estimation errors, which may significantly affect their reliability (see Babu and Rao, 2004). A sound goodness-of-fit test has been, so far, missing in the literature, as pointed out by Ogata (1988) and Chen and Hall (2013).

This project aims to solve some of the methodological limitations from the aforementioned works and reanalyze the eruption record derived from the IODP Hole 350-U1437B (Tamura et al., 2015) in conjunction with the LR04 $\delta^{18}O$ global stack as a global ice cover proxy. In the following items, we provide a brief presentation of the main research contributions of this project.

1.1 Models for eruption rates

The use of point processes to model eruption records is not new in the literature (see Bebbington, 2013, for an overview). When assessing the temporal distribution of eruptions, many works resort to renewal models (e.g., Bantidi and Mavonga, 2023; Ignatieva et al., 2018; Bebbington, 2010; Sandri et al., 2021), although some have considered Poisson (e.g., De la Cruz-Reyna, 1991; Deligne et al., 2010), inhomogeneous Poisson (Ho et al., 1991), and Hawkes processes (Bevilacqua et al., 2016) as well. However, none of these works incorporate external data, such as climate proxy, into the models.

Our solution is to extend the Poisson and Hawkes models, adding a parameter γ to their conditional intensity functions that quantify the process' dependency on some arbitrary function f . In the following, f will denote a function with $\min(f) = 0$ and $\max(f) = 1$. Notice, however, that any bounded function can be used by first applying the normalization $\frac{f(t) - \min(f)}{\max(f) - \min(f)}$.

For the Poisson process, the conditional intensity function, which in our context can be understood as eruption rate, is constant, therefore, can be modeled by a single parameter μ defining the intensity function $\lambda(t) = \mu$. By adding the term $\gamma f(t)$, the model has now two components, one constant baseline rate μ which is independent of the external factor f , and a second one in which the parameter γ directly quantifies the process' dependency on f . These processes, in which the conditional intensity function are deterministic, but vary over time, are known as inhomogeneous Poisson processes.

The same strategy can be applied to Hawkes processes. If (t_1, t_2, \dots) are events, then the intensity of the process is given by $\lambda(t) = \mu + \sum_{t_i < t} \alpha e^{-\beta(t_i - t)}$. Here, events occur at a constant rate μ , but each of them trigger subsequent events, the strength of this response being controlled by the parameters α and β . Adding $\gamma f(t)$ to the intensity function simply makes the rate of occurrence dependent of the external factor, while maintaining the triggering component unchanged.

Figure 1.1 illustrate the four models used in this project. On the left panes are the Poisson and Hawkes process, and on the right their modified versions, with the term $\gamma f(t)$ added. In all plots the values used for the parameters are $\mu = 0.05$, $\gamma = 0.05$, $\alpha = 0.05$ and $\beta = 0.3$, with $f(t)$ as the $\delta^{18}O$ climate proxy record for the last 500 kyr.

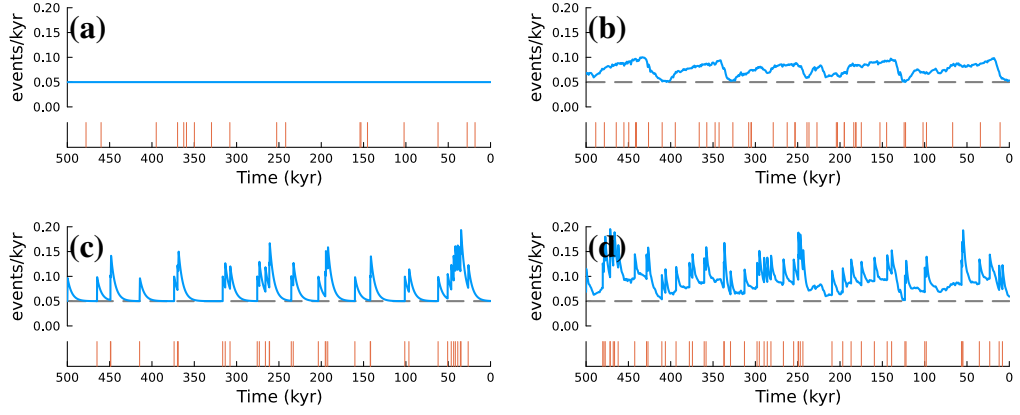


Figure 1.1: Four different models for eruption rate and simulated events over an interval of 500 kyr. **(a)** Homogeneous Poisson process, **(b)** inhomogeneous Poisson process, **(c)** Hawkes process, and **(d)** inhomogeneous Hawkes process. Grey line in panes **(b)**, **(c)** and **(d)** correspond to the constant component μ .

1.2 Goodness-of-fit test for general point processes

Probably the main contribution of our work is the development of a general goodness-of-fit test for point processes that can properly maintain a uniform α -level.

Ogata (1988) introduced methods based on residual analysis to assess the quality of fit of Hawkes processes to seismological data. It relies on the fact that, if a process $N(t)$ is known to have corresponding conditional intensity function $\lambda_0(t)$ and (t_1, \dots, t_N) denote the event times, then the random variables $X_i = \int_{t_{i-1}}^{t_i} \lambda_0(t) dN(t)$ with $t_0 = 0$ follow a unit exponential distribution.

Let λ_0 denote the true conditional intensity function of the process that generated the events at time (t_1, \dots, t_N) . Assume we want to test the hypothesis H_0 : There exist parameters θ such that $\lambda_0(t) = \lambda(t; \theta)$. One possible procedure, which resembles procedures found in, e.g., Ogata (1988). Bebbington (2010) and Bantidi and Mavonga (2023), is to estimate the parameters from the data, resulting in, say, $\hat{\theta}$, then apply the Kolmogorov-Smirnov test to the random variables $\int_{t_{i-1}}^{t_i} \lambda(t; \hat{\theta}) dN(t)$ against a unit exponential distribution, resulting in a p-value for the hypothesis H_0 . This procedure, however, has the limitation that it does not account for parameter estimation error, potentially leading to bias and incorrect results (Babu and Rao, 2004).

Building on theoretical results on the asymptotic normality of the maximum likelihood estimator from Chen and Hall (2013) and incorporating recent bootstrap techniques from Cavaliere et al. (2023), we were able to develop a consistent goodness-of-fit test for parametric point process models (see Sections 2.3 and 3).

Although formal proofs are provided only in the inhomogeneous Poisson cases, simulation studies show that this procedure is effective for a much broader range of models, including renewal processes (Bebbington, 2013) and the two-state model (Selva et al., 2022).

1.3 Frequency analysis in event records

The frequency content of eruption records have been previously analyzed in, e.g., Schindlbeck et al. (2018) and Paterne et al. (1990). Both works resorted to applying a moving average filter to the event record, resulting in a continuous time function, and then using standard procedures based on the Fourier transform. However, this procedure adds some arbitrariness to the analysis, both from the type of filtering (e.g., moving average, Gaussian kernel) and from the width of the filter window.

One way to remedy this is to follow Bartlett (1963). Essentially, the eruption record is modeled as a continuous time series in which events are represented as Dirac- δ functions, i.e., if the events occur at times (t_1, \dots, t_N) over a time interval of length T , then we get the time series $S(t) = \sum_{i=1}^N \delta(t - t_i)$. It can be shown that the Fourier transform of $S(t)$ is defined as $\mathcal{F}_S(\omega) = \sqrt{\frac{2}{T}} \int_{-\infty}^{\infty} S(t) e^{-i2\pi\omega t} dt$, therefore, the power spectrum of $S(t)$ can be calculated as

$$PS_S(\omega) = \left| \int_{-\infty}^{\infty} \sqrt{\frac{2}{T}} S(t) e^{-i2\pi\omega t} dt \right|^2 = \frac{2}{T} \left| \sum_{i=1}^N e^{-i2\pi\omega t_i} \right|^2. \quad (1.1)$$

This procedure has the following advantages over the previous method of transforming the event record into a continuous time series. (1) It completely bypasses the need for filtering, (2) it is more efficient, because the function $e^{-i2\pi\omega t}$ is calculated only at times (t_1, \dots, t_N) and, since there cannot be more cycles than events, only for $\omega \leq T/N$, and (3) it is more accurate, since the integrals in Equation 1.1 are calculated exactly, and not by numerical methods. Notice also that, if the frequency response of the filtered events is still needed, it can still be efficiently calculated by applying the filter's frequency response, provided it is known, to the result of the Fourier transform.

The significance of the resulting frequency response can be assessed through simulations. In Section 4.3.6 it is proposed that the power spectrum of the data should be compared with the responses from simulated Poisson processes. More specifically, periodicities are only considered relevant if a comparable response occurs in less than a fixed fraction of the simulated processes, usually set to be 5%, 1%, or even responses that were not reproduced in the simulations. Notice that this

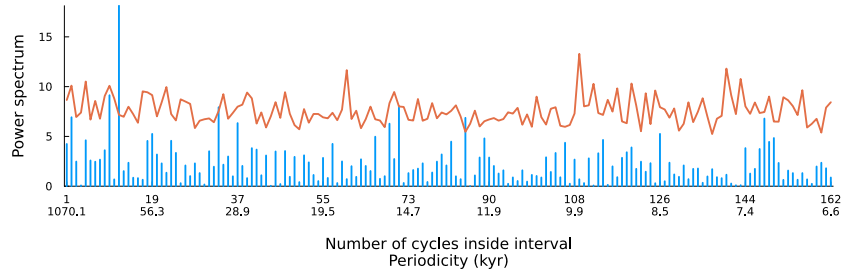


Figure 1.2: Blue vertical bars represent the frequency content of the eruption record. Red line is the maximum value of attained over 10.000 simulated Poisson processes.

procedure can be carried out with models other than the Poisson process.

In Schindlbeck et al. (2018), a strong 100 kyr periodicity coinciding with the Milankovitch eccentricity was detected in the record of explosive eruptions of the Izu-Bonin arc. The result of applying the method described in this section to this data can be seen in Figure 1.2.

Apart from supporting the finding in the aforementioned work, these results illustrate two main advantages of our approach: (1) no manipulation of the eruption record is necessary, assuring the results are not an artifact of the processing of the data, and (2) the better performance of the procedure allows us to assess the significance of the periodicity by comparing it with the responses of thousands of simulations.

1.4 Evidence for coupling between glacial cycles and explosive eruptions in the Izu-bonin arc

In Schindlbeck et al. (2018), the evidence linking climate to explosive eruptions was indirect, relying on common periodicities between the $\delta^{18}\text{O}$ LR04 global stack record (Lisiecki and Raymo, 2005) and the eruption record derived from IODP hole 350-U1437B, comprising 166 explosive eruptions from Japan and the Izu-Bonin-Mariana arc over the last 1.1 Myr (Figure 1.3). The goodness-of-fit test described in Section 1.2 provides a more direct and formal way to test this relationship.

The main hypothesis is that periods of rapid warming at the end of glacial cycles lead to increased number of explosive eruptions, caused by crustal stress changes due to the offloading of terrestrial ice and increase of the sea level. Being a proxy for temperature/sea level, the $\delta^{18}\text{O}$ record does not directly quantify climate changes, however, a simple transformation can be performed to extract this information.

Assume we have a function $f(t)$ and an interval length l . The l -central difference

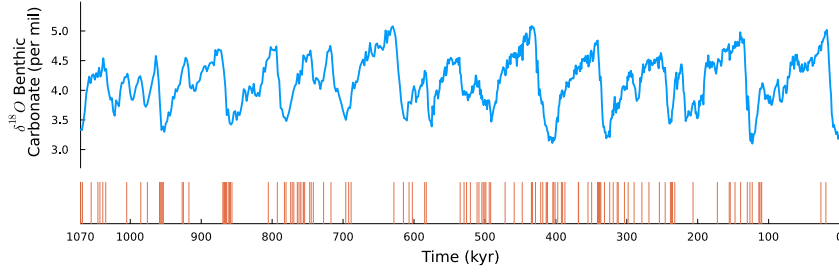


Figure 1.3: The $\delta^{18}O$ LR04 global stack record for the last 1.07 Myr (blue line) along with the calculated onset times of eruptions from the Izu-Bonin arc (red vertical lines).

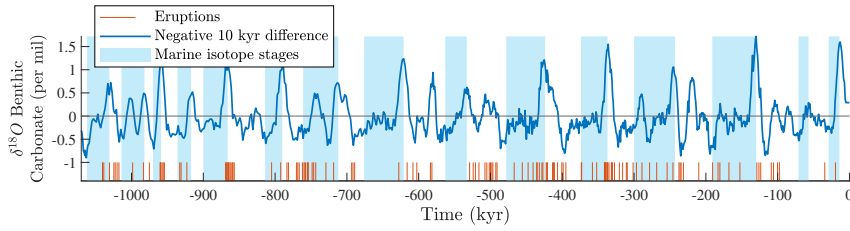


Figure 1.4: Comparison of the negative 10 kyr central difference of the $\delta^{18}O$ record as defined in Equation 1.2 (blue line) with glacial (blue areas) and interglacial (white areas) periods as defined by the Marine Isotope Stages. The red lines on the bottom mark the onset times of eruptions.

of f is denoted $\Delta_{f,l}(t)$ and defined as

$$\Delta_{f,l}(t) = f\left(t + \frac{l}{2}\right) - f\left(t - \frac{l}{2}\right). \quad (1.2)$$

If the derivative of a function captures instantaneous variations, the central difference can be thought of a derivative for variations over longer intervals specified by the parameter l . For our purposes, $f(t)$ is replaced with the $\delta^{18}O$ record, but the parameter l must still be chosen. To avoid spurious correlations, the parameter l was chosen by visual inspection of the $\delta^{18}O$ record and set to 10.000 kyr, without any knowledge on how it would affect the performance of the goodness-of-fit test. To validate that $l = 10$ is an appropriate choice, Figure 1.4 compares $\Delta_{\delta,10}$ with the Marine Isotope Stages (MIS) (Lisiecki and Raymo, 2005), which delimit the different glacial/interglacial cycles.

Notice that not all layers in the tephra record are provenient from the Izu-Bonin arc, as it also contains 21 layers from Japan and Korea. Because the geological settings are very different and could respond very differently to the fast warming periods observed in the 10 kyr difference of the $\delta^{18}O$ record, the layers with provenance from Japan and Korea were disregarded, resulting in a record comprising 145

events.

The goodness-of-fit test from Section 1.2 was performed for all the models described in Section 1.1 with the function f in the Inhomogeneous Poisson and Hawkes process replaced with the 10 kyr-central difference of the $\delta^{18}O$ record. The p-values returned for the hypotheses of Poisson, inhomogeneous Poisson, Hawkes, and inhomogeneous Hawkes processes were of 0, 0, 0.053, and 0.083, respectively. Although the resulting p-values are still low, the hypotheses of Hawkes and inhomogeneous Hawkes processes cannot be rejected at a 95% level.

Most notable, however, are the results of the tests applied to the subsets of felsic, high silica, and mafic, low silica, eruptions. The p-values for the felsic events are 6.6% and 19% for the Poisson and inhomogeneous Poisson processes, respectively, suggesting a very good fit for the former. For mafic eruption, in contrast, these p-values were both 0%, showing a clearly different behavior which, coupled with the large p-values of 22.6% and 28.6% for the Hawkes versions, suggests that clustering plays a much more important role for these types of events.

1.5 Development of software packages for the analysis of point process data

Two software packages were developed during this project. The first (Kling et al., 2023) is implemented in MATLAB (The MathWorks Inc., 2022) and contains all the necessary procedures for performing our novel goodness-of-fit test, including simulations of point processes, estimation of parameters for conditional intensity functions, calculation of log likelihoods, etc.

The second implementation (Kling et al., 2024) is an improvement of the former, including not only all the procedures from the first package, but also the methods for frequency analysis of eruption records. A further advantage of this implementation is that it is coded in the Julia programming language (Bezanson et al., 2017), which, in contrast to MATLAB, is open source.

For Poisson, inhomogeneous Poisson, and Hawkes processes, the necessary calculations and algorithms, including likelihood computations (Ozaki, 1979) and parameter estimation (Veen and Schoenberg, 2008) and simulation (Møller and Rasmussen, 2005) methods, are well-documented in the literature. In contrast, the procedures for inhomogeneous Hawkes processes were developed specifically by adapting methods originally designed for standard Hawkes processes.

References

- G. Jogesh Babu and C. R. Rao. Goodness-of-fit tests when parameters are estimated. *Sankhyā: The Indian Journal of Statistics (2003-2007)*, 66(1):63–74, 2004. ISSN 0972-7671. URL <http://www.jstor.org/stable/25053332>.
- Thystere M Bantidi and Georges Mavonga. Stochastic modeling of the eruption history of nyiragongo volcano in the virunga volcanic province, western branch of the east african rift system. *Statistics in Volcanology*, 5:1–25, feb 2023. doi: 10.5038/2163-338x.5.1.
- M. S. Bartlett. The spectral analysis of point processes. *Journal of the Royal Statistical Society Series B: Statistical Methodology*, 25(2):264–281, July 1963. ISSN 1467-9868. doi: 10.1111/j.2517-6161.1963.tb00508.x.
- M. S. Bebbington. Trends and clustering in the onsets of volcanic eruptions. *Journal of Geophysical Research*, 115(B1), jan 2010. doi: 10.1029/2009jb006581.
- Mark Bebbington. Models for temporal volcanic hazard. *Statistics in Volcanology*, 1:1–24, jan 2013. doi: 10.5038/2163-338x.1.1.
- Andrea Bevilacqua, Franco Flandoli, Augusto Neri, Roberto Isaia, and Stefano Vitale. Temporal models for the episodic volcanism of campi flegrei caldera (italy) with uncertainty quantification. *Journal of Geophysical Research: Solid Earth*, 121(11):7821–7845, nov 2016. doi: 10.1002/2016jb013171.
- Jeff Bezanson, Alan Edelman, Stefan Karpinski, and Viral B Shah. Julia: A fresh approach to numerical computing. *SIAM Review*, 59(1):65–98, 2017. doi: 10.1137/141000671. URL <https://epubs.siam.org/doi/10.1137/141000671>.
- Alberto Boretti. Reassessing the cooling that followed the 1991 volcanic eruption of mt. pinatubo. *Journal of Atmospheric and Solar-Terrestrial Physics*, 256:106187, 2024. ISSN 1364-6826. doi: <https://doi.org/10.1016/j.jastp.2024.106187>.
- Giuseppe Cavaliere, Ye Lu, Anders Rahbek, and Jacob Stærk-Østergaard. Bootstrap inference for hawkes and general point processes. *Journal of Econometrics*, 235(1):133–165, July 2023. ISSN 0304-4076. doi: 10.1016/j.jeconom.2022.02.006.
- Feng Chen and Peter Hall. Inference for a nonstationary self-exciting point process with an application in ultra-high frequency financial data modeling. *Journal of Applied Probability*, 50(4):1006–1024, dec 2013. doi: 10.1239/jap/1389370096.

- Servando De la Cruz-Reyna. Poisson-distributed patterns of explosive eruptive activity. *Bulletin of Volcanology*, 54(1):57–67, dec 1991. doi: 10.1007/bf00278206.
- N. I. Deligne, S. G. Coles, and R. S. J. Sparks. Recurrence rates of large explosive volcanic eruptions. *Journal of Geophysical Research*, 115(B6), jun 2010. doi: 10.1029/2009jb006554.
- Allen F. Glazner, Curtis R. Manley, J. S. Marron, and Stuart Rojstaczer. Fire or ice: anticorrelation of volcanism and glaciation in california over the past 800,000 years. *Geophysical Research Letters*, 26(12):1759–1762, June 1999. ISSN 1944-8007. doi: 10.1029/1999gl900333.
- Chih-Hsiang Ho, Eugene I Smith, Daniel L Feuerbach, and Terry R Naumann. Eruptive probability calculation for the yucca mountain site, USA: statistical estimation of recurrence rates. *Bulletin of Volcanology*, 54(1):50–56, dec 1991. doi: 10.1007/bf00278205.
- Peter Huybers and Charles Langmuir. Feedback between deglaciation, volcanism, and atmospheric CO₂. *Earth and Planetary Science Letters*, 286(3-4):479–491, sep 2009. doi: 10.1016/j.epsl.2009.07.014.
- Anastasia Ignatieva, , Andrew Bell, and Bruce Worton. Point process models for quasi-periodic volcanic earthquakes. *Statistics in Volcanology*, 4:1–27, apr 2018. doi: 10.5038/2163-338x.4.2.
- A. Mark Jellinek, Michael Manga, and Martin O. Saar. Did melting glaciers cause volcanic eruptions in eastern california? probing the mechanics of dike formation. *Journal of Geophysical Research: Solid Earth*, 109(B9):n/a–n/a, sep 2004. doi: 10.1029/2004jb002978.
- José Kling, Mathias Vetter, Julie Schindlbeck-Belo, Marion Jegen, and Steffen Kutterolf. Pointprocesstools (software), 2023.
- José Kling, Mathias Vetter, Julie Schindlbeck-Belo, Marion Jegen, and Steffen Kutterolf. Pointprocesstools.jl (software), 2024.
- Steffen. Kutterolf, Marion Jegen, Jerry X. Mitrovica, Tom Kwasnitschka, Armin Freundt, and Peter J. Huybers. A detection of milankovitch frequencies in global volcanic activity. *Geology*, 41(2):227–230, feb 2013. doi: 10.1130/g33419.1.
- Lorraine E. Lisiecki and Maureen E. Raymo. A pliocene-pleistocene stack of 57 globally distributed benthic $\delta^{18}o$ records. *Paleoceanography*, 20(1):n/a–n/a, jan 2005. doi: 10.1029/2004pa001071.

- Warner Marzocchi and Mark S. Bebbington. Probabilistic eruption forecasting at short and long time scales. *Bulletin of Volcanology*, 74(8):1777–1805, jul 2012. doi: 10.1007/s00445-012-0633-x.
- Benoît Molineaux and Pierre Ineichen. Impact of pinatubo aerosols on the seasonal trends of global, direct and diffuse irradiance in two northern mid-latitude sites. *Solar Energy*, 58(1):91–101, 1996. ISSN 0038-092X. doi: [https://doi.org/10.1016/0038-092X\(96\)00051-5](https://doi.org/10.1016/0038-092X(96)00051-5).
- Jesper Møller and Jakob G. Rasmussen. Perfect simulation of hawkes processes. *Advances in Applied Probability*, 37(3):629–646, sep 2005. doi: 10.1239/aap/1127483739.
- David A. G. Nowell, M. Chris Jones, and David M. Pyle. Episodic quaternary volcanism in france and germany. *Journal of Quaternary Science*, 21(6):645–675, June 2006. ISSN 1099-1417. doi: 10.1002/jqs.1005.
- Yosihiko Ogata. Statistical models for earthquake occurrences and residual analysis for point processes. *Journal of the American Statistical Association*, 83(401):9–27, mar 1988. doi: 10.1080/01621459.1988.10478560.
- T. Ozaki. Maximum likelihood estimation of hawkes’ self-exciting point processes. *Annals of the Institute of Statistical Mathematics*, 31(1):145–155, dec 1979. doi: 10.1007/bf02480272.
- D. E. Parker, H. Wilson, P. D. Jones, J. R. Christy, and C. K. Folland. The impact of mount pinatubo on world-wide temperatures. *International Journal of Climatology*, 16(5):487–497, 1996. doi: [https://doi.org/10.1002/\(SICI\)1097-0088\(199605\)16:5%3C487::AID-JOC39%3E3.0.CO;2-J](https://doi.org/10.1002/(SICI)1097-0088(199605)16:5%3C487::AID-JOC39%3E3.0.CO;2-J).
- M. Paterne, J. Labeyrie, F. Guichard, A. Mazaud, and F. Maitre. Fluctuations of the campanian explosive volcanic activity (south italy) during the past 190,000 years, as determined by marine tephrochronology. *Earth and Planetary Science Letters*, 98(2):166–174, may 1990. doi: 10.1016/0012-821x(90)90057-5.
- Summer Praetorius, Alan Mix, Britta Jensen, Duane Froese, Glenn Milne, Matthew Wolhowe, Jason Addison, and Fredrick Prahl. Interaction between climate, volcanism, and isostatic rebound in southeast alaska during the last deglaciation. *Earth and Planetary Science Letters*, 452:79–89, oct 2016. doi: 10.1016/j.epsl.2016.07.033.

Michael R. Rampino, Stephen Self, and Rhodes W. Fairbridge. Can rapid climatic change cause volcanic eruptions? *Science*, 206(4420):826–829, nov 1979. doi: 10.1126/science.206.4420.826.

Harriet Rawson, David M. Pyle, Tamsin A. Mather, Victoria C. Smith, Karen Fontijn, Stefan M. Lachowycz, and José A. Naranjo. The magmatic and eruptive response of arc volcanoes to deglaciation: Insights from southern chile. *Geology*, 44(4): 251–254, feb 2016. doi: 10.1130/g37504.1.

Alan Robock. Volcanic eruptions and climate. *Reviews of Geophysics*, 38(2): 191–219, may 2000. doi: 10.1029/1998rg000054.

Laura Sandri, Alexander Garcia, Antonio Costa, Alejandra Guerrero Lopez, and Gustavo Cordoba. Stochastic modeling of explosive eruptive events at galeras volcano, colombia. *Frontiers in Earth Science*, 8, jan 2021. doi: 10.3389/feart.2020.583703.

Julie C. Schindlbeck, Marion Jegen, Armin Freundt, Steffen Kutterolf, Susanne M. Straub, Maryline J. Mleneck-Vautravers, and Jerry F. McManus. 100 kyr cyclicity in volcanic ash emplacement: evidence from a 1.1 myr tephra record from the NW pacific. *Scientific Reports*, 8(1), mar 2018. doi: 10.1038/s41598-018-22595-0.

Jacopo Selva, Laura Sandri, Matteo Taroni, Roberto Sulpizio, Pablo Tierz, and Antonio Costa. A simple two-state model interprets temporal modulations in eruptive activity and enhances multivolcano hazard quantification. *Science Advances*, 8 (44), nov 2022. doi: 10.1126/sciadv.abq4415.

Gudmundur E Sigvaldason, Kristian Annertz, and Magnus Nilsson. Effect of glacier loading/deloading on volcanism: postglacial volcanic production rate of the dyngjufjöll area, central iceland. *Bulletin of Volcanology*, 54(5):385–392, jul 1992. doi: 10.1007/bf00312320.

Y. Tamura, C.J. Busby, P. Blum, G. Guèrin, G.D.M. Andrews, A.K. Barker, J.L.R. Berger, E.M. Bongiolo, M. Bordiga, S.M. DeBari, J.B. Gill, C. Hamelin, J. Jia, E.H. John, A.-S. Jonas, M. Jutzeler, M.A.C. Kars, Z.A. Kita, K. Konrad, S.H. Mahony, M. Martini, T. Miyazaki, R.J. Musgrave, D.B. Nascimento, A.R.L. Nichols, J.M. Ribeiro, T. Sato, J.C. Schindlbeck, A.K. Schmitt, S.M. Straub, M.J. Vautravers, Y., and Yang. Site u1437. In *Proceedings of the International Ocean Discovery Program*. International Ocean Discovery Program, may 2015. doi: 10.14379/iodp.proc.350.104.2015.

The MathWorks Inc. Matlab version: 9.13.0 (r2022b), 2022. URL <https://www.mathworks.com>.

Alejandro Veen and Frederic P Schoenberg. Estimation of space-time branching process models in seismology using an EM-type algorithm. *J Amer Statist Assoc*, 103(482):614–624, jun 2008. doi: 10.1198/016214508000000148.

Sebastian F.L. Watt, David M. Pyle, and Tamsin A. Mather. The volcanic response to deglaciation: Evidence from glaciated arcs and a reassessment of global eruption records. *Earth-Science Reviews*, 122:77–102, jul 2013. doi: 10.1016/j.earscirev.2013.03.007.

Chapter 2

A goodness-of-fit test for the analysis of the temporal distribution of explosive eruptions

Kling, J.C.F., Schindlbeck-Belo, J.C., Vetter, M., Jegen, M., Kutterolf, S.

Submitted to Volcanica.

Climatic responses to large explosive volcanic eruptions, such as surface cooling caused by the injection of volcanic aerosols and ash, have been observed several times in history (Robock, 2000). That climate changes may in turn also have an impact on volcanic activity is a relatively recent and fascinating discovery. The recognition came originally from studies of glaciated regions (e.g., Iceland, Alaska), which demonstrated a significantly increased eruption rate after the last glaciation, probably facilitated by unloading of the lithosphere during glacier retreat (Rampino et al., 1979; Sigvaldason et al., 1992; Praetorius et al., 2016; Rawson et al., 2016, e.g.). Later, global compilations of subaerial volcanism indicated an increased number of eruptions during the last deglaciation (Huybers and Langmuir, 2009).

Furthermore, it has been recognized that eruption records long enough to cover many glacial cycles exhibit the same periodicities as the global climate record (Paterne et al., 1990; Kutterolf et al., 2013, e.g.). Global climate changes occur with the periodicities of the so-called Milankovitch cycles, which reflect orbital forcing of global climate (Lisiecki, 2010), including the cycles of precession (23 kyr) and obliquity (41 kyr) of Earth's rotation axis, and the eccentricity (100 kyr) of Earth's rotation around the sun. These periods are visible in the temporal variations of climate proxies, the most prominent being the globally stacked marine foraminiferal $\delta^{18}O$ record, in which $\delta^{18}O$ is mainly a measure of sea level, and therefore reflects glacial-interglacial variations (Lisiecki and Raymo, 2005, e.g.).

Although the underlying physical processes (e.g., change in crustal stress, enhanced magma production) are still largely unknown, a connection of cyclic Earth orbital parameters to volcanism has been established first by Paterne et al. (1990), who observed a 23 kyr periodicity in the Campanian marine tephra (fragmented volcanic particles; ash) record that appeared related to the Earth's precession and associated Earth tides. Kutterolf et al. (2013) detected a strong 41 kyr periodicity in a "Ring of Fire" tephra record compiled from sediment drill sites around the Pacific, and associated it with the periodic obliquity changes of the Earth's rotation axis, while Schindlbeck et al. (2018a) detected a dominant 100 kyr periodicity in an 1.1 Myr tephra time series recovered at the Izu-Bonin arc in the Northwest Pacific. Kutterolf et al. (2019) provided a review on the Milankovitch frequencies in tephra records and re-analyzed four well-characterized tephra records by applying the same methodology, and showed that all four records contain the 41 kyr and 100 kyr periodicities, which significantly correlate with the $\delta^{18}O$ record proxy for global ice volume/sea level change. These and numerous other studies have presented evidence linking volcanic activity and climate change. However, a major challenge has been the limited availability of specific statistical procedures for testing the

various hypotheses connecting the occurrence of eruptions to external factors.

In this work the eruption onset times will be modeled as a point process, which assumes that eruptions occur randomly over some interval of time. Although this approach has been widely used in the literature (De la Cruz-Reyna, 1991; Deligne et al., 2010; Bebbington, 2010; Bevilacqua et al., 2016; Selva et al., 2022, e.g.), it has not been extensively applied to this specific context, in which an external factor may influence the occurrence of events. Furthermore, a reliable goodness-of-fit test - that is, a test to check whether a given parametric point process model adequately fits the observations - for point processes has, to this date, been lacking in the literature.

The numerous studies on linking volcanic eruption data and point processes have mostly dealt with the estimation of parameters, and questions regarding goodness of fit have been typically answered in two ways: The first method involves the Akaike information criterion (AIC) to compare how well different models fit the data relative to one another (Tuel et al., 2017; Bantidi and Mavonga, 2023, e.g.). This approach has a limitation — it cannot assess whether any of the hypotheses explain the data satisfactorily at all. The second is a Kolmogorov-Smirnov type statistic which compares the distribution of the data with one under an estimated model (Ogata, 1988; Bebbington, 2013; Marzocchi and Bebbington, 2012, e.g.). In contrast to the first, this procedure returns a p-value - the probability of the observed data occurring assuming the hypothesis is correct - for each individual hypothesis. Because of the lack of a sound method in the literature, this procedure does not account for the estimation of unknown parameters, which affects the correct computation of p-values (see the example in Babu and Rao (2004) or Section 2.3.3 later). In this work, a new solution to this problem is given by providing an asymptotically valid goodness-of-fit test for the ex-post analysis of the temporal distribution of events, utilizing recently developed bootstrap techniques for point processes (Cavaliere et al., 2023). An extensive simulation study showing that the method works for virtually all classical self-exciting point process models is presented. We have refrained from giving a formal proof of the consistency of the test in this paper, but see Kling and Vetter (2024) for the specific case of inhomogeneous Poisson processes.

The test will be then utilized to re-analyze the tephra record from the IODP Hole 350-U1437B (Schindlbeck et al., 2018b,a) in conjunction with the LR04 $\delta^{18}O$ global reference stack (Lisiecki and Raymo, 2005) as a proxy for ice volume/sea level. The objective of this analysis will be to determine if a link between climate and eruption rate can be observed. All the algorithms, including parameter estimation of processes, simulation of event history and the test itself, were implemented in MATLAB ver.2021b and are available in Kling et al. (2024).

This paper contains five sections in addition to this introduction. Section 2.1 presents the data that motivated this work, the 1.1 Myr eruption record from the Izu-Bonin arc and the $\delta^{18}O$ climate proxy. Section 2.2 contains a brief synthesis of relevant concepts related to point processes and introduces four models corresponding to different hypotheses on how eruption rate and climate are related. Section 2.3 provides an explanation on how the novel goodness-of-fit test works, compares it with the previously used methods for hypothesis testing, and assesses its reliability using simulated data. In Section 2.4, the results of the test applied to the eruption record are described, (1) by applying the goodness-of-fit test to the complete data and (2) by applying the test to two different subsets of the data. Finally, in Section 2.5, further discussion on these results, their interpretation, and the advantages and limitations of the procedure is presented, followed by concluding remarks.

2.1 Data

In the following the data used in this study will be described. The main aim is to obtain insights on the distribution of eruptions and its relation to climate in the form of the sea level/ice volume proxy by applying the novel goodness-of-fit test, but it will also serve as a prime example on the setup of the statistical framework and the proposed methodology. The main aim is to apply the test to tephra data, in order to obtain insights on the distribution of eruptions and its relation to climate in the form of the global ice volume proxy.

2.1.1 Tephra Data

The observation data used throughout this paper is the 1.1 Myr marine tephra record (166 explosive eruptions) from the Izu-Bonin-Mariana arc, in the northwestern Pacific. It derives from the upper 140 meters of sediments recovered in IODP Hole 350-U1437B (Tamura et al., 2015) and was previously studied by Schindlbeck et al. (2018b), Schindlbeck et al. (2018a), and Kutterolf et al. (2019). The sediment record has a remarkably good recovery rate ($\geq 99\%$). Furthermore, the multiproxy age model, which is based on a stable oxygen isotope stratigraphy and supported by independent ages of tephra time markers reveals a constant average sedimentation rate of 12 cm/kyr with no evidence of hiatuses (Schindlbeck et al., 2018a,b). The investigated tephra layers have been interpreted as fallout deposits of large explosive subaerial or shallow marine eruptions with magnitudes $M_v > 4$ (Schindlbeck et al., 2018b).

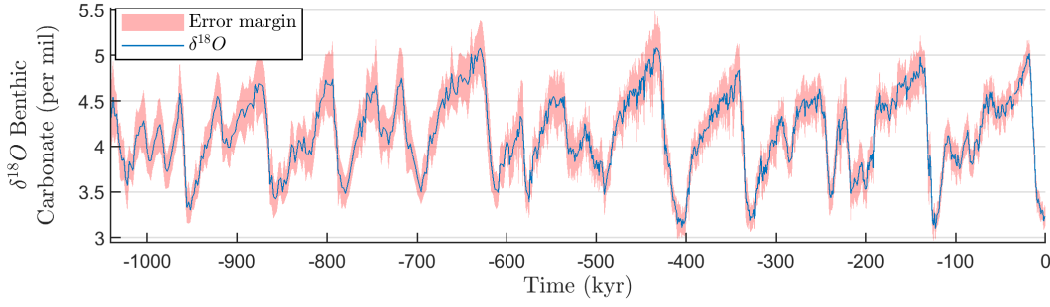


Figure 2.1: LR04 $\delta^{18}O$ global reference stack for the past 1.07 Myr (blue line) with the associated error estimates (red shaded region).

The 166 events are subdivided into three groups according to their provenance, (1) the Izu-Bonin volcanic front (119 events), (2) the Izu-Bonin active rift (26 events), and (3) the Japanese volcanic arcs (21 events) as classified by Schindlbeck et al. (2018a). Out of the 166 events, the 21 tephra layers coming from Japan volcanic arcs are neglected, focusing solely on tephras stemming from the Izu-Bonin region. This is done to avoid any interference of the two different geological settings (continental Japanese arc versus oceanic Izu-Bonin Arc), which might result in misinterpretation of the results. The remaining 145 events can be further subdivided into three groups based on their geochemical composition. (1) 110 felsic (high silica $\geq 65 wt\%$), (2) 27 mafic (low silica), and (3) eight bimodal eruptions (one eruption with two geochemical compositions). The record also contains four pairs of events with the same calculated ages at 339.6 kyr, 339.7 kyr, 418.4 kyr, and 493.9 kyr.

For all details on composition, provenance, and volume calculations of the individual tephra layers we refer to Schindlbeck et al. (2018b). By applying spectral analysis, Schindlbeck et al. (2018a) observed a statistically significant spectral peak at ~ 100 kyr period within the data set, which they correlated with the $\delta^{18}O$ record as climate/sea level proxy. For more discussion we refer to Schindlbeck et al. (2018a).

2.1.2 Climate Proxy Data

The climate proxy used in this work is the LR04 $\delta^{18}O$ global reference stack (Lisiecki and Raymo, 2005), which is a proxy for global ice volume. It comprises 2115 measurements over the last 5.5 Myr along with corresponding measurement errors. The most recent 600 kyr of data is sampled at a 1000 years period, while the remaining data is sampled at a 2000 years period. In all calculations a linear interpolation is performed to determine the values in points between samples (Figure 2.1).

One possible explanation relating climate and volcanism is the change in crustal stress, providing more frequent pathways for magma to rise to the surface, caused by the change in sea level (Albino et al., 2010; Watt et al., 2013). Although periods of paleo stress are difficult to be identified directly, this can be done indirectly via changes in the $\delta^{18}O$ levels, and has been previously applied to earth system models resulting in stress changes over time (Kutterolf et al., 2013).

Since $\delta^{18}O$ levels are inversely correlated to sea level, periods of sea level rise are characterized by a decrease in the $\delta^{18}O$ record, which are identified with intervals when the record's derivative is negative. Because the observations are discrete, the derivative would need to be approximated, which can, up to scaling, be done by means of finite central differences. Given some time span h , define the h central finite differences of the function f as

$$\Delta_{h,f}(t) = f(t + h/2) - f(t - h/2). \quad (2.1)$$

To approximate the derivative of f up to a constant, one can simply set h to be twice the interval between samples, therefore calculating the difference between the next and the previous sample available. This setting has, however, the disadvantage of being extremely sensitive to small perturbations, hindering the identification of longer trends. By changing the value of h , it is possible to focus on changes on some specific time scale. In the posterior analysis, the negative of the 10 kyr central finite differences of the $\delta^{18}O$ record will be used, as it makes periods of intense deglaciation correspond to large positive values. The adequacy of these choices can be assessed in Fig. 2.2, where the negative values of the 10 kyr difference are plotted against the marine isotope stages (MIS) (Lisiecki and Raymo, 2005). It is clear that large positive values are related to transitions from glacial (blue regions) to interglacial (white regions) periods.

The value of $h = 10$ kyr was chosen by visual inspection of the $\delta^{18}O$ record, based on the duration of the strongest changes in the data and additional results not reported in this paper prove that the results we provide are very similar if we choose e.g. $h = 8$ kyr or $h = 12$ kyr instead. Another alternative would have been to test many different values of h and to select the one which fits the eruption record best, however, such a procedure was avoided as it would increase the chance of finding spurious correlations.

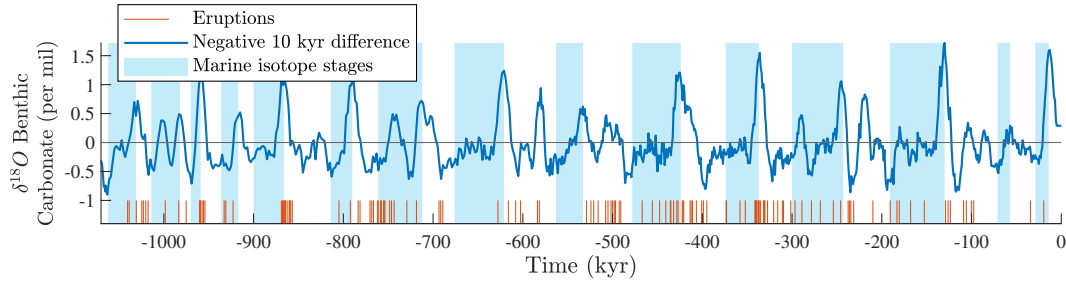


Figure 2.2: Comparison of the negative 10 kyr central difference of the $\delta^{18}\text{O}$ record as defined in Equation 2.1 (blue line) with glacial (blue areas) and interglacial (white areas) periods as defined by the Marine Isotope Stages. The red lines on the bottom mark the onset times of each eruption. Notice that, even though the 10 kyr central difference is not defined for the interval $[0, 5000]$, the values for the period were extrapolated as a constant to maintain the same interval of analysis.

2.2 Models for time dependent eruption rate

In order to perform any kind of statistical procedure, it is key to define a proper model for the data. The general framework proposed here is to model the eruption records as point processes on the real line, as already done in numerous studies (De la Cruz-Reyna, 1991; Furlan, 2010; Bebbington, 2013; Bantidi and Mavonga, 2023, e.g.). Of particular importance are the processes that admit a conditional intensity function (CIF), as such a function offers a natural way for an attempt to quantify the eruption rate (for a concise overview of point processes, see Laub et al. (2021)). There are two equivalent ways to formally model these processes.

(a) Via a counting process $(N(t)|t > 0)$, which satisfies three properties: (i) $N(0) = 0$, (ii) N is a right continuous increasing step function with increments of 1, and (iii) N is (almost surely) finite. In this setting, $N(t)$ is the number of events that occur during the interval $[0, t]$, therefore, for any $s_1 < s_2$, $N(s_2) - N(s_1)$ is the number of events observed in the interval $(s_1, s_2]$. Condition (i) means that the process starts at $t = 0$, (ii) ensures that two events cannot occur at the same time, and (iii) guarantees that only a finite number of events can occur in any given finite period of time.

(b) Via a sequence of random variables $\tau = (t_1, t_2, \dots)$ such that the probabilities of the variables being non-negative and non-decreasing is equal to 1 and, for any bounded time interval, the number of points in that interval is (almost surely) finite. Here, t_i stands for the time of the i -th volcanic eruption in the data series.

In the models above, it is assumed that there are no simultaneous events. Since in our analyses the Izu-Bonin arc is considered as a system, whenever simultaneous events are present in the data set, they will be treated as single events. Slightly

different procedures are possible, but were found to not have a significant impact in the conclusions of the analyses.

The most important concept related with point processes is that of the conditional intensity function. Although events occur randomly, the likelihood of them occurring might change over time, meaning that the expected number of events per unit of time might vary (eruptions/year, in this case). This variability is captured by the CIF, which, at each point, quantifies the ‘instantaneous likelihood’ that an event happens. The CIF thus provides a way to determine if the distribution of events over time matches what is expected if some external function, like the proxy for deglaciation in this case, was modulating the intensity of the process.

Formally, for some counting process N , define $\mathcal{H}(t)$ as the history of the process in $[0, t]$. The CIF of the process is a (possibly random) function λ from $[0, T]$ to $[0, \infty)$ and is given by the identity

$$\lambda(t) = \lim_{h \rightarrow 0} \frac{E[N(t+h) - N(t) | \mathcal{H}(t)]}{h}. \quad (2.2)$$

The CIF quantifies, at each point, how many events are expected to occur per unit of time, therefore the larger the CIF, the more events will tend to occur in this period. More generally, the expected number of events in any interval $(s_1, s_2]$ can be calculated as

$$E[N(s_2) - N(s_1) | \mathcal{H}(s_1)] = E\left[\int_{s_1}^{s_2} \lambda(t) dt | \mathcal{H}(s_1)\right]. \quad (2.3)$$

Notice that for the Poisson and inhomogeneous Poisson processes (Section 2.2.1), $\lambda(t)$ does not depend on past events and is a deterministic function, therefore, in these cases, the dependency on \mathcal{H} can be dropped.

However, if $\lambda(t)$ depends on \mathcal{H} then it is not a function, but a random process. To better understand this, consider $\lambda(s)$ for some $s > 0$. If the process up to time s has already been observed, in which case $\mathcal{H}(s)$ is fully specified, then $\lambda(s)$ is just a specific number. If the process has not yet been observed, then $\mathcal{H}(s)$ resembles the different ways the future might play out, and this translates to the randomness of $\lambda(s)$.

2.2.1 Model parametrization

The proposed procedure is to test different hypotheses for how the rate of occurrence of the detected eruptions changes over time, starting with a simple model and gradually adding complexity. Four different possibilities are considered here and

will be presented in this section: (a) A (homogeneous) Poisson process, (b) an inhomogeneous Poisson process, (c) a Hawkes process, and (d) a Hawkes process with time-varying base intensity.

For the definitions presented below, the first letters in the subscripts are H or I and stand for 'Homogeneous' or 'Inhomogeneous', following the terminology of Poisson processes, while the second letters are P and H for 'Poisson' and 'Hawkes', respectively. HP then refers to homogeneous Poisson, IP to inhomogeneous Poisson, HH to (homogeneous) Hawkes, and IH to inhomogeneous Hawkes.

Poisson

The initial hypothesis to be tested is whether eruption rate is constant over time, which characterizes the Poisson process (De la Cruz-Reyna, 1991; Selva et al., 2022). In this scenario the occurrence of eruptions is not affected by climate nor by previous events. This hypothesis corresponds to the CIF of the process that generated the observations being constant, which means that the CIF for this model contains only one positive parameter μ which defines the function

$$\lambda_{HP}(t; \mu) = \mu. \quad (2.4)$$

Figure 2.3 includes examples of the four different models introduced in this section. Figure 2.3a shows a simulated Poisson process over 500 kyr and its corresponding CIF with $\mu = 1.5 \times 10^{-4}$. For the simulation of this and the following models, the parameters were chosen arbitrarily so as to produce clearly visible differences between distinct models. Still, the average number of events produced in the simulations is comparable to what is observed in the Izu-Bonin data set.

Inhomogeneous Poisson

The next step is to check whether activity follows some specific external factor, which, in this case, is assumed to be the 10 kyr central finite differences of the $\delta^{18}O$ record (see Eq. (2.1)). Confirming this hypothesis would suggest a coupling between climate, or, more specifically, deglaciation periods, and increased volcanic activity. Inhomogeneous Poisson processes have been used in previous works (Ho et al., 1991), although not in the context of testing the influence of some specific external factor on the occurrence of eruptions.

Let $f : [0, T] \rightarrow \mathbb{R}$ be the function corresponding to the external factor of interest. Instead of using f directly, it will always be normalized so that $\min(f) = 0$

and $\max(f) = 1$. Although not strictly necessary, this transformation facilitates the interpretation and comparison between different models and, more importantly, simplifies the algorithms needed for parameter estimation later. Therefore, in the following, f will denote its normalized version, specifically, $\frac{f(t) - \min(f)}{\max(f) - \min(f)}$.

The CIF of the inhomogeneous Poisson process contains an additional positive parameter γ and is defined as

$$\lambda_{IP}(t; \mu, \gamma) = \mu + \gamma f. \quad (2.5)$$

Essentially, the parameter μ represents the baseline rate at which events occur, regardless of the value of the external factor f , while γ quantifies how strong the dependency of the process on f is. A simulation with $\mu = 5 \times 10^{-5}$ and $\gamma = 1.5 \times 10^{-4}$ over 500 kyr is shown in Fig. 2.3b.

Because of the linearity of the integral, it is possible to determine what influence each of the terms has in the process. If $N_{IP}(\cdot; \mu, \gamma)$ is the counting process associated to the process with CIF $\lambda_{IP}(\cdot; \mu, \gamma)$, then from Eq. (2.3) and Eq. (2.5)

$$\begin{aligned} E[N_{IP}(s_2; \mu, \gamma) - N_{IP}(s_1; \mu, \gamma)] \\ &= \int_{s_1}^{s_2} \lambda_{IP}(t; \mu, \gamma) dt = \int_{s_1}^{s_2} (\mu + \gamma f(t)) dt \\ &= (s_2 - s_1)\mu + \gamma \int_{s_1}^{s_2} f(t) dt. \end{aligned} \quad (2.6)$$

Therefore, this model will generate, on average, $\int_0^T (\mu + \gamma f(t)) dt$ events on the interval $[0, T]$, with μT of them expected to be caused by the baseline rate (therefore independently of f) and $\gamma \int_0^T f(t) dt$ by the external factor f . These values provide an indication of the strength of the process' dependency on the function f .

Hawkes

A preliminary visual analysis of the data shows that the eruptions tend to cluster together and that this behavior might not be accounted for with the previous models (see the later discussion in Fig. 2.8), suggesting that models containing a self-exciting component could provide a better fit. Hawkes processes have been widely used in seismology to detect earthquake clustering (Ogata, 1988).

Here the hypothesis is that volcanism has no relation with climate, but eruptions do exhibit an internal dependency, where the occurrence of an event increases the

probability of observing another one shortly after the first, meaning that eruptions tend to occur in clusters.

This tendency can be incorporated in the Poisson process by adding the (random) self-exciting term $\sum_{t_i < t} \alpha e^{-\beta(t-t_i)}$ to Eq. (2.4), where α and β are parameters and t_i refers to events in the observation (t_1, \dots, t_N) . Hence,

$$\lambda_{HH}(t; \mu, \alpha, \beta) = \mu + \sum_{t_i < t} \alpha e^{-\beta(t-t_i)}. \quad (2.7)$$

This new term causes each event to trigger an increase in the CIF (and, therefore, an increase in the probability of an event occurring) with amplitude α , which decays exponentially with rate β . The effect can be clearly seen in Fig. 2.3c, displaying a simulation of a Hawkes process with parameters $\mu = 5 \times 10^{-5}$, $\alpha = 2 \times 10^{-5}$ and $\beta = 6 \times 10^{-5}$.

Hawkes with time-varying base intensity

While the previous model was built simply by adding the self-exciting component to the homogeneous Poisson model, this last one is built analogously, but starting from the inhomogeneous version of the Poisson process (Chen and Hall, 2013), i.e.,

$$\lambda_{IH}(t; \mu, \gamma, \alpha, \beta) = \mu + \gamma f + \sum_{t_i < t} \alpha e^{-\beta(t-t_i)}. \quad (2.8)$$

In this last case, the hypothesis is that both dependencies mentioned above play a role, the dependence on the external factor and the internal dependence. This last model is depicted in Fig. 2.3d by a simulation over 500 kyr with parameters $\mu = 5 \times 10^{-5}$, $\gamma = 7 \times 10^{-5}$, $\alpha = 3 \times 10^{-5}$ and $\beta = 8 \times 10^{-5}$.

Earthquakes provide a useful analogy for understanding the last two processes. The occurrence of main shocks is modeled by the terms corresponding to Poisson processes, which may be constant (μ) or dependent on other processes, such as tides or orbital changes ($\mu + \gamma f(t)$). After a main shock, there is a probability that aftershocks are triggered ($\alpha e^{-\beta(t-t_i)}$), which in turn might trigger even more events, until this part of the process eventually dies out.

The framework described in this section provides some advantages:

1. The eruption rate is directly quantified by the CIF, which makes the models easily interpretable.
2. It is applicable to data in any time scale and for different external factors. For example, it would be possible to apply the same analysis presented in this paper

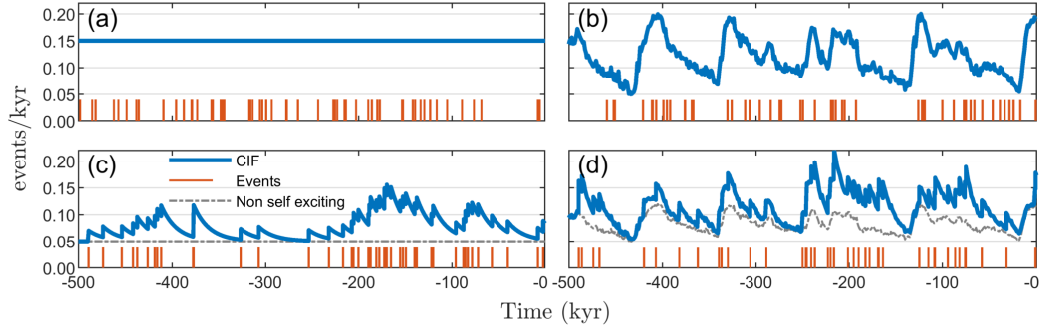


Figure 2.3: Simulations of events over 500 kyr following (a) a Poisson, (b) an inhomogeneous Poisson, (c) a Hawkes and (d) an inhomogeneous Hawkes process. Dashed gray lines are the CIF of the processes excluding the self-exciting component, which consist of μ for panel (c) and $\mu + \gamma f(t)$ for panel (d).

to the influence of tides on seismic activity.

3. By using the $\delta^{18}O$ record as a hypothesized external factor, the effect of the uncertainty in the determination of the eruption ages is minimized. The ages for the eruptions are, among other techniques, derived from the correlation of measured $\delta^{18}O$ values in foraminifer shells present in the sediments, which are further tuned with the LR04 $\delta^{18}O$ global reference stack. Therefore, even if the dating uncertainty is still present, the correlation between events and $\delta^{18}O$ levels remains mostly intact.

2.3 Goodness-of-fit test

For independent and identically distributed data, the problem of testing models with parameters that must be estimated is well-known and dates back to e.g., Darling (1955), Kac et al. (1955) and Lilliefors (1967). The main strategy is to estimate the unknown parameters and then take a suitable distance between the empirical distribution of the data and the one which is theoretically expected if the model was true and the estimated parameters were the correct ones. The problem with these approaches, however, is that the theoretical distributions of this distance are rarely known and change with the distribution of the underlying model, or that they depend on the unknown parameters in a complicated way (Durbin, 1973), so that one needs to rely on simulation methods in order to obtain the quantiles for a valid goodness-of-fit test. Two convincing solutions have more recently been provided by Babu and Rao (2004) and Meintanis and Swanepoel (2007), who have proven under very general assumptions that a bootstrap-based method leads to asymptotically

consistent tests.

In the case of point processes, however, the picture is less clear. Showing consistency and asymptotic normality of maximum-likelihood estimators for point processes dates back to Ogata (1978) and Vere-Jones (1982), albeit in very restrictive situations. It was only recently that Chen and Hall (2013) proved asymptotic normality within a large class of parametric models involving self-exciting point processes. Chen and Hall (2013) also mention that a formal goodness-of-fit test for these models is missing, essentially for the same reasons as historically for i.i.d. observations. In this section such a test will be presented, which utilizes recently developed bootstrap techniques for point processes (Cavaliere et al., 2023).

2.3.1 Testing conditional intensity function with known parameters

In order to better explain the method and to illustrate how it differs from what has been done in previous works, consider the case in which the hypothesis to be tested is whether a specific hypothesized CIF λ_0 is a good fit for observed events. In this setting λ_0 might come directly from a specific function or from fixing parameters in one of the models in Sect. 2.2.

One standard goodness-of-fit test in this case is known as the Kolmogorov-Smirnov test. If λ_0 is the true intensity process and (t_1, t_2, \dots) denote the event times, then the random variables

$$X_i = \int_{t_{i-1}}^{t_i} \lambda_0(t) dt \quad (t_0 = 0) \quad (2.9)$$

are independent and known to follow a unit exponential distribution (Laub et al., 2021). Conversely, if the distribution of the X_i 's deviates significantly from the exponential, then λ_0 is probably not the true CIF. This deviation can be measured with the Kolmogorov-Smirnov distance (KS-distance), which, for observed events (t_1, \dots, t_N) and CIF λ , is calculated as in Equation (2.10), where the term $(1 - e^{-x})$ is the cumulative distribution function of the unit exponential distribution, and $\mathbb{1}_{[0,x]}$ is the characteristic function of the interval $[0, x]$, therefore $\frac{1}{N} \sum_{i=1}^N \mathbb{1}_{[0,x]}(X_i)$ is the empirical cumulative distribution function of the X_i 's.

$$\begin{aligned} KS((t_1, \dots, t_N, \lambda)) \\ = \sup_{x \in [0, \infty)} \left| (1 - e^{-x}) - \left(\frac{1}{N} \sum_{i=1}^N \mathbb{1}_{[0,x]}(X_i) \right) \right|. \end{aligned} \quad (2.10)$$

Equation (2.10) therefore measures the discrepancy between the observed process and some idealized theoretical behavior. To determine the p-value of the test, the KS-distance calculated from the data must be compared with the distribution of the distances from processes known to follow the hypothesized model. In some cases this distribution can be calculated explicitly, in this work, however, we approximate it via simulations. A p-value of 0.05 is the standard confidence threshold for a goodness-of-fit test, therefore, hypotheses whose test returns a p-value smaller than 0.05 are rejected.

Notice that in this approach there is no estimation needed, as the hypothesis fully specifies the conditional intensity function λ_0 . In most applications, however, there is no fixed λ_0 as a hypothesis. It is instead assumed that the true CIF depends on a set of parameters θ (as an example, in the Inhomogeneous Poisson case, $\theta = (\mu, \gamma)$) and that there exists some θ_0 such that the true intensity of the process is $\lambda_0(\cdot) = \lambda(\cdot; \theta_0)$.

One straightforward way to adapt this method to the case where θ_0 is not known is simply to replace λ_0 by $\lambda(\cdot; \hat{\theta})$, where $\hat{\theta}$ are the parameters estimated from the data. Although intuitive, one must be cautious when interpreting the results for such a test, since the estimation of θ_0 does not guarantee that the X_i 's are i.i.d. and exponentially distributed under the null hypothesis.

A simple simulation test can be performed to determine the performance of this procedure. Consider the case in which the hypothesis to be tested is if the data follows a Poisson process, that is, if there exists some μ_0 such that $\lambda_0(t) = \mu_0$. A proper goodness-of-fit test, when applied to a set of data coming from the true hypothesis, should produce a p-value which is uniformly distributed over the interval $[0, 1]$, therefore, if the procedure is valid, then the distribution of a large number of p-values resulting from this test on data independently simulated from Poisson processes (with the same fixed parameter) should be approximately uniform (Sackrowitz and Samuel-Cahn, 1999). Figure 2.4a shows 10000 p-values from these simulations.

It is clear from Fig. 2.4a that lower p-values are significantly less frequent than they should be for a valid goodness-of-fit test, consequently, hypotheses are less likely to be rejected. It should be pointed out that the Poisson process is the simplest of the point processes and contains a single parameter to be estimated, and for more complex models this effect could be amplified. For Fig. 2.4b the novel procedure explained below was carried out, which clearly generates approximately uniformly distributed p-values.

The KS plot, a visual tool widely utilized to evaluate the goodness of fit of point process models (Ogata, 1988; Bebbington, 2010; Ignatieva et al., 2018; Bantidi and Mavonga, 2023, e.g.), uses the values stemming from such a procedure to construct

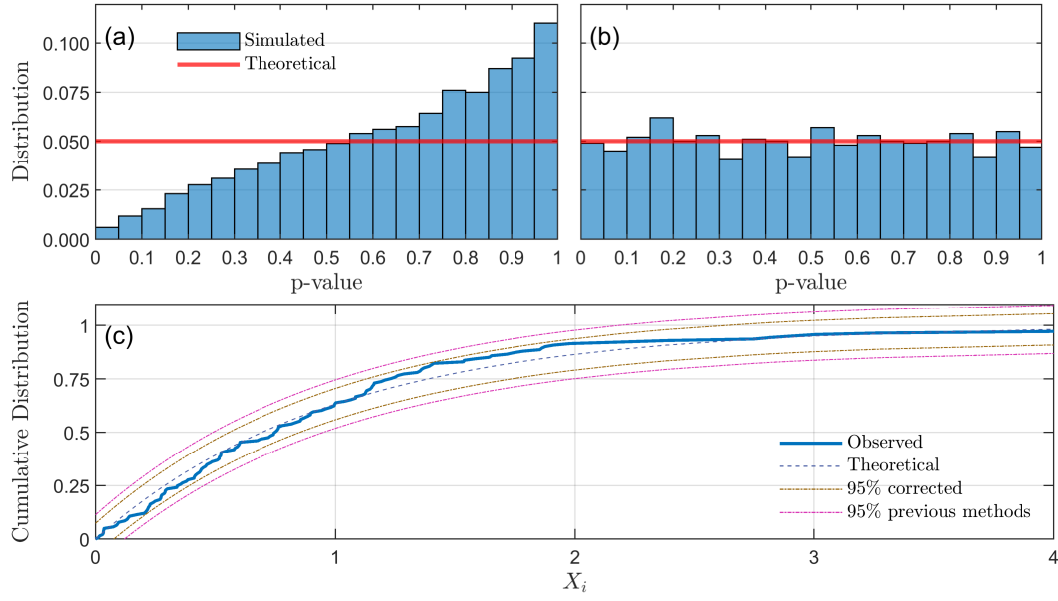


Figure 2.4: Theoretical and observed distribution of p-values for previously used methods (a) and the new goodness-of-fit test (b), showing the correctness of the new procedure. (c) KS-plot comparing the 95% confidence intervals of each procedure.

the confidence intervals. Figure 2.4c compares the 95% bands produced by the algorithm described here with those calculated using the novel bootstrap procedure outlined in the following section. Although in reality the observation is barely inside the true confidence interval, the previous method lacks the power to reject incorrect hypotheses and would have shown a very good fit.

It is important to notice that, although very similar, the procedure described here may not be exactly the same as the ones used in other works (Ogata, 1988; Chen and Hall, 2013; Bebbington, 2013, 2010; Marzocchi and Bebbington, 2012, e.g.).

The procedure described above is just one way how goodness-of-fit tests based on the KS-distance have been introduced in the literature. In practice, these approaches (Ogata, 1988; Chen and Hall, 2013; Bebbington, 2013, 2010; Marzocchi and Bebbington, 2012, e.g.) might differ slightly from the way we have presented them, depending e.g. on the actual model and the way parameters are estimated. However, the overall principle of their tests is essentially the same, and, more importantly, we have also conducted more specific simulation tests tailored to the procedures presented in these papers, and they confirm the behavior spotted in Figure 2.4(a). More details can be found in the supplementary materials.

2.3.2 Testing conditional intensity function with unknown parameters

As shown in the previous section, the adaptation of the Kolmogorov-Smirnov test above produces inconsistent hypothesis tests. The main problem is that, by estimating the parameters, one can fit the model to the data much better than a fixed hypothesis would, in a way "overfitting" the model, and this effect must be taken into account. In fact, it is well known that neglecting this discrepancy may incur unwanted bias and lead to incorrect results (Babu and Rao, 2004). A modification is, therefore, needed. The bootstrap-based algorithm is as follows.

Algorithm 2.3.1.

1. *Based on observations (t_1, \dots, t_N) and a candidate model λ , estimate θ_0 as $\hat{\theta}$ and compute $\hat{d} = KS((t_1, \dots, t_N), \lambda(\cdot; \hat{\theta}))$.*
 2. *Simulate B point processes $((t_1^b, \dots, t_{N_b}^b), b = 1, \dots, B)$ with the intensity function $\lambda(\cdot; \hat{\theta})$.*
 3. *For each simulation, estimate $\hat{\theta}$ as θ_b^* ($b = 1, 2, \dots, B$).*
 4. *For each $b = 1, \dots, B$, calculate $d_b = KS((t_1^b, \dots, t_{N_b}^b), \lambda(\cdot; \theta_b^*))$.*
 5. *If there are exactly k distances such that $d_b \geq \hat{d}$, then the desired p -value is $\frac{k}{B}$.*
-

The term bootstrap in Algorithm 2.3.1 refers to steps 1 and 2, in which information from data is used for resampling. In items 3 and 4, instead of calculating the KS-distance with respect to the intensity estimated from the original observation as done in the previous section, the distance is calculated with respect to the intensity estimated from a simulated process. This is done to resemble the procedure in item 1. The distribution constructed in item 4 serves as an approximation of the distribution of the KS-distance under the null hypothesis that the data-generating model is indeed the proposed one.

In this work the algorithm will be applied only to the four models presented in Sect. 2.2, but simulation tests show that it also produces consistent goodness-of-fit tests for a wider range of models, for example, the Weibull renewal process from Bebbington (2013) and the two-state model from Selva et al. (2022).

Some technical remarks are in order. The parameters in steps 1 and 3 of Algorithm 2.3.1 are estimated by maximizing the likelihood function of the process (Ozaki, 1979), so, as the maximum likelihood estimator (MLE). Chen and Hall (2013) proved that such estimation is consistent and asymptotically normal, which,

roughly speaking, guarantees that the estimates become more accurate with larger sample sizes, making MLE a reliable and efficient method for parameter estimation. However, the computation is specific for each of the models. For the Poisson process the MLE is calculated as the average number of events per unit of time (N/T). For all other models no closed formula exists, therefore for the inhomogeneous Poisson case the MLE is approximated by optimizing the likelihood function using MATLAB's trust region reflective algorithm, and, finally, for both self-exciting processes, Expectation-Maximization (EM) algorithms are applied (Veen and Schoenberg, 2008).

Notice also that the normalization of the proxy (Section 2.1.2) does not interfere with the results. If f is the original non-normalized proxy and f^* its normalization, then $\mu + \gamma f(t) = (\mu + \gamma \min(f)) + (\gamma(\max(f) - \min(f)))f^*(t)$, therefore, the MLE with respect to f can be easily transformed into the MLE with respect to f^* and vice-versa, and these solutions are mathematically equivalent.

2.3.3 Simulation Tests

To determine the reliability of the procedure described in the last section, it is necessary to assess the accuracy of the approximation of the distribution of KS distances in different settings. This can be done with a test, which is conducted by simulating a set of events from a known conditional intensity function (estimated from the data), then applying Algorithm 2.3.1 to each of the simulations and recording the p-values. For each of the four models, the procedure described in Algorithm 2.3.1 is repeated for 1000 simulations of event records produced using the parameters estimated from the data, and $B = 1000$. The results are then plotted as a histogram of p-values. If the test works, the distribution of p-values should be approximately uniform over the interval $[0, 1]$, showing that the test approximately keeps the level α for every pre-specified $\alpha \in [0, 1]$.

Visual inspection of the histograms in Fig. 2.5 already shows that the distributions of the p-values are close to uniform. It is possible, however, to use a classical Kolmogorov-Smirnov based test for uniformity for a more formal assessment. The test applied to each of the four models described in Sect. 2.2.1 yielded p-values of 0.99, 0.60, 0.36 and 0.22, respectively, showing a good fit in all cases. Therefore, not only the statistical procedure is reliable for a variety of point process models, but also the sample size of the Izu-Bonin eruption record is adequate for the test to work properly.

In the next section, however, the events will be split into felsic and mafic/bimodal.

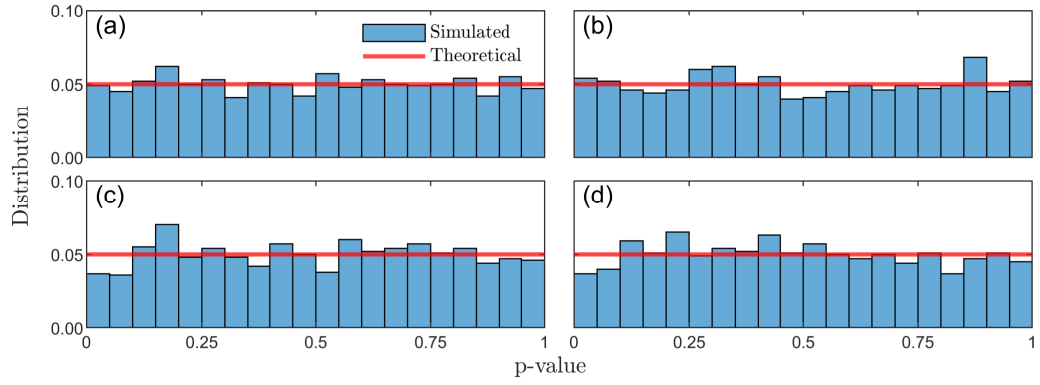


Figure 2.5: Distribution of 1000 p-values generated by Alg. 2.3.1 against the true model for **(a)** Poisson, **(b)** inhomogeneous Poisson, **(c)** Hawkes, and **(d)** inhomogeneous Hawkes processes. P-values for uniformity are 0.99, 0.60, 0.36, and 0.22, respectively.

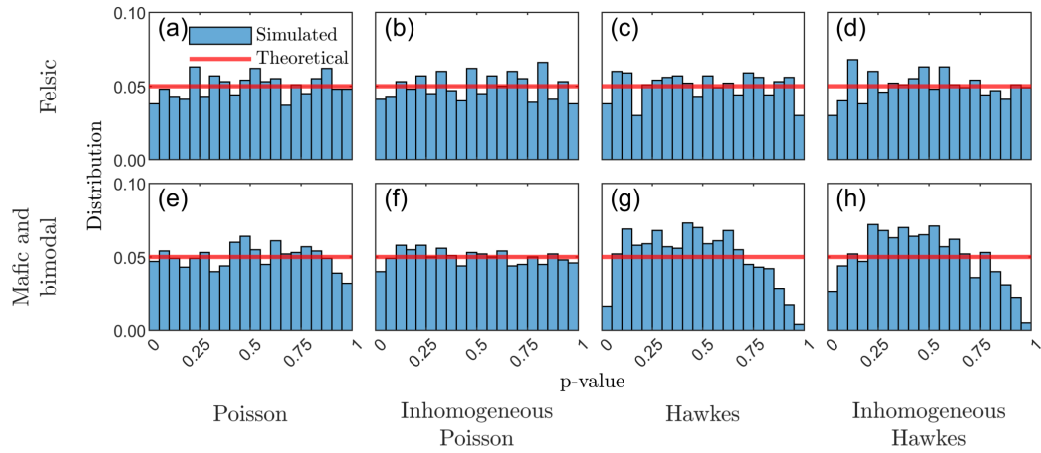


Figure 2.6: Same as in Fig. 2.5 for each of the four models and two subsets. Uniformity tests yields p-values of **(a)** 0.29, **(b)** 0.81, **(c)** 0.50, **(d)** 0.29, **(e)** 0.15, **(f)** 0.60, **(g)** 0.00, **(h)** 0.00.

Since the robustness of this test depends on the number of events and on the specific parameters, the same procedure was carried out for both subsets and the results are presented in Fig. 2.6. The p-values for uniformity are 0.29, 0.81, 0.50, and 0.29 for the felsic subset and 0.15, 0.60, 0.00, and 0.00 for the mafic subset. Note that for the homogeneous and inhomogeneous Hawkes processes restricted to sets with very few events (such as mafic eruptions) the test is clearly unreliable.

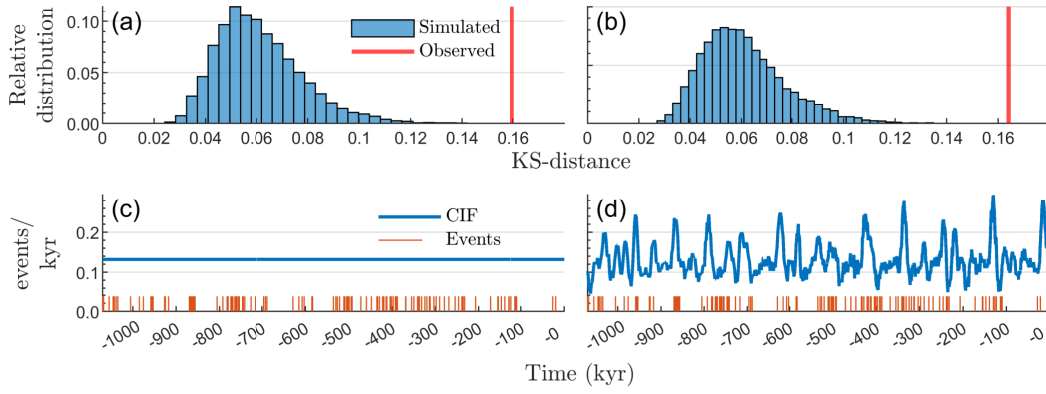


Figure 2.7: **(a) (b)** Approximated distribution and calculated KS-distance with respect to the complete data set for the Poisson ($p = 0$) and inhomogeneous Poisson ($p = 0$) process. **(c) (d)** Eruptions record and estimated CIF as a Poisson and inhomogeneous Poisson process.

2.4 Results

Some evidence has been building up for the case that glacial cycles influence volcanic activity (Sigvaldason et al., 1992; Praetorius et al., 2016; Schindlbeck et al., 2018a; Kutterolf et al., 2019, e.g.), with different methods been applied to try to validate the results. This section presents an application of the goodness-of-fit test introduced in Sect. 2.3 to the analysis of the eruption record from the Izu-Bonin volcanic arc (Sect. 2.1). The detailed analysis and interpretation of the results will be presented in Sect. 2.5.

2.4.1 Complete eruption record

The first and simplest model is the Poisson process. The result of applying Algorithm 2.3.1 with $\lambda_0(t; \mu) = \mu$ can be seen in Fig. 2.7. The estimated value for the parameter μ is 1.32×10^{-4} , and none of the simulations exhibited a distance larger than that of the observation, therefore yielding a p-value of 0.

The next model to be considered is the Inhomogeneous Poisson process with the function f in Eq. (2.5) replaced by the normalized 10 kyr difference of the $\delta^{18}O$ record (Eq. (2.1)). The estimated parameters are $\mu = 4.64 \times 10^{-5}$ and $\gamma = 2.48 \times 10^{-4}$, but the result, however, does not improve when compared to the Homogeneous Poisson Process, still returning a p-value of 0.

Despite showing that the proposed intensities are not a good fit for the data, the result does not provide any insight into why this is the case. This question can be addressed by the K-S plot presented in Sect. 2.3.1. Figure 2.8 displays the observed

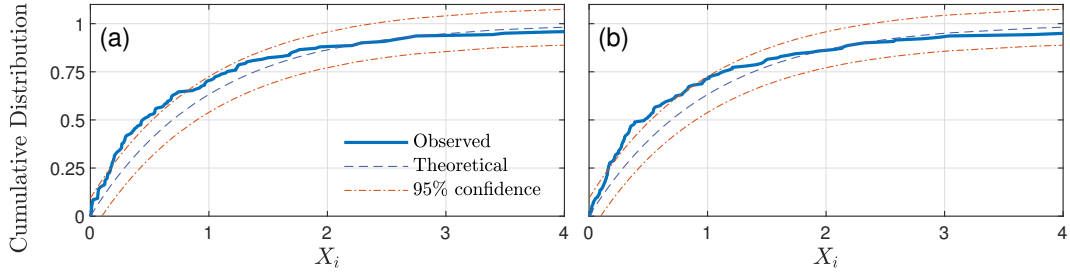


Figure 2.8: KS plot for **(a)** the Poisson and **(b)** the inhomogeneous Poisson processes. Horizontal axis is the value of the random variable X_i and the vertical axis the normalized cumulative number of occurrences.

cumulative distribution of the random variables X_i presented in Eq. (2.9) computed with respect to the estimated parameters (blue) and a standard exponential, along with a 95% confidence interval for both the Homogeneous and Inhomogeneous Poisson models. The excess of observations at the beginning of the graph means that there are many more short intervals than expected.

These observations, together with the visual clustering of events, suggest that it makes sense to test for Hawkes Processes, discussed in Sect. 2.2.1. Although it is not necessarily assumed that eruptions trigger subsequent events, the clustering observed in the previous analysis (Fig. 2.8) suggests the existence of an additional unknown underlying process that causes this effect, which can be approximated by a self-exciting behavior.

The test from Fig. 2.7 was carried out once again, but this time for both versions of the Hawkes process. The results are shown in Fig. 2.9. For the homogeneous version, the test returns the parameters $\mu = 7.14 \times 10^{-5}$, $\alpha = 1.17 \times 10^{-4}$ and $\beta = 2.55 \times 10^{-4}$, and a p-value of 0.053. For the inhomogeneous case the parameters are $\mu = 1.82 \times 10^{-5}$, $\gamma = 1.5 \times 10^{-4}$, $\alpha = 9.94 \times 10^{-5}$ and $\beta = 2.11 \times 10^{-4}$, with a p-value of 0.083.

2.4.2 Mafic and felsic eruptions

One feature of the Izu-Bonin tephra data set investigated in this study is that it consists of both felsic and mafic tephra layers as well as a small number of bimodal events. Felsic magmas are generally characterized by a higher silica content and evolve over longer time scales and in shallower crustal magma reservoirs than mafic magmas, which are generally stored at deeper levels and are heavily influenced by the degree of melting (Schmincke, 2004). The higher grade of differentiation of felsic magmas generally results in higher silica contents and more dissolved volatiles in the magma, making them more viscous and more prone to explosive eruptions.

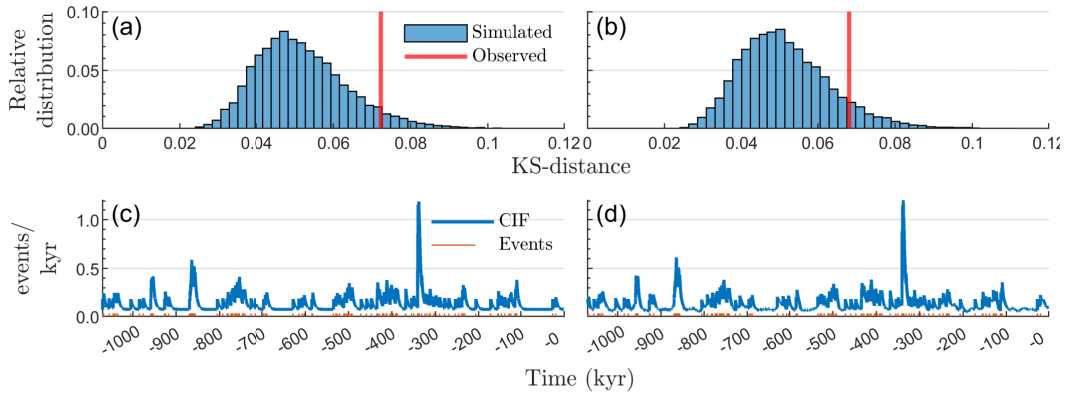


Figure 2.9: Same as in Fig. 2.7 for the Hawkes processes. Test returned $p = 0.053$ for Hawkes and $p = 0.083$ for inhomogeneous Hawkes.

Nevertheless, there is also a subset of mafic explosive eruptions observed in the Izu-Bonin data set. The physical mechanisms that are discussed on how climate induced sea level changes affect volcanism are (1) the stress changes in the crust, which might open pathways for rising magma, or (2) direct influence on the degree of melting in the mantle (e.g., Huybers and Langmuir (2009); Rawson et al. (2016); Kutterolf et al. (2019) and references therein). Analyzing the subsets separately may give additional insights on these factors and their influence on the distribution of eruptions relative to the overall climate.

In order to determine if there is a difference in the eruption frequency behavior related to the composition of the magmas, the test will be applied to the two subsets, the subset of felsic events, and the subset of mafic and bimodal events.

The result of applying the test to the felsic eruptions can be seen in Fig. 2.10 below. For the homogeneous Poisson process the estimated parameter is $\mu = 1.01 \times 10^{-4}$ and returned a p-value of 0.066, while in the inhomogeneous case the parameters are $\mu = 3.99 \times 10^{-5}$ and $\gamma = 1.77 \times 10^{-4}$ with a p-value of 0.19.

The same procedure, when applied to mafic and bimodal eruptions, yields p-values of 0 for both versions of the Poisson process, 0.226 for the homogeneous Hawkes process, and 0.286 for its inhomogeneous version. The estimated parameters are $\mu = 3.66 \times 10^{-5}$ for the Poisson process, $\mu = 8.74 \times 10^{-6}$ and $\gamma = 8.07 \times 10^{-5}$ for inhomogeneous Poisson, $\mu = 1.55 \times 10^{-5}$, $\alpha = 1.72 \times 10^{-4}$ and $\beta = 2.98 \times 10^{-4}$ for Hawkes, and, finally, for the inhomogeneous Hawkes process, $\mu = 6.05 \times 10^{-6}$, $\gamma = 2.63 \times 10^{-5}$, $\alpha = 1.57 \times 10^{-4}$ and $\beta = 2.68 \times 10^{-4}$.

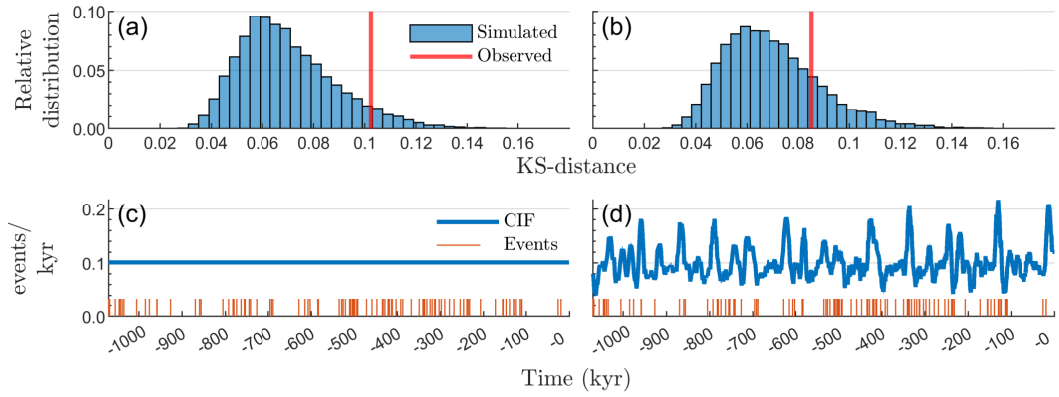


Figure 2.10: Same as in Fig. 2.7 considering only felsic eruptions and Poisson processes. Test returned $p = 0.066$ for Poisson and $p = 0.19$ for inhomogeneous Poisson.

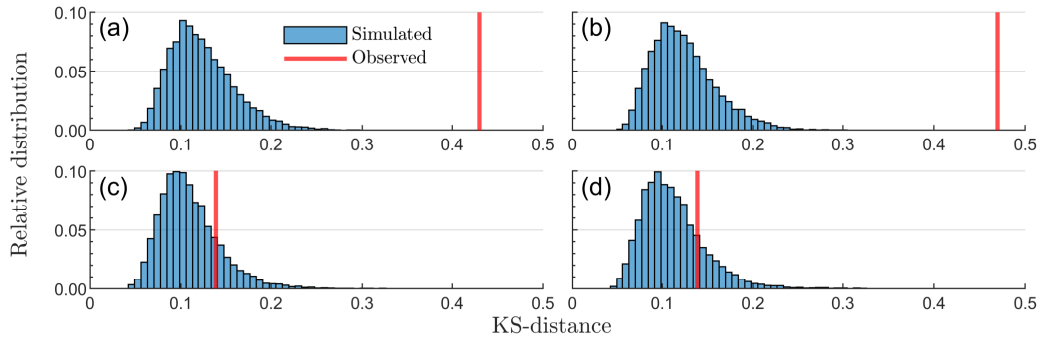


Figure 2.11: Test results considering only mafic and bimodal eruptions. (a) $p = 0$ for the Poisson, (b) $p = 0$ for the Inhomogeneous Poisson, (c) $p = 0.24$ for the Hawkes process, and (d) $p = 0.29$ for the Inhomogeneous Hawkes processes.

2.5 Discussion and closing remarks

2.5.1 Analysis of the results

The first important result presented in this work is the rejection of the hypothesis that the eruption rate remained constant during the time. This conclusion is derived from the goodness-of-fit test, which yields a p-value of 0 when applied to the hypothesis of a Poisson process. While Schindlbeck et al. (2018a) previously indicated a correlation between the Izu-Bonin eruption record and the climate proxy - and, in particular, that the eruption rate is not constant - no formal test was performed to rule out this possibility. However, the fact the test's p-value was also 0 for the inhomogeneous Poisson process suggests that other factors, possibly additionally to climate, are modulating the the occurrence of eruptions.

As observed in previous works, eruptions can exhibit a tendency to cluster in

time (Bebbington, 2010; Selva et al., 2022; Bantidi and Mavonga, 2023, e.g.). In particular, Bevilacqua et al. (2016) and Bebbington and Cronin (2011) resorted to the Hawkes process to analyze this behavior. By including Hawkes' self-exciting component into the previous models, the p-values returned by the test were slightly above 0.05. This means that the Hawkes and inhomogeneous Hawkes can be reasonable candidates for the true intensity of the process.

As explained in Sect. 2.2, it is possible to determine how many events are expected to be generated by each of the components in a model, providing means to compare how prominent these components are. For the Hawkes process, the constant baseline intensity is expected to be accountable for 54% of the events, with the remaining 46% being attributed to the self-exciting component. What is noteworthy, however, is that in the inhomogeneous version, the constant component is expected to generate only 13.8% of the events, most of it being shifted to the component related to the climate proxy with 39.2% of the events, and leaving essentially the same 47% to the self-exciting component. This large portion of events attributed to the external factor suggests that it might have a significant impact on the process.

To further investigate this problem, the record was split into mafic/bimodal and felsic eruptions and the same analysis applied to each subset.

For the felsic events, the test shows that even a simple Poisson process cannot be rejected at a 5% confidence level, yielding a p-value of 0.066. The inhomogeneous Poisson process, however, significantly improves this value to 0.19 and also estimates that the climate proxy is responsible for 60.5% of the events, while only 39.5% are expected to occur in a constant fashion. This, allied with the findings from Schindlbeck et al. (2018a), provides an even stronger argument for the link between deglaciation and increased volcanic activity. Since the results for these first two models already showed a very good fit, the self-exciting models were omitted.

The mafic and bimodal eruptions exhibit a completely different behavior. Both versions of the Poisson process are rejected with a p-value of 0, demonstrating a clear difference from the felsic events. Although the Hawkes processes produced very large p-values, the reliability of the test cannot be guaranteed due to the small number of events, as shown in Sect. 2.3.3.

These results show that the two different magma compositions exhibit very distinct eruptive behaviors, suggesting an influence of the composition of magmas on the mechanisms causing the explosive eruptions in the Izu-Bonin arc. While felsic eruption exhibit a good coupling with the climate proxy without the need to account for any clustering effects, this is not the case for the mafic/bimodal subset.

Although the test for Hawkes processes has not been shown to be completely reliable for such a small number of events, the result of the goodness-of-fit test, together with the clustering observed in the complete data set, points towards these models being very reasonable for the evolution of mafic/bimodal events. For conclusive results, deeper statistical analysis and investigations to pin down possible mechanisms that can account for this difference are needed. Yet, the goodness-of-fit test presented in this work is capable of capturing different types of processes, even with relatively small events.

2.5.2 Advantages and limitations of the methodology

The goodness-of-fit test proposed in this study has the potential to serve as a unifying framework in the analysis of eruption rates, either by improving or by extending previous methods. The Julie code including the implementation of this test along with simulation and estimation algorithms is openly available for future research (Kling et al., 2024). The following paragraphs will highlight some of the advantages of this test.

Similarly to this work, Tuel et al. (2017) and Ammann and Naveau (2003) propose parametric models for the volcanic process intensity. There, however, each year comprised by the eruption record is treated as a discrete Bernoulli random variable, which provides a straightforward and intuitive representation of the data. Nonetheless, the estimation of the intensity of the process must be done indirectly through the logarithm of the odds of each random variable, making the results less interpretable compared to the estimation via point processes, which can perform this estimation directly.

The development of a robust goodness-of-fit test for point processes on the real line is a significant improvement over previously available procedures. It solves the problem of not having a reliable way to assess whether a hypothesis was consistent with the data in hand, and provides results based on sound statistical theory.

The procedure may also offer rigorous tests for a larger array of models not explored in this work. The Weibull renewal process (Bebbington, 2013) and the two-state model (Selva et al., 2022) were already mentioned, but the authors are convinced that this is the case for a much broader class of models, although more detailed computational and theoretical analyses are required to determine for which specific ones.

For the specific case considered in this paper, however, there is an added benefit of using the $\delta^{18}O$ record instead of some arbitrary function. Although the uncertainty

in age dating has not been tackled directly, since the $\delta^{18}O$ values are taken into account when performing the dating of the events, the $\delta^{18}O$ levels at the time of each event are not prone to large deviations, which makes the correlation between events and $\delta^{18}O$ values robust.

Lastly, even though the motivation for this work is the analysis of the temporal distribution of explosive eruptions, the proposed method is extremely flexible, since it is applicable to problems in any time scale and does not need large numbers of events to be effective. It also has virtually no restrictions on what external factors could be considered and is possibly applicable to models other than the ones considered here.

The presented procedure does, however, have its limitations. Firstly, it is complex and computationally intensive, especially for both versions of the Hawkes process, because of their recursive nature. While this is not a problem for small data sets such as the ones analyzed here, for applications with thousands of observations the computational cost increases drastically. This limitation most strongly impacts the ability to perform reliability tests, such as those presented in Sect. 2.3.3.

Secondly, additional information from individual events, such as the strength of the eruptions given, for example, by the volcanic explosivity index (VEI) (Newhall and Self, 1982) or geochemical composition, are not considered. While one solution presented here would be to analyze different subsets separately, the classification of events may not be as straightforward as in the case presented here.

2.5.3 Conclusion

In conclusion, this study has successfully developed a robust framework tailored for testing the influence of external factors on volcanic processes. Based on previous works that utilized point processes for modeling the eruption onset times, four different possibilities were considered as candidates to represent the change in eruption rate over time: the Poisson process, the inhomogeneous Poisson process, the Hawkes process, and the inhomogeneous Hawkes process.

A major contribution of this work lies in the introduction of a novel goodness-of-fit test. Unlike existing methods, this test, built upon recent results and techniques, has been demonstrated to be both correct and superior through a comprehensive study using simulated data. Its introduction fills a critical gap in the literature, providing a consistent and reliable means to assess the fit of candidate models to observed records.

The application of our framework to the Izu-Bonin eruption record in conjunction

with the $\delta^{18}O$ record revealed insightful patterns. Notably, the felsic eruptions, which comprise the majority of events in the data set, exhibited a direct correlation with the climate proxy, while the clustering behavior was primarily attributed to a small number of mafic and bimodal events.

In summary, this work presents a new tool for the study of past volcanic processes. Its foundation on solid statistical theory, providing consistent p-values for hypothesis validation, significantly improves the robustness of results when compared to existing methods. Moreover, this approach is extremely flexible. It allows for testing on a broad range of models and has virtually no restrictions on what functions can be used as external factors. It is also not constrained to a particular time scale and can be incorporated in the study of various phenomena, such as earthquakes, neuron firings, trade stock transactions, and spread of diseases. This versatility opens up exciting possibilities for new applications and extensions of the results.

References

- F. Albino, V. Pinel, and F. Sigmundsson. Influence of surface load variations on eruption likelihood: application to two icelandic subglacial volcanoes, grímsvötn and katla. *Geophysical Journal International*, apr 2010. doi: 10.1111/j.1365-246x.2010.04603.x.
- Caspar M. Ammann and Philippe Naveau. Statistical analysis of tropical explosive volcanism occurrences over the last 6 centuries. *Geophysical Research Letters*, 30(5):n/a–n/a, mar 2003. doi: 10.1029/2002gl016388.
- G. Jogesh Babu and C. R. Rao. Goodness-of-fit tests when parameters are estimated. *Sankhyā: The Indian Journal of Statistics (2003-2007)*, 66(1):63–74, 2004. ISSN 0972-7671. URL <http://www.jstor.org/stable/25053332>.
- Thystere M Bantidi and Georges Mavonga. Stochastic modeling of the eruption history of nyiragongo volcano in the virunga volcanic province, western branch of the east african rift system. *Statistics in Volcanology*, 5:1–25, feb 2023. doi: 10.5038/2163-338x.5.1.
- M. S. Bebbington. Trends and clustering in the onsets of volcanic eruptions. *Journal of Geophysical Research*, 115(B1), jan 2010. doi: 10.1029/2009jb006581.
- Mark Bebbington. Models for temporal volcanic hazard. *Statistics in Volcanology*, 1:1–24, jan 2013. doi: 10.5038/2163-338x.1.1.

- Mark S. Bebbington and Shane J. Cronin. Spatio-temporal hazard estimation in the auckland volcanic field, new zealand, with a new event-order model. *Bulletin of Volcanology*, 73(1):55–72, sep 2011. doi: 10.1007/s00445-010-0403-6.
- Andrea Bevilacqua, Franco Flandoli, Augusto Neri, Roberto Isaia, and Stefano Vitale. Temporal models for the episodic volcanism of campi flegrei caldera (italy) with uncertainty quantification. *Journal of Geophysical Research: Solid Earth*, 121(11):7821–7845, nov 2016. doi: 10.1002/2016jb013171.
- Giuseppe Cavaliere, Ye Lu, Anders Rahbek, and Jacob Stærk-Østergaard. Bootstrap inference for hawkes and general point processes. *Journal of Econometrics*, 235(1):133–165, July 2023. ISSN 0304-4076. doi: 10.1016/j.jeconom.2022.02.006.
- Feng Chen and Peter Hall. Inference for a nonstationary self-exciting point process with an application in ultra-high frequency financial data modeling. *Journal of Applied Probability*, 50(4):1006–1024, dec 2013. doi: 10.1239/jap/1389370096.
- D. A. Darling. The cramer-smirnov test in the parametric case. *The Annals of Mathematical Statistics*, 26(1):1–20, mar 1955. doi: 10.1214/aoms/1177728589.
- Servando De la Cruz-Reyna. Poisson-distributed patterns of explosive eruptive activity. *Bulletin of Volcanology*, 54(1):57–67, dec 1991. doi: 10.1007/bf00278206.
- N. I. Deligne, S. G. Coles, and R. S. J. Sparks. Recurrence rates of large explosive volcanic eruptions. *Journal of Geophysical Research*, 115(B6), jun 2010. doi: 10.1029/2009jb006554.
- J. Durbin. Weak convergence of the sample distribution function when parameters are estimated. *The Annals of Statistics*, 1(2), mar 1973. doi: 10.1214/aos/1176342365.
- Claudia Furlan. Extreme value methods for modelling historical series of large volcanic magnitudes. *Statistical Modelling*, 10(2):113–132, jun 2010. doi: 10.1177/1471082x0801000201.
- Chih-Hsiang Ho, Eugene I Smith, Daniel L Feuerbach, and Terry R Naumann. Eruptive probability calculation for the yucca mountain site, USA: statistical estimation of recurrence rates. *Bulletin of Volcanology*, 54(1):50–56, dec 1991. doi: 10.1007/bf00278205.
- Peter Huybers and Charles Langmuir. Feedback between deglaciation, volcanism, and atmospheric CO₂. *Earth and Planetary Science Letters*, 286(3-4):479–491, sep 2009. doi: 10.1016/j.epsl.2009.07.014.

- Anastasia Ignatieva, , Andrew Bell, and Bruce Worton. Point process models for quasi-periodic volcanic earthquakes. *Statistics in Volcanology*, 4:1–27, apr 2018. doi: 10.5038/2163-338x.4.2.
- M. Kac, J. Kiefer, and J. Wolfowitz. On tests of normality and other tests of goodness of fit based on distance methods. *The Annals of Mathematical Statistics*, 26(2): 189–211, jun 1955. doi: 10.1214/aoms/1177728538.
- José Kling, Mathias Vetter, Julie Schindlbeck-Belo, Marion Jegen, and Steffen Kutterolf. Pointprocesstools.jl (software), 2024.
- José C. F. Kling and Mathias Vetter. On goodness-of-fit testing for self-exciting point processes, 2024.
- S. Kutterolf, J.C. Schindlbeck, M. Jegen, A. Freundt, and S.M. Straub. Milankovitch frequencies in tephra records at volcanic arcs: The relation of kyr-scale cyclic variations in volcanism to global climate changes. *Quaternary Science Reviews*, 204:1–16, jan 2019. doi: 10.1016/j.quascirev.2018.11.004.
- Steffen. Kutterolf, Marion Jegen, Jerry X. Mitrovica, Tom Kwasnitschka, Armin Freundt, and Peter J. Huybers. A detection of milankovitch frequencies in global volcanic activity. *Geology*, 41(2):227–230, feb 2013. doi: 10.1130/g33419.1.
- Patrick J. Laub, Young Lee, and Thomas Taimre. *The Elements of Hawkes Processes*. Springer International Publishing, 2021. doi: 10.1007/978-3-030-84639-8.
- Hubert W. Lilliefors. On the kolmogorov-smirnov test for normality with mean and variance unknown. *Journal of the American Statistical Association*, 62(318): 399–402, jun 1967. doi: 10.1080/01621459.1967.10482916.
- Lorraine E. Lisiecki. Links between eccentricity forcing and the 100,000-year glacial cycle. *Nature Geoscience*, 3(5):349–352, apr 2010. doi: 10.1038/geo828.
- Lorraine E. Lisiecki and Maureen E. Raymo. A pliocene-pleistocene stack of 57 globally distributed benthic $\delta^{18}o$ records. *Paleoceanography*, 20(1):n/a–n/a, jan 2005. doi: 10.1029/2004pa001071.
- Warner Marzocchi and Mark S. Bebbington. Probabilistic eruption forecasting at short and long time scales. *Bulletin of Volcanology*, 74(8):1777–1805, jul 2012. doi: 10.1007/s00445-012-0633-x.

- Simos Meintanis and Jan Swanepoel. Bootstrap goodness-of-fit tests with estimated parameters based on empirical transforms. *Statistics & Probability Letters*, 77(10):1004–1013, jun 2007. doi: 10.1016/j.spl.2007.01.014.
- Christopher G. Newhall and Stephen Self. The volcanic explosivity index (VEI) an estimate of explosive magnitude for historical volcanism. *Journal of Geophysical Research: Oceans*, 87(C2):1231–1238, feb 1982. doi: 10.1029/jc087ic02p01231.
- Yoshiko Ogata. The asymptotic behaviour of maximum likelihood estimators for stationary point processes. *Annals of the Institute of Statistical Mathematics*, 30(2):243–261, dec 1978. doi: 10.1007/bf02480216.
- Yoshihiko Ogata. Statistical models for earthquake occurrences and residual analysis for point processes. *Journal of the American Statistical Association*, 83(401):9–27, mar 1988. doi: 10.1080/01621459.1988.10478560.
- T. Ozaki. Maximum likelihood estimation of hawkes’ self-exciting point processes. *Annals of the Institute of Statistical Mathematics*, 31(1):145–155, dec 1979. doi: 10.1007/bf02480272.
- M. Paterne, J. Labeyrie, F. Guichard, A. Mazaud, and F. Maitre. Fluctuations of the campanian explosive volcanic activity (south italy) during the past 190,000 years, as determined by marine tephrochronology. *Earth and Planetary Science Letters*, 98(2):166–174, may 1990. doi: 10.1016/0012-821x(90)90057-5.
- Summer Praetorius, Alan Mix, Britta Jensen, Duane Froese, Glenn Milne, Matthew Wolhowe, Jason Addison, and Fredrick Prah. Interaction between climate, volcanism, and isostatic rebound in southeast alaska during the last deglaciation. *Earth and Planetary Science Letters*, 452:79–89, oct 2016. doi: 10.1016/j.epsl.2016.07.033.
- Michael R. Rampino, Stephen Self, and Rhodes W. Fairbridge. Can rapid climatic change cause volcanic eruptions? *Science*, 206(4420):826–829, nov 1979. doi: 10.1126/science.206.4420.826.
- Harriet Rawson, David M. Pyle, Tamsin A. Mather, Victoria C. Smith, Karen Fontijn, Stefan M. Lachowycz, and José A. Naranjo. The magmatic and eruptive response of arc volcanoes to deglaciation: Insights from southern chile. *Geology*, 44(4):251–254, feb 2016. doi: 10.1130/g37504.1.
- Alan Robock. Volcanic eruptions and climate. *Reviews of Geophysics*, 38(2):191–219, may 2000. doi: 10.1029/1998rg000054.

Harold Sackrowitz and Ester Samuel-Cahn. P values as random variables-expected p values. *The American Statistician*, 53(4):326, November 1999. ISSN 0003-1305. doi: 10.2307/2686051.

Julie C. Schindlbeck, Marion Jegen, Armin Freundt, Steffen Kutterolf, Susanne M. Straub, Maryline J. Mleneck-Vautravers, and Jerry F. McManus. 100 kyr cyclicity in volcanic ash emplacement: evidence from a 1.1 myr tephra record from the NW pacific. *Scientific Reports*, 8(1), mar 2018a. doi: 10.1038/s41598-018-22595-0.

Julie Christin Schindlbeck, Steffen Kutterolf, Susanne M. Straub, Graham D. M. Andrews, Kuo-Lung Wang, and Maryline J. Mleneck-Vautravers. One million years tephra record at IODP sites u1436 and u1437: Insights into explosive volcanism from the japan and izu arcs. *Island Arc*, 27(3), feb 2018b. doi: 10.1111/iar.12244.

Hans-Ulrich Schmincke. *Volcanism*. Springer eBook Collection. Springer, Berlin, 2004. ISBN 9783642189524.

Jacopo Selva, Laura Sandri, Matteo Taroni, Roberto Sulpizio, Pablo Tierz, and Antonio Costa. A simple two-state model interprets temporal modulations in eruptive activity and enhances multivolcano hazard quantification. *Science Advances*, 8(44), nov 2022. doi: 10.1126/sciadv.abq4415.

Gudmundur E Sigvaldason, Kristian Annertz, and Magnus Nilsson. Effect of glacier loading/deloading on volcanism: postglacial volcanic production rate of the dyngjufjöll area, central iceland. *Bulletin of Volcanology*, 54(5):385–392, jul 1992. doi: 10.1007/bf00312320.

Y. Tamura, C.J. Busby, P. Blum, G. Guèrin, G.D.M. Andrews, A.K. Barker, J.L.R. Berger, E.M. Bongiorno, M. Bordiga, S.M. DeBari, J.B. Gill, C. Hamelin, J. Jia, E.H. John, A.-S. Jonas, M. Jutzeler, M.A.C. Kars, Z.A. Kita, K. Konrad, S.H. Mahony, M. Martini, T. Miyazaki, R.J. Musgrave, D.B. Nascimento, A.R.L. Nichols, J.M. Ribeiro, T. Sato, J.C. Schindlbeck, A.K. Schmitt, S.M. Straub, M.J. Vautravers, Y., and Yang. Site u1437. In *Proceedings of the International Ocean Discovery Program*. International Ocean Discovery Program, may 2015. doi: 10.14379/iodp.proc.350.104.2015.

A. Tuel, P. Naveau, and C. M. Ammann. Skillful prediction of multidecadal variations in volcanic forcing. *Geophysical Research Letters*, 44(6):2868–2874, mar 2017. doi: 10.1002/2016gl072234.

- Alejandro Veen and Frederic P Schoenberg. Estimation of space-time branching process models in seismology using an EM-type algorithm. *J Amer Statist Assoc*, 103(482):614–624, jun 2008. doi: 10.1198/016214508000000148.
- D. Vere-Jones. On the estimation of frequency in point-process data. *Journal of Applied Probability*, 19(A):383–394, 1982. doi: 10.2307/3213577.
- Sebastian F.L. Watt, David M. Pyle, and Tamsin A. Mather. The volcanic response to deglaciation: Evidence from glaciated arcs and a reassessment of global eruption records. *Earth-Science Reviews*, 122:77–102, jul 2013. doi: 10.1016/j.earscirev.2013.03.007.

Chapter 3

On goodness-of-fit testing for self-exciting point processes

Kling, J.C.F, Vetter, M.

Submitted to the Scandinavian Journal of Statistics.

Self-exciting point processes constitute a rich class of models to describe the evolution of real world events over time. Among the most prominent models in practice are standard Poisson processes (having a constant intensity function), inhomogeneous Poisson processes (those with a deterministic but time-varying intensity process) and Hawkes processes (self-exciting point processes with a conditional intensity which depends on past observations). Such processes are used in a variety of fields such as geology (see e.g., Ogata (1978) for an early use of Hawkes process models in seismology, but also Dion-Blanc et al. (2023) for recent work on inhomogeneous Poisson processes in volcanology), neuroscience (see e.g., Burkitt (2006) for neuron models based on inhomogeneous Poisson processes), finance (see Bauwens and Hautsch (2009) for an overview on the use of point processes in finance) and telecommunication (see e.g., Pinto et al. (2015) and Rizoïu et al. (2017) for the use of Hawkes processes in social media), among many others.

From a statistical point of view, the situation is usually as follows: One has data coming from a specific class of point processes, i.e. observation times $0 < t_1 < t_2 < \dots$ over some compact interval $[0, T]$, which correspond to the event times of the underlying point process N . Statistical procedures then usually involve the estimation of an unknown parameter in the underlying model. For self-exciting point processes it is well known that the distribution of N is uniquely characterized by its conditional intensity process $\lambda(t)$, i.e. the (random) process making $N(t) - \int_0^t \lambda(s) ds$ a zero mean locally square integrable martingale with respect to the natural filtration. Hence, parametric models are usually of the form $\lambda(t) = \nu(t, \theta)$ for some $\theta \in \Theta$, where Θ is a finite-dimensional parameter space and $t \mapsto \nu(t, \theta)$ in general needs to be a suitably measurable stochastic process indexed by θ . The prime interest of the statistician then is to estimate the unknown true parameter θ_0 .

For self-exciting point processes, but also for certain models based on renewal processes, this is relatively easy as the likelihood function often is directly accessible. Therefore, e.g., Ogata (1978); Vere-Jones (1982); Chornoboy et al. (1988) were able to explicitly compute maximum likelihood estimators for certain point process models and to prove consistency as well as asymptotic normality, albeit in quite restrictive situations where either stationarity assumptions were needed or very strong assumptions on the form of the intensity process had to be made. Asymptotic considerations were then made under the condition $T \rightarrow \infty$, typically utilizing classical central limit theorems. A more flexible model for self-exciting point processes was presented recently in Chen and Hall (2013) where both the baseline intensity and the excitation function can be chosen from a large class of parametric functions. These authors proved asymptotic normality for the maximum likelihood

estimator $\hat{\theta}$ as well, but since stationarity typically fails their asymptotic setting is not based on $T \rightarrow \infty$. In fact, they work in the situation of infill asymptotics where the underlying interval $[0, T]$ remains fixed but the baseline intensity function tends to infinity in a specific way.

What is lacking, however, is a consistent goodness-of-fit test for parametric point process models. This means, the goal is not to estimate the unknown parameter θ_0 or to test certain properties of it, but rather to check whether the proposed parametric model provides a reasonable fit for the observed event times. Formally, what is missing is a sound statistical procedure which tests the null hypothesis that $\lambda(t) = \nu(t, \theta)$ for some $\theta \in \Theta$ against the alternative that there is no $\theta \in \Theta$ such that $\nu(t, \theta)$ fully describes the intensity process.

For independent and identically distributed data, the problem of testing a given parametric model is well-known and dates back to e.g. Darling (1955); Kac et al. (1955); Lilliefors (1967). The main strategy is always to first estimate the unknown parameter and to then take a suitable distance between two estimators for the unknown distribution function. The first is the parametric distribution function under the model with the unknown parameter replaced by the estimated one, and the second is a non-parametric estimator such as the empirical distribution function. The problem with these approaches, however, is that the (explicit or asymptotic) distribution of this distance is rarely known or depends on the unknown parameter in a complicated way (Durbin, 1973), so that one needs to rely on simulation methods in order to obtain asymptotic quantiles for a valid goodness-of-fit test. Two convincing solutions have been provided somewhat recently by Babu and Rao (2004); Meintanis and Swanepoel (2007) who have proven under very general assumptions that a bootstrap-based method leads to asymptotically consistent tests.

For simple point processes, however, the picture is much less clear. Both Ogata (1988); Chen and Hall (2013) mention that a formal goodness-of-fit test for these models is missing, and they propose the use of an ad-hoc method based on the fact that, if its conditional intensity function is known, then a self-exciting point process can be transformed into a standard Poisson one. To be precise, given observation times $0 = t_0 < t_1 < t_2 < \dots$ and the associated cumulative intensity process $\Lambda(t) = \int_0^t \lambda(s) ds$ it is known that the process $0 = s_0 < s_1 < s_2 < \dots$ given by $s_i = \Lambda(t_i)$ is equal in distribution to a standard Poisson process. In particular, the increments $s_i - s_{i-1}$, $i \geq 1$, equal independent standard exponential random variables.

This intuition is used to come up with the aforementioned ad-hoc method for goodness-of-fit testing. Under the null hypothesis there exists an unknown true

parameter θ_0 giving both the true intensity process $\lambda(t, \theta_0)$ as well as the true cumulative intensity process $\Lambda(t, \theta_0)$. Clearly, the above time transformation is infeasible as θ_0 is unknown, but we can replace θ_0 by its consistent estimator $\hat{\theta}$ and in turn obtain an estimator $\hat{\Lambda}(t)$ as well as event times given by $\hat{s}_i = \hat{\Lambda}(t_i)$. The proposed goodness-of-fit tests are then based on testing the null hypothesis whether the increments $\hat{s}_i - \hat{s}_{i-1}$, $i \geq 1$, behave like independent standard exponential random variables. This can be done via standard procedures. (A similar approach is proposed for renewal processes; see Bebbington and Lai, 1996; Bebbington, 2013).

The problem, however, is the same as historically for i.i.d. observations, namely that these procedures do not account for the fact that the parameter (and, hence, the cumulative intensity function) needs to be estimated. Under the null, they treat $\hat{s}_i - \hat{s}_{i-1}$ as being i.i.d. standard exponential distributed which obviously is not the case. Our main goal in this work therefore is to overcome this issue and to provide a convincing solution to the problem of goodness-of-fit testing for self-exciting point processes. In the spirit of Babu and Rao (2004); Meintanis and Swanepoel (2007) we establish a novel test which utilizes recent bootstrap techniques for point processes (Cavaliere et al., 2023). We also provide a thorough asymptotic theory which proves that this new methodology yields a consistent test, albeit only for inhomogeneous Poisson processes.

The paper is organized as follows: In Section 3.1 we introduce the formal setting of this work and explain the main idea behind our bootstrap-based goodness-of-fit test. Section 3.2 contains the statement of the main results of this work, which are the asymptotic consistency of the bootstrap-based test in the inhomogeneous Poisson case as well as a generalisation of the key theorems in Chen and Hall (2013), and we also discuss the various conditions needed to prove these claims. Sections 3.3 and 3.4 deal with a thorough simulation study as well as some empirical applications. Finally, the main structure of the proofs is presented in Section 3.5 while some additional details are gathered within the supplementary materials.

3.1 Setting

In the following we will work with the setting from Chen and Hall (2013) which is specifically tailored to allow for a formal asymptotic theory. If one thinks of the class of inhomogeneous Poisson processes, it is clear that in order to check whether a (parametric) model is appropriate or not one needs to potentially have infinitely many observations around every time point t as it is otherwise not obvious to check whether the proposed function λ is reasonable at t or not. A similar

reasoning applies to processes with self-exciting components as well. The solution of Chen and Hall (2013) to this problem is to work with infill asymptotics; e.g., to assume that, for any given n , we have observations $0 = t_0^n < t_1^n < t_2^n < \dots$ associated with a self-exciting point process N_n over a compact interval, which we choose to be $[0, 1]$ from now on. The corresponding intensity process is then given by $\lambda_n(t) = a_n\mu(t) + \int_{[0,t)} g(t-s)dN_n(s)$, where $a_n \rightarrow \infty$ denotes a sequence of known positive constants and $\mu(\cdot)$ and $g(\cdot)$ are unknown functions (satisfying additional conditions) which represent the deterministic part and the self-exciting part of the intensity process, respectively. Under the null hypothesis the above sequence of intensity processes belongs to a given parametric family, i.e. it is assumed that there exists some space Θ parametrizing $\mu(\cdot)$ and $g(\cdot)$, and that there exists some $\theta \in \Theta$ such that

$$H_0 : \lambda_n(t) = \lambda_n(t, \theta) = a_n\mu(t, \theta) + \int_{[0,t)} g(t-s, \theta)dN_n(s) \quad (3.1)$$

holds true for each n .

Loosely speaking, under the null hypothesis there exists a true parameter $\theta_0 \in \Theta$ such that the intensity process (and, hence, the point process itself) follows a shape given by the baseline function $\mu(\cdot, \theta_0)$ and the excitation function $g(\cdot, \theta_0)$, while the factor a_n allows for a growing number of events as $n \rightarrow \infty$ and thus makes an asymptotic theory from observations over $[0, 1]$ possible. In Chen and Hall (2013) this model is used for asymptotic inference on the true parameter, i.e. if H_0 holds and θ_0 is the true parameter then the authors prove under relatively mild conditions that the maximum likelihood estimator $\hat{\theta}_n$ is consistent for θ_0 and asymptotically normal.

Our aim is to provide a consistent goodness-of-fit test for which we utilize the fact that the point process given by $0 = s_0^n < s_1^n < s_2^n < \dots$ with $s_i^n = \Lambda_n(t_i^n, \theta_0)$ is equal in distribution to a standard Poisson process. Here, $\Lambda_n(t, \theta_0)$ denotes the cumulative intensity process associated with $\lambda_n(t, \theta_0)$. As noted in the introduction, a natural idea is to replace the unknown process $\Lambda_n(t, \theta_0)$ by an estimated version $\Lambda_n(t, \hat{\theta}_n)$. This estimated process $\Lambda_n(t, \hat{\theta}_n)$ can then be interpreted as a near optimal fit to the unknown process $\Lambda_n(t, \theta_0)$ within the parametric model, and under the null hypothesis the estimated increments $\hat{s}_i^n - \hat{s}_{i-1}^n$, $i = 1, \dots, N_n(1)$, based on the transform $\hat{s}_i^n = \Lambda_n(t_i^n, \hat{\theta}_n)$, should be reasonably close to independent standard exponential random variables.

There exist many tests to check whether a given set of observations was generated by a specific distribution, and in this work we will discuss a version based

on empirical Laplace transforms, although many other statistics (including more standard ones like the Kolmogorov-Smirnov approach) would, in principle, work as well. Critical values for the resulting test statistic will then be obtained from a bootstrap procedure explained in detail below. Its validity (i.e. consistency under the null hypothesis) will be proven, albeit only for inhomogeneous Poisson processes. For notational convenience we will often drop the index n and simply write e.g. t_i instead of t_i^n .

In the following, let $k_n(u, \theta, r, s) = \exp(-u \int_r^s \lambda_n(t, \theta) dt)$, with $u \geq 0$, and set

$$\begin{aligned} L_n(u, \hat{\theta}_n) &= \frac{1}{N_n(1)} \sum_{i \geq 1} k_n(u, \hat{\theta}_n, t_{i-1}, t_i) 1_{\{t_i \leq 1\}} \\ &= \frac{1}{N_n(1)} \sum_{i \geq 1} \exp\left(-u(\Lambda_n(t_i, \hat{\theta}_n) - \Lambda_n(t_{i-1}, \hat{\theta}_n))\right) 1_{\{t_i \leq 1\}} \end{aligned}$$

where $\hat{\theta}_n$ denotes the maximum likelihood estimator for the true parameter θ_0 under H_0 as discussed in Chen and Hall (2013). By construction, $L_n(u, \hat{\theta}_n)$ plays the role of an empirical Laplace transform based on the estimated increments $\hat{s}_i^n - \hat{s}_{i-1}^n$, $i = 1, \dots, N_n(1)$. Hence, under the null hypothesis it should be close to the Laplace transform $L(u) = (1 + u)^{-1}$ of a standard exponential variable. As the (random) number of observations $N_n(1)$ is proportional to a_n , a reasonable test statistic for H_0 is given by $\sqrt{a_n} \|G_n\|$, where $G_n(u) = L_n(u, \hat{\theta}_n) - L(u)$, and $\|h\|^2 = \int_0^\infty h^2(u) \beta(u) du$, where β is a positive and integrable weight function. Note that the set

$$\mathcal{H} = \left\{ h : [0, \infty) \rightarrow \mathbb{R} \mid h \text{ is continuous with } \int_0^\infty h^2(u) \beta(u) du < \infty \right\} \quad (3.2)$$

with the usual scalar product, $\langle h_1, h_2 \rangle = \int_0^\infty h_1(u) h_2(u) \beta(u) du$, defines a separable Hilbert space.

Recall that $L_n(u, \hat{\theta}_n)$ does not equal the empirical Laplace transform of i.i.d. standard exponential variables even under the null hypothesis, as the true cumulative intensity process $\Lambda_n(t, \theta_0)$ is unknown and needs to be estimated based on $\hat{\theta}_n$. Hence, asymptotic critical values for $\sqrt{a_n} \|G_n\|$ are unknown, and in the spirit of Babu and Rao (2004); Meintanis and Swanepoel (2007) we propose a bootstrap procedure to estimate these critical values. This procedure mimics how $\sqrt{a_n} \|G_n\|$ is obtained and accounts for the fact that the distinction between the true unknown parameter yielding the observations and the estimated parameter used to calculate the time transformation needs to be taken into account.

Precisely, we propose the following strategy: For all $b = 1, \dots, B$, simulate a

point process $\{t_i^{*,b} \mid i = 0, 1, \dots\}$ according to the intensity process $\lambda_n(t, \hat{\theta}_n)$ and the corresponding cumulative intensity process $\Lambda_n(t, \hat{\theta}_n)$, for which both variants of the proposed bootstrap strategy in Cavaliere et al. (2023) can be used. Note specifically that, in the case of inhomogeneous Poisson processes, the simulation mimics the time transformation from above, i.e. one simulates a standard Poisson process $0 = s_0^{*,b} < s_1^{*,b} < s_2^{*,b} < \dots$ and then transforms the event times to $t_i^{*,b} = \Lambda_n^{-1}(s_i^{*,b}, \hat{\theta}_n)$. Based on the simulated point process $\{t_i^{*,b} \mid i = 0, 1, \dots\}$ over $[0, 1]$ one then reproduces how the original test statistic is obtained. First, one estimates $\hat{\theta}_n^{*,b}$ from $\{t_i^{*,b} \mid i = 0, 1, \dots\}$ via maximum likelihood and computes $\hat{s}_i^{*,b} = \Lambda_n(t_i^{*,b}, \hat{\theta}_n^{*,b})$. Then

$$L_n(u, \hat{\theta}_n^{*,b}) = \frac{1}{N_n^{*,b}(1)} \sum_{i \geq 1} \exp \left(-u(\Lambda_n(t_i^{*,b}, \hat{\theta}_n^{*,b}) - \Lambda_n(t_{i-1}^{*,b}, \hat{\theta}_n^{*,b})) \right) 1_{\{t_i^{*,b} \leq 1\}}$$

and $G_n^{*,b}(u) = L_n(u, \hat{\theta}_n^{*,b}) - L(u)$ are computed in exactly the same way as $L_n(u, \hat{\theta}_n)$ and $G_n(u)$. Finally, one uses the empirical quantiles of $\sqrt{a_n} \|G_n^{*,b}\|$, $b = 1, \dots, B$, as critical values which should approximate the unknown true critical values of $\sqrt{a_n} \|G_n\|$ as $B \rightarrow \infty$. Note that a feasible test statistic can be constructed easily without the knowledge of a_n .

To summarize, the only difference regarding the generation of $\sqrt{a_n} \|G_n\|$ and the ones of $\sqrt{a_n} \|G_n^{*,b}\|$, $b = 1, \dots, B$, regards the distribution of the underlying point process. Under the null hypothesis the parameter is θ_0 for $\sqrt{a_n} \|G_n\|$, whereas the bootstrapped processes are generated according to $\hat{\theta}_n$ (which estimates θ_0 consistently). Intuitively it is thus clear that this bootstrap strategy leads to asymptotically valid critical values if a certain continuity property of the distribution of $\sqrt{a_n} \|G_n\|$ with respect to the parameter θ generating the original point process is satisfied. This will be made precise below.

3.2 Results

Proving consistency of the bootstrap procedure equals showing that the empirical quantiles obtained above converge (in a certain sense) to the unknown asymptotic quantiles of $\sqrt{a_n} \|G_n\|$ if the null hypothesis holds. Hence, from now on we assume that there exists $\theta_0 \in \Theta$ such that $\lambda_n(t) = a_n \mu(t, \theta_0) + \int_{[0,t)} g(t-s, \theta_0) dN_n(s)$ holds true. A natural goal is to prove

$$\lim_{n \rightarrow \infty, B \rightarrow \infty} \mathbb{P} \left(\sqrt{a_n} \|G_n\| \geq (F_n^B)^{-1}(1 - \alpha) \right) = \alpha \quad (3.3)$$

for any $\alpha \in (0, 1)$, where $F_n^B(x) = \frac{1}{B} \sum_{b=1}^B 1_{\{\sqrt{a_n} \|G_n^{*,b}\| \leq x\}}$, and $(F_n^B)^{-1}$ denotes its generalized inverse.

In order to deduce (3.3) we will rely on previous results from Bücher and Kojadinovic (2018); Van Der Vaart (1998). Let us start with some additional notation: Given is a series of experiments $(\mathcal{X}_n, \mathcal{B}_n, \mathcal{P}_n)$ with $\mathcal{P}_n = \{P_{\theta,n} \mid \theta \in \Theta\}$ for some parameter space $\Theta \subset \mathbb{R}^d$ and we regard any $x_n \in \mathcal{X}_n$ as a sample of the original point process. Associated with these samples is the maximum likelihood estimator $\hat{\theta}_n = f_n(x_n)$ as well as $\sqrt{a_n} \|G_n\| = k_n(x_n)$ whose distribution we call $V_{\theta,n}$. We will later work under conditions which grant consistency and asymptotic normality of the estimator $\hat{\theta}_n$ for the unknown true parameter θ_0 , invoking the results from Chen and Hall (2013). See in particular the more general Lemma 3.2.3(b) later.

Now, Lemma 4.2 in Bücher and Kojadinovic (2018) states a sufficient condition to deduce (3.3), and it boils down to checking two separate conditions. On one hand, one needs to show that their Condition 4.1 holds true, i.e. for any fixed θ_0 one needs weak convergence of $\sqrt{a_n} \|G_n\|$ towards a limiting random variable with a continuous distribution function. In other words, setting d as the bounded Lipschitz metric which metrizes weak convergence, one has to show

$$\lim_{n \rightarrow \infty} d(V_{\theta_0,n}, V_{\theta_0}) = 0 \quad \text{for all } \theta_0 \in \Theta, \quad (3.4)$$

where V_{θ_0} is a distribution on \mathbb{R} with a continuous distribution function. The other condition is any of the equivalent statements in their Lemma 2.2, part (c) being the one used here. In accordance with the notation from above, a generic bootstrap sample is based on simulating according to $P_{\hat{\theta}_n,n}$, and we obtain both $\hat{\theta}_n^*$ and $\sqrt{a_n} \|G_n^*\|$ by applying the functions f_n and g_n to the bootstrap sample. We hence denote the conditional distribution of $\sqrt{a_n} \|G_n^*\|$, as it is based on the estimator $\hat{\theta}_n$, by $V_{\hat{\theta}_n,n}$, and Lemma 2.2(c) then becomes proving $d(V_{\hat{\theta}_n,n}, V_{\theta_0}) \xrightarrow{P_{\theta_0,n}} 0$ for all $\theta_0 \in \Theta$.

By setting $\Phi_{\theta_0,n}(h) = d(V_{\theta_0+h/\sqrt{a_n,n}}, V_{\theta_0})$, we get the equivalent formulation $\Phi_{\theta_0,n}(\sqrt{a_n}(\hat{\theta}_n - \theta_0)) \xrightarrow{P_{\theta_0,n}} 0$ for all $\theta_0 \in \Theta$, and, in the spirit of Exercise 23.5 in Van Der Vaart (1998), a sufficient condition to deduce this convergence is to show

$$\lim_{n \rightarrow \infty} d(V_{\theta_0+h_n/\sqrt{a_n,n}}, V_{\theta_0}) = 0 \quad \text{for all } \theta_0 \in \Theta, \text{ and all } h_n \rightarrow h, \quad (3.5)$$

or equivalently $\lim_{n \rightarrow \infty} \Phi_{\theta_0,n}(h_n) = \Phi(h) \equiv 0$ for all $\theta_0 \in \Theta$ and all $h_n \rightarrow h$. Indeed, utilizing the asymptotic normality $\lim_{n \rightarrow \infty} d(\sqrt{a_n}(\hat{\theta}_n - \theta_0), N_{\theta_0}) = 0$ with $N_{\theta_0} \sim \mathcal{N}(0, \mathcal{I}(\theta_0)^{-1})$ (Theorem 2 in Chen and Hall, 2013) and the extended

continuous mapping theorem (Theorem 18.11 in Van Der Vaart, 1998), for any $\theta_0 \in \Theta$ we then can first conclude the weak convergence of $\Phi_{\theta_n,n}(\sqrt{a_n}(\hat{\theta}_n - \theta_0))$ towards the constant $\Phi(N_{\theta_0}) = 0$ and then convergence to zero in $P_{\theta_0,n}$ -probability afterwards.

Hence, besides checking the conditions for an application of Theorem 2 in Chen and Hall (2013), what remains in order to prove (3.3) is to show (3.4) and (3.5). In fact, we will prove the stronger statement

$$\lim_{n \rightarrow \infty} d(V_{\theta_n,n}, V_{\theta_0}) = 0 \quad \text{for all } \theta_0 \in \Theta, \text{ and all } \theta_n \rightarrow \theta_0 \quad (3.6)$$

from which both assertions obviously follow.

Before we come to the main result of our work, we will give some conditions and state a few auxiliary claims which generalize some results from Chen and Hall (2013) and might be of independent interest. Note that while the strategy of proving (3.6) works for all self-exciting processes, our main restriction will be that a full proof is only provided for inhomogeneous Poisson processes in the sense below.

Condition 3.2.1. *Suppose the following conditions to hold:*

- (a) $\Theta \subset \mathbb{R}^d$ is a compact parameter space whose interior is connected and contains a d -dimensional open ball which contains the limiting (true) parameter θ_0 .
- (b) $a_n \rightarrow \infty$ is a known sequence, $\theta_n \rightarrow \theta_0$ denotes a sequence of unknown parameters, and for each n a point process $0 = t_0^n < t_1^n < t_2^n < \dots$ is observed over $[0, 1]$ according to the intensity function $\lambda_n(t) = \lambda_n(t, \theta_n) = a_n \mu(t, \theta_n)$ and associated cumulative intensity function $\Lambda_n(t) = \Lambda_n(t, \theta_n) = \int_0^t a_n \mu(s, \theta_n) ds$. We also set $C(t, \theta_n) = \int_0^t \mu(s, \theta_n) ds$.
- (c) The function $(t, \theta) \mapsto \mu(t, \theta)$ is uniformly bounded away from zero, i.e., $\inf_{t \in [0, 1], \theta \in \Theta} |\mu(t, \theta)| > 0$, and it is two times continuously differentiable with uniformly bounded zeroth, first and second derivatives.
- (d) $\beta : [0, \infty) \rightarrow [0, \infty)$ is a known integrable function and defines a Hilbert space \mathcal{H} as in (3.2).

The first lemma essentially generalizes results from Chen and Hall (2013). As mentioned before, we will work under conditions which grant consistency and asymptotic normality of $\hat{\theta}_n$ as an estimator for θ_0 whenever the latter is the true unknown parameter. However, for a proof of the bootstrap procedure to work we need to discuss the slightly more general situation stated in Condition 3.2.1, namely the one where the true parameter at stage n is θ_n , and these parameters do not have to

equal θ_0 but only have to converge to it. In this more general case, which obviously contains the case of a constant parameter, we will need a version of asymptotic normality (and, hence, consistency) as well.

This result will be proved in the more general situation of truly self-exciting processes. Hence, we need a more comprehensive set of assumptions as well as additional notation.

Condition 3.2.2. Assume Condition 3.2.1 with item (b) modified to

(b) $a_n \rightarrow \infty$ is a known sequence, $\theta_n \rightarrow \theta_0$ denotes a sequence of unknown parameters, and for each n a point process $0 = t_0^n < t_1^n < t_2^n < \dots$ is observed over $[0, 1]$ according to the intensity process

$$\lambda_n(t) = \lambda_n(t, \theta_n) = a_n \mu(t, \theta_n) + \int_0^t g(t-u, \theta_n) dN_n(u)$$

and the associated cumulative intensity process

$$\Lambda_n(t) = \Lambda_n(t, \theta_n) = \int_0^t \left(a_n \mu(u, \theta_n) + \int_0^u g(u-s, \theta_n) dN_n(s) \right) du.$$

Note that the mean intensity process associated with $\lambda_n(t, \theta)$ satisfies the linear Volterra equation $\eta_n(t, \theta) = a_n \mu(t, \theta) + \int_0^t g(t-u, \theta) \eta_n(u, \theta) du$. We then define $c(t, \theta)$ via $a_n c(t, \theta) = \eta_n(t, \theta)$ and also write $C(t, \theta) = \int_0^t c(u, \theta) du$.

We also additionally assume:

(e) The function $(t, \theta) \mapsto g(t, \theta)$ is two times continuously differentiable with uniformly bounded zeroth, first and second derivatives.

(f) The matrix-valued function

$$\mathcal{I}(\theta) = \int_0^1 \frac{\left(\partial_\theta \mu(t, \theta) + \int_0^t \partial_\theta g(t-u, \theta) c(u, \theta) du \right)^{\otimes 2}}{\mu(t, \theta) + \int_0^t g(t-u, \theta) c(u, \theta) du} \quad (3.7)$$

is non-singular at the true parameter value θ_0 . In the d -dimensional situation we use the notation $\partial_\theta = \partial / \partial \theta$ and $\partial_\theta^{\otimes 2} = \partial^2 / \partial \theta \partial \theta^T$ in accordance with Chen and Hall (2013).

Notice that an inhomogeneous Poisson process is a degenerate case of a self-exciting process where $g = 0$, therefore any inhomogeneous Poisson process satisfying Condition 3.2.1 will automatically satisfy Condition 3.2.2.

Before we state the first lemma, we finally give a preparation which is borrowed from the proof of Theorem 2 in Chen and Hall (2013) and provides a typical representation for $\sqrt{a_n}(\hat{\theta}_n - \theta_n)$ when maximum likelihood estimation is used. For $S_n(\theta) = \int_0^1 U_n(t, \theta) dM_n(t, \theta)$ with

$$U_n(t, \theta) = \frac{\partial_\theta \mu(t, \theta) + \int_0^t \partial_\theta g(t-u, \theta) da_n^{-1} N_n(u)}{\mu(t, \theta) + \int_0^t g(t-u, \theta) da_n^{-1} N_n(u)} \quad (3.8)$$

and

$$M_n(t, \theta) = N_n(t) - \int_0^t \left(a_n \mu(u, \theta) + \int_0^u g(u-s, \theta) dN_n(s) \right) du \quad (3.9)$$

we have

$$0 = a_n^{-1/2} S_n(\hat{\theta}_n) = a_n^{-1/2} S_n(\theta_n) + a_n^{-1} \partial_\theta S_n(\theta)|_{\theta=\tilde{\theta}_n} a_n^{1/2} (\hat{\theta}_n - \theta_n) \quad (3.10)$$

for some intermediate $\tilde{\theta}_n$.

Lemma 3.2.3. *Suppose that Condition 3.2.2 holds and recall that $N_n(1)$ denotes the random number of events over $[0, 1]$.*

- (a) *We have $\sup_{t \in [0, 1]} |a_n^{-1} N_n(t) - C(t, \theta_0)| \xrightarrow{\mathbb{P}} 0$ as well as $N_n(1)/\kappa_n \xrightarrow{\mathbb{P}} 1$ and $\mathbb{E}(N_n(1))/\kappa_n \rightarrow 1$, with $\kappa_n = a_n C(1, \theta_0)$.*
- (b) *Let $\hat{\theta}_n$ denote the maximum likelihood estimator for θ_n based on the observations $0 = t_0^n < t_1^n < t_2^n < \dots$ over $[0, 1]$. Then $\sqrt{a_n}(\hat{\theta}_n - \theta_n) \xrightarrow{\mathcal{L}} \mathcal{N}(0, \mathcal{I}(\theta_0)^{-1})$, with $\mathcal{I}(\theta_0)$ as in Condition 3.2.2(f).*
- (c) *With $\mathcal{I}(\theta_0)$ as above we have $a_n^{-1} \partial_\theta S_n(\theta)|_{\theta=\tilde{\theta}_n} \xrightarrow{\mathbb{P}} -\mathcal{I}(\theta_0)$.*

We are now in a position to formulate the main theorem of this work. As noted before, and in contrast to Lemma 3.2.3, it will only be stated for inhomogeneous Poisson processes in the sense of Condition 3.2.1.

Theorem 3.2.4. *Let*

$$k_n(u, \theta, r, s) = \exp \left(-u \int_r^s a_n \mu(t, \theta) dt \right), \quad u \geq 0,$$

and let $\hat{\theta}_n$ be the maximum likelihood estimator for θ_n based on the observations

$0 = t_0^n < t_1^n < t_2^n < \dots$ over $[0, 1]$. Set

$$L_n(u, \hat{\theta}_n) = \frac{1}{N_n(1)} \sum_{i \geq 1} k_n(u, \hat{\theta}_n, t_{i-1}^n, t_i^n) 1_{\{t_i^n \leq 1\}}, \quad L(u) = (1 + u)^{-1}.$$

Then, under Condition 3.2.1, $\sqrt{a_n} \|G_n\|$ with $G_n(u) = L_n(u, \hat{\theta}_n) - L(u)$ converges weakly to a limiting distribution V_{θ_0} with a continuous distribution function.

As a direct consequence of Lemma 3.2.3 and Theorem 3.2.4 we obtain consistency of the bootstrap procedure.

Corollary 3.2.5. *Under Condition 3.2.1 we have*

$$\lim_{n \rightarrow \infty, B \rightarrow \infty} \mathbb{P} \left(\sqrt{a_n} \|G_n\| \geq (F_n^B)^{-1}(1 - \alpha) \right) = \alpha$$

for any $\alpha \in (0, 1)$.

Remark 3.2.6. (a) As noted before, to base a goodness-of-fit test on Laplace transforms is only one of many options, as essentially all methods to test the difference between two distributions are in play. We use this specific method essentially only for the reason that it allows for easy differentiability with respect to various parameters, a fact which is heavily exploited in the proof of Theorem 3.2.4. Empirically, there is no problem in choosing other variants such as the Kolmogorov-Smirnov distance which performs equally well in simulations.

(b) We have also conducted further simulations which check that the procedure is not only valid for the class of (inhomogeneous) Poisson processes, but it also works for other self-exciting processes such as Hawkes processes (which are explicitly discussed in Section 3.3), Hawkes processes with varying baseline intensity, renewal processes, and the two-stage model proposed in Selva et al. (2022). In all cases, the general procedure for the bootstrap-based test is the same, with the differences only residing in the specific algorithms for estimating the unknown parameter and in the calculation of the transform $t_i \mapsto s_i = \Lambda(t_i)$.

(c) While the main strategy of the proof of Theorem 3.2.4 as laid out in Section 3.5.2 should remain valid for general self-exciting point processes, we heavily rely on a variety of properties of inhomogeneous Poisson processes when it comes to detailed derivations. In particular, this regards distributional aspects in the proof of Lemma 3.5.7 as well as a simplified form of U_n from (3.8) which

is exploited in the proof of Theorem 3.5.9. Finding an alternative proof which also works e.g. for Hawkes processes is an important topic for future research.

3.3 Simulation study

This section aims to assess the performance of our bootstrap-based goodness-of-fit test by investigating its type I error and power in different settings and comparing it with a popular alternative method.

Ogata (1988) presented several procedures based on residual analysis to assess the fit of a model to the data. One of them relies on the fact that, if t_1, \dots, t_n are event times originating from a process $N(t)$ with corresponding conditional intensity process $\lambda(t)$, then the random variables s_1, \dots, s_n , with $s_i = \int_0^{N(t_i)} \lambda(s) ds$, are equal in distribution to the event times of a Poisson process. Therefore, a good strategy would be simply to test if the interevent times of the time transformed process follow a unit exponential distribution.

In the situation of goodness-of-fit testing, however, where the intensity process λ depends on a parameter θ , the transformation $(t_1, \dots, t_n) \rightarrow (s_1, \dots, s_n)$ can only be calculated using an estimator $\hat{\theta}$ for the true parameter θ_0 . Bebbington (2013) provides an implementation of such a test, which will be used here as a reference for the performance of our method and to show to which extent parameter estimation error can affect the results.

3.3.1 Type I error

In this section we discuss the type I error for both methods and check to which percentage the null hypothesis was incorrectly rejected. The following procedure was carried out using a level of 0.05.

- Algorithm 3.3.1.**
1. *Simulate 1000 data sets from a known process with fixed parameters.*
 2. *Perform the tests for each simulation, correctly assuming that the null hypothesis is true.*
 3. *Compute the percentage of times the null hypothesis was rejected with level 0.05.*

Figure 3.1 shows the result of six applications of Algorithm 3.3.1 for Poisson processes on the interval $[0, 1]$, each corresponding to different parameters. We

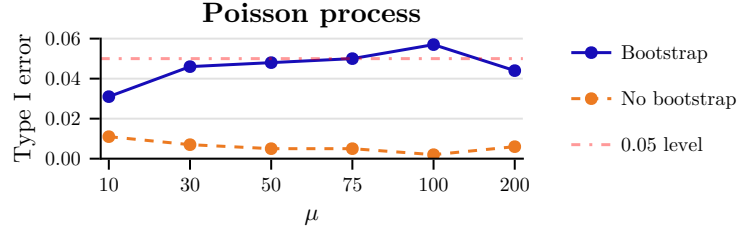


Figure 3.1: Type I error for the bootstrap and non-bootstrap based tests for Poisson processes with different parameters.

can see that our bootstrap-based test, when performed with 1000 bootstrap samples, maintains a level close to 0.05 for processes with an expected number of events of as few as 30. The non-bootstrap-based test, in contrast, is not consistent as it is very conservative and rarely rejects the null hypothesis. This behaviour might also point towards a potential lack of power.

This pattern persists also for more general Hawkes processes, which are considerably more complex. For the next tests, we consider Hawkes processes with an exponential activation function. Figure 3.2 shows the results of the procedure for several parameter configurations. This class of Hawkes processes has three parameters: μ , the constant baseline intensity; α , the amplitude of the increase in intensity following each event; and β , the decay rate. For a realization $0 < t_1 < \dots < t_n$ of a Hawkes process, its conditional intensity function is given by $\lambda(t; \mu, \alpha, \beta) = \mu + \sum_{t_i < t} \alpha e^{-\beta(t-t_i)}$.

Of particular importance is the branching factor α/β , which is the expected number of events a single event causes due to the self-exciting component. In Figure 3.2, the parameter μ and the ratio α/β were kept fixed in each subfigure. By increasing the parameter α the response of the intensity function to an event happens faster and therefore the behaviour is less similar to a Poisson process.

In all tests, the expected number of events is approximately equal, and we can see that a reasonably good level is maintained for all configurations. This behaviour is in sharp contrast to the performance of the test without bootstrap.

3.3.2 Power

The next step is to test the power of the methods. The procedure is similar to Algorithm 3.3.1, but now two distinct models A and B are needed. The idea is to test how effective the tests are in rejecting incorrect hypotheses.

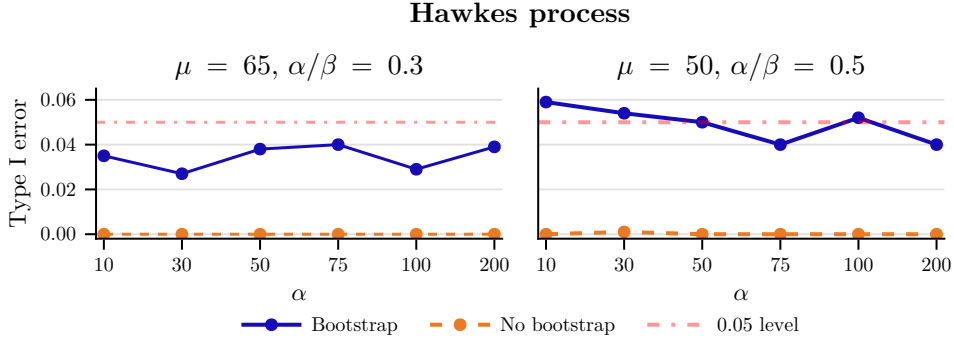


Figure 3.2: Type I error for both tests with respect to Hawkes processes.

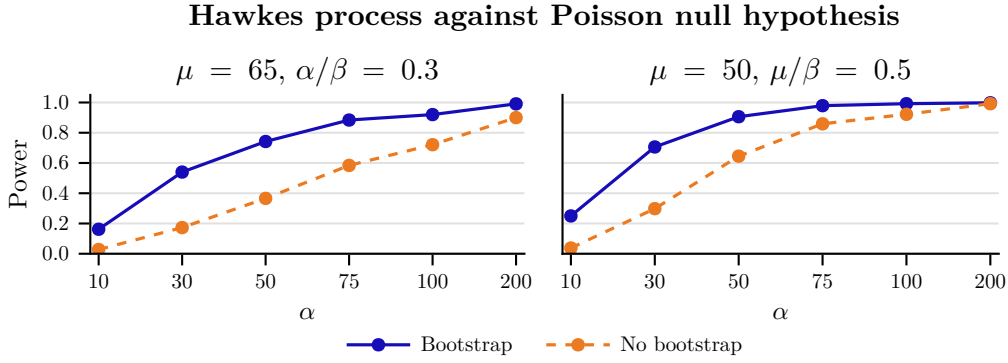


Figure 3.3: Power of tests for simulated Hawkes processes with the null hypothesis that these are Poisson processes.

- Algorithm 3.3.2.**
1. Simulate 1000 data sets from a known process A with fixed parameters.
 2. Perform the tests for each simulation, incorrectly assuming that the data stems from some process B .
 3. Compute the percentage of times the null hypothesis was rejected with level 0.05.

In Figure 3.3, the power is plotted for a Hawkes process as model A and a Poisson process as model B . In essence, this graphic shows how good each of the tests are in differentiating Poisson from Hawkes processes.

It can be seen that both tests perform better for larger values of the parameter α and the branching factor α/β , but the bootstrap-based approach is clearly superior.

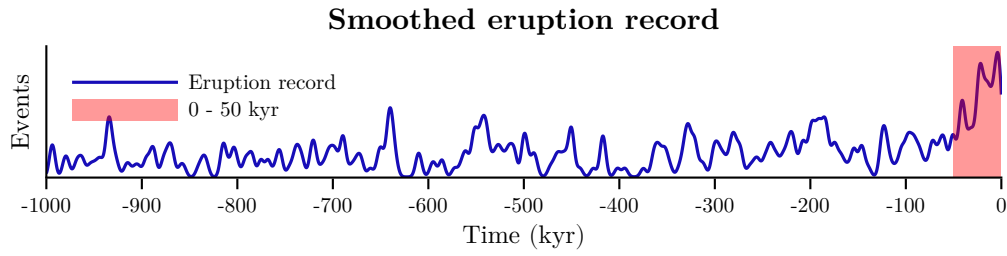


Figure 3.4: Eruption record smoothed with a Gaussian kernel ($\sigma = 3000$) and highlighted period excluded from the analysis.

3.4 Empirical application

It is widely accepted that volcanism can affect local and global climate, primarily through the injection of aerosols into the stratosphere (Robock, 2000). A less known and still being explored hypothesis is that climate variations may influence volcanism. The proposed mechanism for this effect is the stress change in Earth's crust due to variations in sea level and thickness of the ice sheets (e.g., Rampino et al., 1979; Jellinek et al., 2004; Cooper et al., 2018).

Kutterolf et al. (2013) presents a compilation of eruption records from multiple sites around the Pacific Ring of Fire over the last 1 million years. These records are based on tephra layers from cores drilled on the ocean floor which are identified and dated. Younger layers tend to suffer less from degradation than older ones, possibly causing an artificial peak of volcanic activity. To mitigate this bias, eruptions dated within the first 50 thousand years were excluded from the analysis. This potential bias can be seen in Figure 3.4, where we show the entire eruption records smoothed with a Gaussian kernel.

To determine whether glacial cycles affect the eruptive process, the data set was split into two groups based on the sites' latitudes. The first part contains eruptions from tropical regions that were not glaciated (Peru, Ecuador, Central America, Philippines, and Tonga). The second comprises sites in extratropical sites in both hemispheres which were more likely subjected to glaciation (New Zealand, Nankai Trough, Kamchatka, Alaska, and the Aleutian Basin and Arc).

Applying our bootstrap-based goodness-of-fit test to both data sets with the hypothesis that they are distributed as Poisson processes shows distinctively different patterns. While for the tropical sites the returned p-value is 0.44, suggesting that a Poisson process is a good fit for the data, the p-value for the extratropical sites

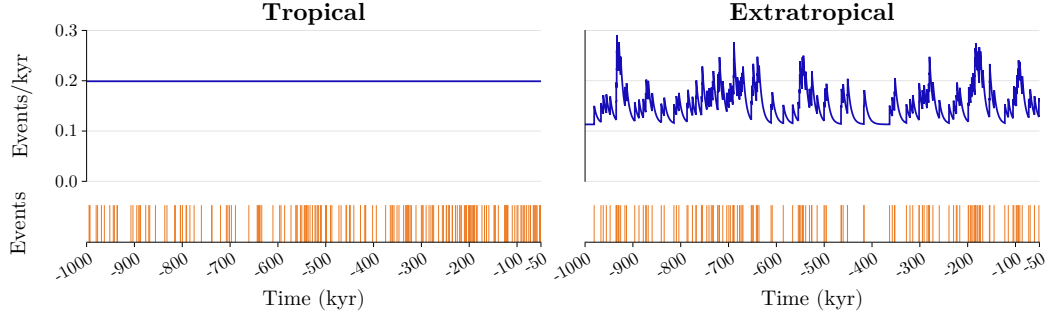


Figure 3.5: Estimated CIF for tropical (left) under the Poisson assumption and extratropical (right) sites using a Hawkes process.

is 0.03. For the hypothesis that the extratropical eruptions stem from a Hawkes process as in Section 3.3.1, in contrast, the p-value of the test is 0.80. The estimated conditional intensity functions for both data sets are shown in Figure 3.5.

These results show that, while tropical eruptions occurred uniformly during the period, in the extratropical regions there is a tendency for events to cluster in time, suggesting different mechanisms governing the processes. Note that the non-bootstrap-based test from Section 3.3, when applied to the hypothesis that the extratropical data set is distributed as a Poisson process, returns a p-value of 0.42, in clear disagreement with the result for the bootstrap-based test. This might be a consequence of the non-bootstrap based being very conservative as discussed previously.

3.5 Proofs

In this section, the outline of the proofs for the results stated in Section 3.2 will be provided. A number of auxiliary results are used, but their proofs are left in the Supplementary Materials for the reader interested in all the details.

3.5.1 Proof of Lemma 3.2.3

We will start with a few auxiliary results for which our notation mostly follows the one in Chen and Hall (2013). We assume Condition 3.2.2 in all cases.

Lemma 3.5.1. *The function $c(t, \theta)$ is uniformly bounded in $t \in [0, 1]$ and $\theta \in \Theta$.*

Lemma 3.5.2. *For the function $c(t, \theta)$ as defined in Condition 3.2.2(b), we have $\sup_{t \in [0, 1]} |c(t, \theta_n) - c(t, \theta_0)| \rightarrow 0$.*

With these results, we are now in a position to prove Lemma 3.2.3(a). For the first claim, one can use the inequality

$$|a_n^{-1}N_n(t) - C(t, \theta_0)| \leq |a_n^{-1}N_n(t) - C(t, \theta_n)| + |C(t, \theta_n) - C(t, \theta_0)|,$$

and deduce $\sup_{t \in [0,1]} |a_n^{-1}N_n(t) - C(t, \theta_n)| \xrightarrow{\mathbb{P}} 0$ along the lines of Theorem 1 from Chen and Hall (2013) by replacing θ_0 by θ_n in all occurrences, and redefining $\bar{\mu}$ and \bar{g} as

$$\bar{\mu} = \sup_{\substack{t \in [0,1] \\ \theta \in \Theta}} \mu(t, \theta) \quad \text{and} \quad \bar{g} = \sup_{\substack{t \in [0,1] \\ \theta \in \Theta}} g(t, \theta).$$

Furthermore,

$$\sup_{t \in [0,1]} |C(t, \theta_n) - C(t, \theta_0)| = \sup_{t \in [0,1]} \left| \int_0^1 c(u, \theta_n) - c(u, \theta_0) du \right| \rightarrow 0$$

is a consequence of Lemma 3.5.2.

It is then easy to deduce

$$\left| \frac{N_n(1)}{\kappa_n} - 1 \right| = \frac{|N_n(1) - a_n C(1, \theta_0)|}{a_n C(1, \theta_0)} = \frac{|a_n^{-1}N_n(1) - C(1, \theta_0)|}{C(1, \theta_0)} \xrightarrow{\mathbb{P}} 0$$

from the fact that μ is uniformly bounded from below, as well as

$$\frac{\mathbb{E}(N_n(1))}{\kappa_n} - 1 = \frac{\int_0^1 a_n (c(t, \theta_n) - c(t, \theta_0)) dt}{a_n \int_0^1 c(t, \theta_0) dt} = \frac{\int_0^1 (c(t, \theta_n) - c(t, \theta_0)) dt}{\int_0^1 c(t, \theta_0) dt} \rightarrow 0$$

utilizing that $\eta(t, \theta_n) = a_n c(t, \theta_n)$ is the mean intensity function of the point process.

For the remaining parts of Lemma 3.2.3 we first state and prove a few corollaries from the previous results. The first is a direct consequence of Lemma 3.5.2 and uniform boundedness of g and its derivatives and hence stated without proof.

Corollary 3.5.3. *We have*

$$\sup_{\substack{t \in [0,1] \\ \theta \in \Theta}} \left| \int_0^t g(t-u, \theta) c(t, \theta_n) du - \int_0^t g(t-u, \theta) c(t, \theta_0) du \right| \rightarrow 0,$$

and similarly with g replaced by $\partial_\theta g$ or $\partial_\theta^{\otimes 2} g$.

Corollary 3.5.4. *For every fixed $\theta \in \Theta$ we have*

$$\sup_{t \in [0,1]} \left| \int_0^t g(t-u, \theta) da_n^{-1}N_n(u) - \int_0^t g(t-u, \theta) c(u, \theta_n) du \right| \xrightarrow{\mathbb{P}} 0,$$

and similarly for other functions with uniformly bounded derivatives.

Proof. By using integration by parts, we get

$$\begin{aligned} & \int_0^t g(t-u, \theta) (da_n^{-1} N_n(u) - c(u, \theta_n) du) \\ &= (a_n^{-1} N_n(t) - C(t, \theta_n)) g(0, \theta) + \int_0^t (a_n^{-1} N_n(u) - C(u, \theta_n)) g'(t-u, \theta) du \end{aligned}$$

where g' denotes the derivative of g with respect to t . The claim can then be deduced easily from Lemma 3.2.3(a) and uniform boundedness of all functions involved. \square

To prove the remaining two claims in Lemma 3.2.3, we need to first establish the consistency of $\hat{\theta}_n$ as an estimator for θ_0 . For this proof we will use Theorem 5.9 in Van Der Vaart (1998), with the following additional notation of

$$\begin{aligned} s_n(\theta) &= \int_0^1 \frac{\partial_\theta \mu(t, \theta) + \int_0^t \partial_\theta g(t-u, \theta) c(u, \theta_n) du}{\mu(t, \theta) + \int_0^t g(t-u, \theta) c(u, \theta_n) du} c(t, \theta_n) dt \\ &\quad - \int_0^1 \left(\partial_\theta \mu(t, \theta) + \int_0^t \partial_\theta g(t-u, \theta) c(u, \theta_n) du \right) dt \end{aligned}$$

and

$$\begin{aligned} s_0(\theta) &= \int_0^1 \frac{\partial_\theta \mu(t, \theta) + \int_0^t \partial_\theta g(t-u, \theta) c(u, \theta_0) du}{\mu(t, \theta) + \int_0^t g(t-u, \theta) c(u, \theta_0) du} c(t, \theta_0) dt \\ &\quad - \int_0^1 \left(\partial_\theta \mu(t, \theta) + \int_0^t \partial_\theta g(t-u, \theta) c(u, \theta_0) du \right) dt. \end{aligned}$$

Recalling that $S_n(\hat{\theta}_n) = 0$ according to (3.10), using the aforementioned Theorem 5.9 boils down to showing the following result.

Lemma 3.5.5. *With s_0 defined as above and S_n as in Section 3.2, we have*

- (a) $\inf_{\{\theta: d(\theta, \theta_0) \geq \varepsilon\}} \|s_0(\theta)\| > 0 = s_0(\theta_0)$ for all $\varepsilon > 0$, and
- (b) $\sup_{\theta \in \Theta} \|a_n^{-1} S_n(\theta) - s_0(\theta)\| \xrightarrow{\mathbb{P}} 0$.

3.5.2 Proof of Theorem 3.2.4

As a first step in the proof, we will give a preliminary comment from which several simplifications follow. Some of these are direct, others need more attention and will be treated in several lemmas, whose proofs are presented in the Supplementary Materials.

Suppose that a decomposition of the form

$$\sqrt{a_n}G_n(u) = \gamma_n F_n(u) + H_n(u) \quad (3.11)$$

with $\gamma_n \xrightarrow{\mathbb{P}} 1$ and $\|H_n\| \xrightarrow{\mathbb{P}} 0$ holds. Using $a_n\|G_n\|^2 = \gamma_n^2\|F_n\|^2 + \|H_n\|^2 + 2\gamma_n\langle F_n, H_n \rangle$, as well as $\gamma_n^2 \xrightarrow{\mathbb{P}} 1$, $\|H_n\|^2 \xrightarrow{\mathbb{P}} 0$ and $\langle F_n, H_n \rangle \leq \|F_n\| \|H_n\|$ plus Slutsky's lemma and the continuous mapping theorem, it is obviously enough to prove weak convergence of $\|F_n\|$ towards a limiting distribution with the desired properties in order to deduce the claim for $\sqrt{a_n}\|G_n\|$.

We use (3.11) for two quick simplifications before we need to get more sophisticated. On one hand, Lemma 3.2.3(a) allows to replace

$$\begin{aligned} \sqrt{a_n}G_n(u) &= \sqrt{a_n} \left(L_n(u, \hat{\theta}_n) - L(u) \right) \\ &= \frac{\sqrt{a_n}}{N_n(1)} \sum_{i \geq 1} \left(k_n(u, \hat{\theta}_n, t_{i-1}, t_i) - L(u) \right) 1_{\{t_i \leq 1\}} \end{aligned}$$

with $(\sqrt{a_n}/\kappa_n) \sum_{i \geq 1} \left(k_n(u, \hat{\theta}_n, t_{i-1}, t_i) - L(u) \right) 1_{\{t_i \leq 1\}}$. Second, using the uniform boundedness of g_n and L as well as integrability of β and $a_n \rightarrow \infty$ we can equivalently discuss

$$\frac{\sqrt{a_n}}{\kappa_n} \sum_{i \geq 1} \left(k_n(u, \hat{\theta}_n, t_{i-1}, t_i) - L(u) \right) 1_{\{t_{i-1} \leq 1\}} \quad (3.12)$$

instead, which later allows for a usage of martingale methods.

We will now state several decompositions of the random function in (3.12), and to keep the notation readable we will provide these in the case where Θ is one-dimensional. The extension to an arbitrary dimension d bears no additional difficulty. We first write

$$\begin{aligned} &k_n(u, \hat{\theta}_n, t_{i-1}, t_i) - L(u) \\ &= \left(k_n(u, \hat{\theta}_n, t_{i-1}, t_i) - k_n(u, \theta_n, t_{i-1}, t_i) \right) + \left(k_n(u, \theta_n, t_{i-1}, t_i) - L(u) \right), \end{aligned} \quad (3.13)$$

where the first summand represents the bias due to the estimation of θ_n while the second one can essentially be interpreted as the usual randomness of having to estimate a Laplace transform from i.i.d. observations. To provide an intuition for the latter interpretation, setting $\mathcal{F}_t = \mathcal{F}_t^n = \sigma(N_n(s) \mid s \leq t)$ we have that the conditional distribution of

$\int_{t_{i-1}}^{t_i} a_n \mu_n(t, \theta_n) dt = \Lambda_n(t_i, \theta_n) - \Lambda_n(t_{i-1}, \theta_n)$ given $\mathcal{F}_{t_{i-1}}$ is the standard expo-

nential.

We will now provide a series of simplifications for the first summand in (3.13) which we can decompose as

$$\begin{aligned}
k_n(u, \hat{\theta}_n, t_{i-1}, t_i) - k_n(u, \theta_n, t_{i-1}, t_i) &= \int_{\theta_n}^{\hat{\theta}_n} q_n(u, r, t_{i-1}, t_i) dr \\
&= (\hat{\theta}_n - \theta_n) q_n(u, \theta_n, t_{i-1}, t_i) + \int_{\theta_n}^{\hat{\theta}_n} \int_{\theta_n}^r \tilde{q}_n(u, z, t_{i-1}, t_i) dz dr \\
&= (\hat{\theta}_n - \theta_n) \mathbb{E}(q_n(u, \theta_n, t_{i-1}, t_i) | \mathcal{F}_{t_{i-1}}) \\
&\quad + (\hat{\theta}_n - \theta_n) \left\{ q_n(u, \theta_n, t_{i-1}, t_i) - \mathbb{E}(q_n(u, \theta_n, t_{i-1}, t_i) | \mathcal{F}_{t_{i-1}}) \right\} \\
&\quad + \int_{\theta_n}^{\hat{\theta}_n} \int_{\theta_n}^r \tilde{q}_n(u, z, t_{i-1}, t_i) dz dr
\end{aligned} \tag{3.14}$$

where we have set

$$q_n(u, \theta, r, s) = \frac{\partial}{\partial \theta} k_n(u, \theta, r, s) \quad \text{and} \quad \tilde{q}_n(u, \theta, r, s) = \frac{\partial^2}{\partial \theta^2} k_n(u, \theta, r, s).$$

Using (3.11), the next lemma proves that the latter two terms in (3.14) do not contribute in the asymptotics. Its proof, as well for several other results, will be given in the Supplementary Materials.

Lemma 3.5.6. *Let*

$$\begin{aligned}
\overline{G}_n(u) &= \frac{\sqrt{a_n}}{\kappa_n} (\hat{\theta}_n - \theta_n) \sum_{i \geq 1} \left\{ q_n(u, \theta_n, t_{i-1}, t_i) - \mathbb{E}(q_n(u, \theta_n, t_{i-1}, t_i) | \mathcal{F}_{t_{i-1}}) \right\} 1_{\{t_{i-1} \leq 1\}} \\
&\quad + \frac{\sqrt{a_n}}{\kappa_n} \sum_{i \geq 1} \int_{\theta_n}^{\hat{\theta}_n} \int_{\theta_n}^r \tilde{q}_n(u, z, t_{i-1}, t_i) dz dr 1_{\{t_{i-1} \leq 1\}} \\
&=: \sqrt{a_n} (\hat{\theta}_n - \theta_n) \overline{G}_n^{(1)}(u) + \overline{G}_n^{(2)}(u).
\end{aligned}$$

Then under Condition 3.2.1, $\|\overline{G}_n\|^2 \xrightarrow{\mathbb{P}} 0$.

Following (3.12), (3.13) and Lemma 3.5.6 we thus only have to establish the asymptotics associated with the random function

$$\begin{aligned}
&\frac{\sqrt{a_n}}{\kappa_n} \sum_{i \geq 1} \left\{ (\hat{\theta}_n - \theta_n) \mathbb{E}(q_n(u, \theta_n, t_{i-1}, t_i) | \mathcal{F}_{t_{i-1}}) \right. \\
&\quad \left. + (k_n(u, \theta_n, t_{i-1}, t_i) - L(u)) \right\} 1_{\{t_{i-1} \leq 1\}}.
\end{aligned} \tag{3.15}$$

We provide two further auxiliary results regarding the first summand above.

Lemma 3.5.7. *Set*

$$h_n(u, \theta_n, t_{i-1}) = \mathbb{E} \left(q_n(u, \theta_n, t_{i-1}, t_i) \middle| \mathcal{F}_{t_{i-1}} \right) \quad \text{and}$$

$$h(u, \theta_0, t) = -\frac{u}{(u+1)^2} \frac{\frac{\partial}{\partial \theta} \mu(t, \theta_0)}{C(1, \theta_0)}$$

as well as

$$\begin{aligned} \widehat{G}_n(u) &= a_n^{1/2} \left(\hat{\theta}_n - \theta_n \right) \left(\frac{1}{\kappa_n} \sum_{i \geq 1} h_n(u, \theta_n, t_{i-1}) 1_{\{t_{i-1} \leq 1\}} - \int_0^1 h(u, \theta_0, t) dt \right) \\ &=: a_n^{1/2} \left(\hat{\theta}_n - \theta_n \right) \widehat{G}_n^{(1)}(u). \end{aligned}$$

Then under Condition 3.2.1, $\|\widehat{G}_n\|^2 \xrightarrow{\mathbb{P}} 0$.

For the other result we utilize the representation

$$0 = a_n^{-1/2} S_n(\hat{\theta}_n) = a_n^{-1/2} S_n(\theta_n) + a_n^{-1} \frac{\partial}{\partial \theta} S_n(\tilde{\theta}_n) a_n^{1/2} \left(\hat{\theta}_n - \theta_n \right)$$

which was introduced prior the statement of Lemma 3.2.3. Using part (c) of that lemma, we can, up to a null set, write

$$a_n^{1/2} \left(\hat{\theta}_n - \theta_n \right) = \frac{a_n^{-1/2} S_n(\theta_n)}{-a_n^{-1} \frac{\partial}{\partial \theta} S_n(\tilde{\theta}_n)}.$$

According to (3.11), Lemma 3.2.3(c), Lemma 3.5.7 and the previous simplifications leading to (3.15) it remains to establish weak convergence of $\|\tilde{G}_n\|$ with

$$\begin{aligned} \tilde{G}_n(u) &= a_n^{-1/2} \left(\frac{S_n(\theta_n)}{\mathcal{I}(\theta_0)} \int_0^1 h(u, \theta_0, t) dt \right. \\ &\quad \left. + \frac{1}{C(1, \theta_0)} \sum_{i \geq 1} (k_n(u, \theta_n, t_{i-1}, t_i) - L(u)) 1_{\{t_{i-1} \leq 1\}} \right). \end{aligned} \quad (3.16)$$

In fact, we will only prove that the \mathcal{H} -valued random variable $\tilde{G}_n(\cdot)$ converges weakly to an \mathcal{H} -valued Gaussian limiting variable $G_{\theta_0}(\cdot)$, as the result then follows from an application of the continuous mapping theorem. For the proof of the aforementioned weak convergence in a Hilbert space we will rely in particular on Theorem 1.8.4 in van der Vaart and Wellner (1996) which contains two sufficient conditions.

The first condition which needs to be checked is asymptotic finite-dimensionality. Denoting an orthonormal basis of \mathcal{H} by $\{e_j \mid j \in J\}$ this amounts to showing that

for every $\varepsilon, \delta > 0$ there exists a finite set $I \subset J$ such that

$$\limsup_{n \rightarrow \infty} \mathbb{P} \left(\sum_{j \notin I} \langle \tilde{G}_n, e_j \rangle^2 > \delta \right) < \varepsilon.$$

Clearly it is sufficient to prove this property for the two summands in (3.16) separately. For the first summand it is relatively simple. First, utilizing Lemma 3.2.3(c) and (3.11) we may equivalently discuss $a_n^{1/2} (\hat{\theta}_n - \theta_n) \int_0^1 h(u, \theta_0, t) dt$.

Now, Lemma 3.2.3(b) implies tightness of the sequence $\sqrt{a_n} (\hat{\theta}_n - \theta_n)$, i.e. the existence of $A > 0$ such that $\limsup_{n \rightarrow \infty} \mathbb{P} \left(\left| \sqrt{a_n} (\hat{\theta}_n - \theta_n) \right| > A \right) \leq \varepsilon/2$. Hence only the existence of I such that

$$\mathbb{P} \left(\sum_{j \notin I} \left\langle \int_0^1 h(u, \theta_0, t) dt, e_j \right\rangle^2 > \frac{\delta}{A^2} \right) \leq \frac{\varepsilon}{2}$$

needs to be shown, and this is an easy consequence of Bessel's inequality since Condition 3.2.1(c) implies boundedness of $\| \int_0^1 h(u, \theta_0, t) dt \|^2$.

The discussion of the other summand in (3.16) is more subtle. Note first that $\mathbb{E} (k_n(u, \theta_n, t_{i-1}, t_i) - L(u) | \mathcal{F}_{t_{i-1}}) = 0$ holds for every i , utilizing that the $\mathcal{F}_{t_{i-1}}$ -conditional distribution of $k_n(u, \theta_n, t_{i-1}, t_i)$ equals the one of $\exp(-uX)$ for $X \sim \exp(1)$ and is independent of $\mathcal{F}_{t_{i-1}}$. Hence, by Fubini's theorem we obtain

$$\begin{aligned} & \mathbb{E} (\langle k_n(u, \theta_n, t_{i-1}, t_i) - L(\cdot), e_j \rangle | \mathcal{F}_{t_{i-1}}) \\ &= \int_0^\infty \mathbb{E} (k_n(u, \theta_n, t_{i-1}, t_i) - L(u) | \mathcal{F}_{t_{i-1}}) e_j(u) \beta(u) du = 0, \end{aligned} \tag{3.17}$$

and for any choice of $i_1 \neq i_2$ we thus have

$$\mathbb{E} (\langle k_n(\cdot, \theta_n, t_{i_1-1}, t_{i_1}) - L(\cdot), e_j \rangle 1_{\{t_{i_1-1} \leq 1\}} \langle k_n(\cdot, \theta_n, t_{i_2-1}, t_{i_2}) - L(\cdot), e_j \rangle 1_{\{t_{i_2-1} \leq 1\}}) = 0$$

by successive conditioning. To summarize,

$$\begin{aligned}
& \mathbb{E} \left(\left\langle \frac{a_n^{-1/2}}{C(1, \theta_0)} \sum_{i \geq 1} (k_n(u, \theta_n, t_{i-1}, t_i) - L(u)) 1_{\{t_{i-1} \leq 1\}}, e_j \right\rangle^2 \right) \\
&= \frac{a_n^{-1}}{C^2(1, \theta_0)} \sum_{i \geq 1} \mathbb{E} (\langle k_n(u, \theta_n, t_{i-1}, t_i) - L(u), e_j \rangle^2 1_{\{t_{i-1} \leq 1\}}) \\
&= \frac{a_n^{-1}}{C^2(1, \theta_0)} \sum_{i \geq 1} \mathbb{E} (\mathbb{E} (\langle k_n(u, \theta_n, t_{i-1}, t_i) - L(u), e_j \rangle^2 | \mathcal{F}_{t_{i-1}}) 1_{\{t_{i-1} \leq 1\}}) \\
&= \frac{a_n^{-1}}{C^2(1, \theta_0)} \mathbb{E} (\langle \exp(-uX) - L(u), e_j(u) \rangle^2) \mathbb{E}(N_n(1) + 1) \\
&\leq K \mathbb{E} (\langle \exp(-uX) - L(u), e_j(u) \rangle^2)
\end{aligned}$$

where we have used Lemma 3.2.3(a) and Condition 3.2.1(c) in the last step. The claim then follows again from Bessel's inequality, this time in connection with dominated convergence and Markov's inequality, utilizing

$$\sum_{j \in J} \mathbb{E} (\langle \exp(-uX) - L(u), e_j(u) \rangle^2) \leq \mathbb{E} (\|\exp(-uX) - L(u)\|^2) < \infty.$$

The second condition of Theorem 1.8.4 in van der Vaart and Wellner (1996) regards weak convergence of

$$\begin{aligned}
\langle \tilde{G}_n, f \rangle &= \frac{a_n^{-1/2} S_n(\theta_n)}{\mathcal{I}(\theta_0)} \left\langle \int_0^1 h(u, \theta_0, t) dt, f(u) \right\rangle \\
&\quad + \frac{a_n^{-1/2}}{C(1, \theta_0)} \sum_{i \geq 1} \langle k_n(u, \theta_n, t_{i-1}, t_i) - L(u), f(u) \rangle 1_{\{t_{i-1} \leq 1\}}.
\end{aligned} \tag{3.18}$$

towards $\langle G_{\theta_0}, f \rangle$ for each $f \in \mathcal{H}$. Here, G_{θ_0} is an \mathcal{H} -valued Gaussian random variable. Precisely, we will show the aforementioned weak convergence with $\langle G_{\theta_0}, f \rangle \sim \mathcal{N}(0, \sigma^2(f))$ for $f \in \mathcal{H}$, which is enough to deduce Gaussianity of G_{θ_0} and determines its distribution uniquely. Here,

$$\begin{aligned}
\sigma^2(f) &= \int_0^1 \left(\left(\frac{\langle \int_0^1 h(u, \theta_0, t) dt, f(u) \rangle}{\mathcal{I}(\theta_0)} \right)^2 \frac{(\frac{\partial}{\partial \theta} \mu(s, \theta_0))^2}{\mu(s, \theta_0)} \right. \\
&\quad \left. + 2 \frac{\langle \int_0^1 h(u, \theta_0, t) dt, f(u) \rangle}{\mathcal{I}(\theta_0) C(1, \theta_0)} \Phi(f) \frac{\partial}{\partial \theta} \mu(s, \theta_0) + \frac{\Delta(f)}{C(1, \theta_0)^2} \mu(s, \theta_0) \right) ds
\end{aligned}$$

with $\Phi(f) = \int_0^\infty \frac{u}{(1+u)^2} f(u) \beta(u) du$ and

$$\Delta(f) = \int_0^\infty \int_0^\infty \left(\frac{1}{1+u+v} - \frac{1}{(1+u)(1+v)} \right) \beta(u) f(u) \beta(v) f(v) dudv.$$

Hence, let $f \in \mathcal{H}$ be fixed from now on.

For the proof of the weak convergence stated above we will rely on a martingale central limit theorem provided as Theorem 2.2.13 in Jean Jacod (2004) for which we need some preparation. Loosely speaking, the problem is that both summands on the right-hand side of (3.18) can be regarded as end points of martingales but with respect to different filtrations (the first one with respect to \mathcal{F}_t for every $t \in [0, 1]$, the second one with respect to $\mathcal{F}_{t_{i-1}}$ for every i). Hence we are looking for an approximation of $\langle G_{\theta_0}, f \rangle$ by an end point of a martingale with respect to the same filtration. For this, we use a “big blocks, small blocks”-strategy. Let $p \in \mathbb{N}$ and $0 < \varrho < 1/2$ be fixed, and set $\ell_n = \lfloor a_n^\varrho \rfloor$, as well as $c_{n,p}(j) = j(p+1)\ell_n$ and $d_{n,p}(j) = j(p+1)\ell_n + p\ell_n$, and recall that one way to prove the weak convergence $Y_n \xrightarrow{\mathcal{L}} Z$ (for generic random variables) is to show

$$Z_{n,p} \xrightarrow{\mathcal{L}} Z_p \text{ as } n \rightarrow \infty, \text{ for any fixed } p \in \mathbb{N}, \quad (3.19)$$

$$Z_p \xrightarrow{\mathcal{L}} Z \text{ as } p \rightarrow \infty, \quad (3.20)$$

$$\lim_{p \rightarrow \infty} \limsup_{n \rightarrow \infty} \mathbb{P}(|Y_n - Z_{n,p}| \geq \eta) = 0, \text{ for any } \eta > 0, \quad (3.21)$$

for auxiliary random variables $Z_{n,p}$ and Z_p . We will begin with a version of (3.21) in our setting, for which we recall the definition of $U_n(t, \theta)$ in (3.8).

Lemma 3.5.8. *Let*

$$G_{n,p}(f) = \sqrt{\frac{(p+1)\ell_n}{a_n}} \sum_{j=0}^{\lfloor \frac{a_n}{(p+1)\ell_n} \rfloor - 1} \left(\frac{\langle \int_0^1 h(u, \theta_0, t) dt, f(u) \rangle}{\mathcal{I}(\theta_0)} \xi_{p,j}^n + \frac{1}{C(1, \theta_0)} \zeta_{p,j}^n(f) \right)$$

with

$$\begin{aligned} \xi_{p,j}^n &= \frac{1}{\sqrt{(p+1)\ell_n}} \sum_{i \geq 1} \left(U_n(t_{i-1}, \theta_n) 1_{\{\frac{c_{n,p}(j)}{a_n} < t_{i-1} \leq \frac{d_{n,p}(j)}{a_n}\}} \right. \\ &\quad \left. - \mathbb{E} \left(U_n(t_{i-1}, \theta_n) 1_{\{\frac{c_{n,p}(j)}{a_n} < t_{i-1} \leq \frac{d_{n,p}(j)}{a_n}\}} \middle| \mathcal{F}_{\frac{c_{n,p}(j)}{a_n}} \right) \right) \end{aligned}$$

and

$$\begin{aligned} \zeta_{p,j}^n(f) &= \frac{1}{\sqrt{(p+1)\ell_n}} \times \\ &\sum_{i \geq 1} \left(\langle k_n(u, \theta_n, t_{i-1}, t_i) - L(u), f(u) \rangle 1_{\{\frac{c_{n,p}(j)}{a_n} < t_{i-1} \leq \frac{d_{n,p}(j)}{a_n}, t_i \leq \frac{c_{n,p}(j+1)}{a_n}\}} \right. \\ &\quad \left. - \mathbb{E} \left(\langle k_n(u, \theta_n, t_{i-1}, t_i) - L(u), f(u) \rangle 1_{\{\frac{c_{n,p}(j)}{a_n} < t_{i-1} \leq \frac{d_{n,p}(j)}{a_n}, t_i \leq \frac{c_{n,p}(j+1)}{a_n}\}} \middle| \mathcal{F}_{\frac{c_{n,p}(j)}{a_n}} \right) \right) \end{aligned}$$

Then, for any $\eta > 0$,

$$\lim_{p \rightarrow \infty} \limsup_{n \rightarrow \infty} \mathbb{P} \left(\left| \langle \tilde{G}_n, f \rangle - G_{n,p}(f) \right| \geq \eta \right) = 0.$$

By definition, $G_{n,p}(f)$ for each fixed p is the end point of a martingale with respect to the filtration associated with $\mathcal{F}_{\frac{c_{n,p}(j)}{a_n}}$ for $j = 0, 1, \dots$. Note that each $\zeta_{p,j}^n(f)$ is measurable with respect to $\mathcal{F}_{\frac{c_{n,p}(j+1)}{a_n}}$, for which the additional condition of $t_i \leq \frac{c_{n,p}(j+1)}{a_n}$ is needed. However, as seen from (7.30) in the Supplementary Materials, adding this condition does not alter the overall asymptotic behaviour.

To finish the proof of Theorem 3.2.4 we need to prove (3.19) and (3.20) for $G_{n,p}(f)$. In fact, we will only prove the analogue of (3.19) in the following result as it is trivial to deduce (3.20) afterwards.

Theorem 3.5.9. *Under Condition 3.2.1, and for any fixed f and p , we have $G_{n,p}(f) \xrightarrow{\mathcal{L}} \mathcal{N} \left(0, \frac{p}{p+1} \sigma^2(f) \right)$.*

For the omitted proofs in this section, namely, the proofs from Lemmas 3.5.2, 3.5.5, 3.5.6, 3.5.7 and 3.5.8, and Theorem 3.5.9, refer to Section 3.6 below.

3.6 Omitted proofs

In this appendix the proofs omitted during Section 3.5 are presented. K will always refer to an unspecified positive constant, possibly changing throughout the proofs.

3.6.1 Proof of Lemma 3.5.1

By definition, $c(t, \theta)$ satisfies the equation

$$c(t, \theta) = \mu(t, \theta) + \int_0^t g(t-u, \theta) c(u, \theta) du \quad (3.22)$$

and is hence continuous as a function in t . Then

$$c(t, \theta) \leq K + K \int_0^t c(u, \theta) du \leq K(1 + \exp(K))$$

by the uniform boundedness of μ and g and Gronwall's lemma.

3.6.2 Proof of Lemma 3.5.2

Using (3.22), we obtain

$$\begin{aligned} |c(t, \theta_0) - c(t, \theta_n)| &\leq |\mu(t, \theta_0) - \mu(t, \theta_n)| \\ &\quad + \left| \int_0^t (g(t-u, \theta_0) - g(t-u, \theta_n)) c(t, \theta_n) du \right| \\ &\quad + \left| \int_0^t g(t-u, \theta_0) (c(t, \theta_0) - c(t, \theta_n)) du \right|. \end{aligned}$$

Recall that μ and g are continuously differentiable with uniformly bounded derivatives and, by Lemma 3.5.1, $c(t, \theta)$ is uniformly bounded, therefore,

$$\sup_{t \in [0,1]} |\mu(t, \theta_0) - \mu(t, \theta_n)| + \left| \int_0^t (g(t-u, \theta_0) - g(t-u, \theta_n)) c(t, \theta_n) du \right| \leq K(\theta_n - \theta_0)$$

Again from Gronwall's lemma we can conclude

$$|c(t, \theta_0) - c(t, \theta_n)| \leq K(\theta_n - \theta_0) + K \int_0^t |c(t, \theta_0) - c(t, \theta_n)| du \leq K(\theta_n - \theta_0)$$

for all $t \in [0, 1]$, from which the claim follows.

3.6.3 Proof of Lemma 3.5.5

Item (a) can be proved exactly as in Chen and Hall (2013).

For (b), the proof has two steps. First, we will show $\sup_{\theta \in \Theta} \|s_n(\theta) - s_0(\theta)\| \rightarrow 0$, for which we write

$$\begin{aligned} \|s_n(\theta) - s_0(\theta)\| &\leq \int_0^1 \int_0^t \|\partial_\theta g(t-u, \theta)\| |c(u, \theta_n) - c(u, \theta_0)| du dt \\ &\quad + \int_0^1 \left\| \frac{\partial_\theta \mu(t, \theta) + \int_0^t \partial_\theta g(t-u, \theta) c(u, \theta_n) du}{\mu(t, \theta) + \int_0^t g(t-u, \theta) c(u, \theta_n) du} c(t, \theta_n) \right. \\ &\quad \left. - \frac{\partial_\theta \mu(t, \theta) + \int_0^t \partial_\theta g(t-u, \theta) c(u, \theta_0) du}{\mu(t, \theta) + \int_0^t g(t-u, \theta) c(u, \theta_0) du} c(t, \theta_0) \right\| dt. \end{aligned} \tag{3.23}$$

The first term on the right hand side is dealt with using Lemma 3.5.2 and uniform boundedness of $\partial_\theta g$, while the second term is split up into

$$\begin{aligned} & \int_0^1 \left\| \frac{\partial_\theta \mu(t, \theta) + \int_0^t \partial_\theta g(t-u, \theta) c(u, \theta_n) du}{\mu(t, \theta) + \int_0^t g(t-u, \theta) c(u, \theta_n) du} \right\| \\ & \quad - \left\| \frac{\partial_\theta \mu(t, \theta) + \int_0^t \partial_\theta g(t-u, \theta) c(u, \theta_0) du}{\mu(t, \theta) + \int_0^t g(t-u, \theta) c(u, \theta_0) du} \right\| c(t, \theta_n) dt \\ & + \int_0^1 \left\| \frac{\partial_\theta \mu(t, \theta) + \int_0^t \partial_\theta g(t-u, \theta) c(u, \theta_0) du}{\mu(t, \theta) + \int_0^t g(t-u, \theta) c(u, \theta_0) du} \right\| |c(t, \theta_n) - c(t, \theta_0)| dt. \end{aligned}$$

To bound the first summand we use Corollary 3.5.3 as well as the uniform boundedness from below of μ in order to deduce that the difference of the fractions converges to zero uniformly in $\theta \in \Theta$. Uniform convergence to zero of the entire term then follows from uniform boundedness of c . The second summand is treated similarly to the first term on the right hand side of (3.23).

To finish the proof of (ii) we have to show $\sup_{\theta \in \Theta} \|a_n^{-1} S_n(\theta) - s_n(\theta)\| \xrightarrow{\mathbb{P}} 0$. We will start with proving the convergence for a fixed $\theta \in \Theta$. Clearly,

$$\begin{aligned} & \|a_n^{-1} S_n(\theta) - s_n(\theta)\| \\ & \leq \left\| \int_0^1 \frac{\partial_\theta \mu(t, \theta) + \int_0^t \partial_\theta g(t-u, \theta) da_n^{-1} N_n(u)}{\mu(t, \theta) + \int_0^t g(t-u, \theta) da_n^{-1} N_n(u)} da_n^{-1} N_n(t) \right. \\ & \quad \left. - \int_0^1 \frac{\partial_\theta \mu(t, \theta) + \int_0^t \partial_\theta g(t-u, \theta) c(u, \theta_n) du}{\mu(t, \theta) + \int_0^t g(t-u, \theta) c(u, \theta_n) du} c(t, \theta_n) dt \right\| \\ & + \int_0^1 \left\| \int_0^t \partial_\theta g(t-u, \theta) c(u, \theta_n) du - \int_0^t \partial_\theta g(t-u, \theta) da_n^{-1} N_n(u) \right\| dt. \end{aligned}$$

All summands converge to zero in view of a repeated application of Corollary 3.5.4. To prove that this convergence is uniform we can follow the same steps as in Chen and Hall (2013). The only difference is that we additionally need to show that for every $\varepsilon > 0$ there exists $\delta > 0$ such that $\|\theta_1 - \theta_2\| < \delta$ implies $\|s_n(\theta_1) - s_n(\theta_2)\| < \varepsilon$. This property, however, follows easily from $\sup_{\theta \in \Theta} \|s_n(\theta) - s_0(\theta)\| \rightarrow 0$ and the fact that such a claim already holds for s_0 .

To finish the proof of Lemma 3.2.3 we recall (3.10). It is clear that Lemma 3.2.3(b) follows once $a_n^{-1/2} S_n(\theta_n) \xrightarrow{\mathcal{L}} N(0, \mathcal{I}(\theta_0))$ and Lemma 3.2.3(c) have been established. For the latter, note that $\sup_{\theta \in \Theta} \|a_n^{-1} \partial_\theta S_n(\theta) - \partial_\theta s_0(\theta)\| \xrightarrow{\mathbb{P}} 0$ can be established in the same way as (ii) above. $\partial_\theta s_0(\theta_0) = -\mathcal{I}(\theta_0)$ and $\tilde{\theta}_n \rightarrow \theta_0$ together with continuity of $\partial_\theta s_0$ then give the claim. Finally, the other claim follows as in

Theorem 2 of Chen and Hall (2013), replacing θ_0 by θ_n up until the definition of $\langle \tilde{M} \rangle_n(t)$. Then $\tilde{M}_n(t)$ converges to $v(t)$ without changing the definition of the latter.

3.6.4 Proof of Lemma 3.5.6

Regarding the first summand, note that the sequence $\sqrt{a_n}(\hat{\theta}_n - \theta_n)$ is tight according to Lemma 3.2.3(b). Hence it is sufficient to show

$$\mathbb{E} \left(\left\| \overline{G}_n^{(1)} \right\|^2 \right) = \int_0^\infty \mathbb{E} \left(\left(G_n^{(1)}(u) \right)^2 \right) \beta(u) du = o(1),$$

where we have used Fubini's theorem. By construction,

$$\begin{aligned} \mathbb{E} \left(\left(G_n^{(1)}(u) \right)^2 \right) &= \\ &= \frac{1}{\kappa_n^2} \sum_{i \geq 1} \mathbb{E} \left(\left(q_n(u, \theta_n, t_{i-1}, t_i) - \mathbb{E} \left(q_n(u, \theta_n, t_{i-1}, t_i) \mid \mathcal{F}_{t_{i-1}} \right) \right)^2 1_{\{t_{i-1} \leq 1\}} \right). \end{aligned}$$

To finish the proof for the first summand we will show uniform boundedness of $q_n(u, \theta_n, t_{i-1}, t_i)$, as then

$$\mathbb{E} \left(\left(G_n^{(1)}(u) \right)^2 \right) \leq K \frac{1}{\kappa_n^2} \sum_{i \geq 1} \mathbb{E} (1_{\{t_{i-1} \leq 1\}}) \leq K \frac{\mathbb{E}(N_n(1) + 1)}{\kappa_n^2} = o(1)$$

(use Lemma 3.2.3(a) and integrability of β) concludes. To prove the aforementioned uniform boundedness we write

$$|q_n(u, \theta, r, s)| \leq \exp \left(-u \int_r^s a_n \mu(t, \theta) dt \right) u a_n \int_r^s \left| \frac{\partial}{\partial \theta} \mu(t, \theta) \right| dt,$$

where we have used Condition 3.2.1(c) to justify the exchange of integral and derivative. The same assumption allows to bound the right hand side above by

$$|q_n(u, \theta, r, s)| \leq K \exp \left(-u \int_r^s a_n \mu(t, \theta) dt \right) u a_n \int_r^s \mu(t, \theta) dt,$$

using the fact that $\mu(t, \theta)$ is uniformly bounded from below while $|\frac{\partial}{\partial \theta} \mu(t, \theta)|$ is uniformly bounded from above. $x \exp(-x) \leq 1$ for $x \geq 0$ finishes the proof for the first summand.

For the second summand, note that a similar argument in combination with the boundedness of $x^2 \exp(-x)$ for $x \geq 0$ yields $|\tilde{q}_n(u, \theta, r, s)| \leq K$. Hence,

$|G_n^{(2)}(u)| \leq K\sqrt{a_n} \left| \hat{\theta}_n - \theta_n \right|^2 (N_n(1) + 1) / \kappa_n$, and Slutsky's lemma in combination with Lemma 3.2.3(a) and (b) proves that the right hand side is $o_{\mathbb{P}}(1)$. Since the same upper bound (up to a possibly different constant) holds for $\|G_n^{(2)}\|$ as well, the proof is complete. \square

3.6.5 Proof of Lemma 3.5.7

Let us start with some remarks regarding integrals with respect to inhomogeneous Poisson processes. For any \mathcal{F} -stopping time R , any $s > 0$, and any bounded measurable function $\varphi \geq 0$ we have

$$\begin{aligned} \mathbb{E} \left(\sum_{i \geq 1} 1_{\{R < t_i \leq R+s\}} \varphi(t_i, \theta_n) \middle| \mathcal{F}_R \right) &= \mathbb{E} \left(\int_R^{R+s} \varphi(t, \theta_n) dN_n(t) \middle| \mathcal{F}_R \right) \\ &= \mathbb{E} \left(a_n \int_R^{R+s} \varphi(t, \theta_n) \mu(t, \theta_n) dt \middle| \mathcal{F}_R \right) \end{aligned}$$

as well as

$$\text{Var} \left(\int_R^{R+s} \varphi(t, \theta_n) dN_n(t) \middle| \mathcal{F}_R \right) = \mathbb{E} \left(a_n \int_R^{R+s} \varphi^2(t, \theta_n) \mu(t, \theta_n) dt \middle| \mathcal{F}_R \right).$$

We now write $\widehat{G}_n^{(1)}(u) = \widehat{G}_n^{(2)}(u) + \widehat{G}_n^{(3)}(u) + \widehat{G}_n^{(4)}(u)$ with

$$\begin{aligned} \widehat{G}_n^{(2)}(u) &= \frac{1}{\kappa_n} \left(\sum_{i \geq 1} h_n(u, \theta_n, t_{i-1}) 1_{\{t_{i-1} \leq 1\}} - \int_0^1 h_n(u, \theta_n, t) a_n \mu(t, \theta_n) dt \right), \\ \widehat{G}_n^{(3)}(u) &= \int_0^1 \left(\frac{a_n}{\kappa_n} h_n(u, \theta_n, t) \mu(t, \theta_n) - h(u, \theta_n, t) \right) dt, \\ \widehat{G}_n^{(4)}(u) &= \int_0^1 (h(u, \theta_n, t) - h(u, \theta_0, t)) dt. \end{aligned}$$

Obviously, as in the proof of Lemma 3.5.6, it suffices to show $\mathbb{E} \left(\left\| \widehat{G}_n^{(1)} \right\|^2 \right) = o(1)$, and we prove the claim above separately for $\widehat{G}_n^{(2)}$, $\widehat{G}_n^{(3)}$ and $\widehat{G}_n^{(4)}$. The latter is an immediate consequence of Condition 3.2.1(c) and dominated convergence.

For the first one, note that we may write

$$\begin{aligned} \widehat{G}_n^{(2)}(u) &= \frac{1}{\kappa_n} \left(\sum_{i \geq 1} h_n(u, \theta_n, t_{i-1}) 1_{\{t_{i-1} \leq 1\}} - \int_0^1 h_n(u, \theta_n, t) a_n \mu(t, \theta_n) dt \right) \\ &= \frac{1}{\kappa_n} \left(\int_0^1 h_n(u, \theta_n, t) dN_n(t) - \int_0^1 h_n(u, \theta_n, t) a_n \mu(t, \theta_n) dt \right) + o_{\mathbb{P}}(1) \end{aligned}$$

where the error term is due to up to two additional summands according to $1_{\{t_{i-1} \leq 1\}}$ instead of $1_{\{0 < t_i \leq 1\}}$. In particular, this error term is uniformly bounded by definition of h_n and g_n , and it is then easy to obtain

$$\begin{aligned} & \mathbb{E} \left(\left(\widehat{G}_n^{(2)}(u) \right)^2 \right) \\ &= \mathbb{E} \left(\frac{1}{\kappa_n^2} \left(\int_0^1 h_n(u, \theta_n, t) dN_n(t) - \int_0^1 h_n(u, \theta_n, t) a_n \mu(t, \theta_n) dt \right)^2 \right) + o(1) \\ &= \frac{1}{\kappa_n^2} \int_0^1 h_n^2(u, \theta_n, t) a_n \mu(t, \theta_n) dt + o(1) = o(1) \end{aligned}$$

with again uniformly bounded error terms. Dominated convergence concludes.

The most involved part of the proof regards $\widehat{G}_n^{(3)}$, and we begin with deriving a suitable functional form for $h_n(u, \theta_n, t_{i-1})$. On the set where $s > t_{i-1}$, we have

$$\begin{aligned} \mathbb{P}(t_i \geq s | \mathcal{F}_{t_{i-1}}) &= \mathbb{P}(\Lambda(t_i, \theta_n) - \Lambda(t_{i-1}, \theta_n) \geq \Lambda(s, \theta_n) - \Lambda(t_{i-1}, \theta_n) | \mathcal{F}_{t_{i-1}}) \\ &= \exp \left(- \int_{t_{i-1}}^s a_n \mu(r, \theta_n) dr \right), \end{aligned}$$

which gives the conditional density

$$f_{t_{i-1}}(s) = \exp \left(- \int_{t_{i-1}}^s a_n \mu(r, \theta_n) dr \right) a_n \mu(s, \theta_n) 1_{\{s > t_{i-1}\}}. \quad (3.24)$$

As a consequence, we have by definition of $q_n(u, \theta, r, s)$ and using integration by parts as well as a change of variables

$$\begin{aligned} h_n(u, \theta_n, t_{i-1}) &= \int_{t_{i-1}}^\infty \exp \left(-u \int_{t_{i-1}}^s a_n \mu(r, \theta_n) dr \right) \left(-u a_n \int_{t_{i-1}}^s \frac{\partial}{\partial \theta} \mu(r, \theta_n) dr \right) \\ &\quad \exp \left(- \int_{t_{i-1}}^s a_n \mu(r, \theta_n) dr \right) a_n \mu(s, \theta_n) ds \\ &= \int_{t_{i-1}}^\infty \exp \left(-(u+1) \int_{t_{i-1}}^s a_n \mu(r, \theta_n) dr \right) \left(-u a_n \int_{t_{i-1}}^s \frac{\partial}{\partial \theta} \mu(r, \theta_n) dr \right) a_n \mu(s, \theta_n) ds \\ &= -\frac{u}{1+u} \int_0^\infty \exp \left(-(u+1) \int_{t_{i-1}}^{t_{i-1}+s} a_n \mu(r, \theta_n) dr \right) a_n \frac{\partial}{\partial \theta} \mu(t_{i-1} + s, \theta_n) ds. \end{aligned}$$

Again, Condition 3.2.1(c) allows to exchange integrals and derivatives. Using the notation $g_{t,n}(s) = \int_0^s \mu(r+t, \theta_n) dr$ and $f_{t,n}(s) = \frac{\partial}{\partial \theta} \mu(t+s, \theta_n)$, and another change

of variables, we can hence write

$$\begin{aligned}
h_n(u, \theta_n, t) &= -\frac{u}{1+u} \int_0^\infty \exp(-(u+1)a_n g_{t,n}(s)) a_n f_{t,n}(s) ds \\
&= -f_{t,n}(0) \frac{u}{1+u} \int_0^\infty \exp\left(-(u+1)s \frac{g_{t,n}(\frac{s}{a_n}) - g_{t,n}(0)}{\frac{s}{a_n}}\right) ds \\
&\quad - \frac{u}{1+u} \int_0^\infty \exp\left(-(u+1)s \frac{g_{t,n}(\frac{s}{a_n}) - g_{t,n}(0)}{\frac{s}{a_n}}\right) \left(f_{t,n}\left(\frac{s}{a_n}\right) - f_{t,n}(0)\right) ds \\
&=: h_n^{(1)}(u, \theta_n, t) + h_n^{(2)}(u, \theta_n, t).
\end{aligned}$$

Proving $\int_0^\infty \left(\int_0^1 \frac{a_n}{\kappa_n} h_n^{(2)}(u, \theta_n, t) \mu(t, \theta_n) dt \right)^2 \beta(u) du = o(1)$ follows quickly, as Condition 3.2.1(c) grants boundedness of all coefficients as well as

$$\begin{aligned}
&\int_0^\infty \exp\left(-(u+1)s \frac{g_{t,n}(\frac{s}{a_n}) - g_{t,n}(0)}{\frac{s}{a_n}}\right) \left(f_{t,n}\left(\frac{s}{a_n}\right) - f_{t,n}(0)\right) ds \\
&\leq K \int_0^\infty \frac{s}{a_n} \exp(-Ks) ds \leq \frac{K}{a_n}.
\end{aligned}$$

We finally prove

$$\int_0^\infty \left(\int_0^1 \left(\frac{a_n}{\kappa_n} h_n^{(1)}(u, \theta_n, t) \mu(t, \theta_n) - h(u, \theta_n, t) \right) dt \right)^2 \beta(u) du = o(1). \quad (3.25)$$

Note that we can rewrite

$$\begin{aligned}
h(u, \theta_n, t) &= -\frac{u}{u+1} \frac{1}{C(1, \theta_0)} \frac{\partial}{\partial \theta} \mu(t, \theta_n) \frac{1}{(u+1)\mu(t, \theta_n)} \mu(t, \theta_n) \\
&= -\frac{u}{u+1} \frac{a_n}{\kappa_n} f_{t,n}(0) \frac{1}{(u+1)g'_{t,n}(0)} \mu(t, \theta_n),
\end{aligned}$$

utilizing Condition 3.2.1(c). Hence, using dominated convergence three times, (3.25) follows from showing

$$\lim_{n \rightarrow \infty} \left\{ \exp\left(-(u+1)s \frac{g_{t,n}(\frac{s}{a_n}) - g_{t,n}(0)}{\frac{s}{a_n}}\right) - \exp(-(u+1)s g'_{t,n}(0)) \right\} = 0,$$

uniformly in u, t and s . The latter is an easy consequence from Lipschitz continuity of $x \mapsto \exp(-x)$ on $[-K, \infty)$ and Condition 3.2.1(c). \square

3.6.6 Proof of Lemma 3.5.8

Recall the identities given at the beginning of the proof of Lemma 3.5.7. Utilizing

$$\sum_{i \geq 1} U_n(t_{i-1}, \theta_n) 1_{\{R < t_{i-1} \leq R+s\}} = \int_R^{R+s} U_n(t, \theta_n) dN_n(t) \quad (3.26)$$

and the definition of $U_n(t, \theta)$ in (3.8), we can then write

$$S_n(\theta_n) = \int_0^1 U_n(t, \theta_n) dM_n(t, \theta_n) = \sum_{i \geq 1} U_n(t_{i-1}, \theta_n) 1_{\{0 < t_{i-1} \leq 1\}} - a_n \int_0^1 \frac{\partial}{\partial \theta} \mu(t, \theta) dt,$$

and setting

$$\begin{aligned} \bar{\xi}_{p,j}^n &= \frac{1}{\sqrt{(p+1)\ell_n}} \sum_{i \geq 1} \left(U_n(t_{i-1}, \theta_n) 1_{\{\frac{d_{n,p}(j)}{a_n} < t_{i-1} \leq \frac{c_{n,p}(j+1)}{a_n}\}} \right. \\ &\quad \left. - \mathbb{E} \left(U_n(t_{i-1}, \theta_n) 1_{\{\frac{d_{n,p}(j)}{a_n} < t_{i-1} \leq \frac{c_{n,p}(j+1)}{a_n}\}} \middle| \mathcal{F}_{\frac{d_{n,p}(j)}{a_n}} \right) \right) \\ &= \frac{1}{\sqrt{(p+1)\ell_n}} \left(\int_{\frac{d_{n,p}(j)}{a_n}}^{\frac{c_{n,p}(j+1)}{a_n}} U_n(t, \theta_n) dN_n(t) - \mathbb{E} \left(\int_{\frac{d_{n,p}(j)}{a_n}}^{\frac{c_{n,p}(j+1)}{a_n}} U_n(t, \theta_n) dN_n(t) \middle| \mathcal{F}_{\frac{d_{n,p}(j)}{a_n}} \right) \right) \end{aligned} \quad (3.27)$$

we then obtain

$$\begin{aligned} a_n^{-1/2} S_n(\theta_n) &- \sqrt{\frac{(p+1)\ell_n}{a_n}} \sum_{j=0}^{\lfloor \frac{a_n}{(p+1)\ell_n} \rfloor - 1} \bar{\xi}_{p,j}^n \\ &= \sqrt{\frac{(p+1)\ell_n}{a_n}} \sum_{j=0}^{\lfloor \frac{a_n}{(p+1)\ell_n} \rfloor - 1} \bar{\xi}_{p,j}^n + a_n^{-1/2} \left(\int_{\lfloor \frac{a_n}{(p+1)\ell_n} \rfloor \frac{(p+1)\ell_n}{a_n}}^1 U_n(t, \theta_n) dN_n(t) \right. \\ &\quad \left. - \mathbb{E} \left[\int_{\lfloor \frac{a_n}{(p+1)\ell_n} \rfloor \frac{(p+1)\ell_n}{a_n}}^1 U_n(t, \theta_n) dN_n(t) \middle| \mathcal{F}_{\lfloor \frac{a_n}{(p+1)\ell_n} \rfloor \frac{(p+1)\ell_n}{a_n}} \right] \right). \end{aligned}$$

Using the final representation for $\bar{\xi}_{p,j}^n$ above we get

$$\begin{aligned}
& \mathbb{E} \left(\left(\sqrt{\frac{(p+1)\ell_n}{a_n}} \sum_{j=0}^{\lfloor \frac{a_n}{(p+1)\ell_n} \rfloor - 1} \bar{\xi}_{p,j}^n \right)^2 \right) \\
&= \frac{(p+1)\ell_n}{a_n} \sum_{j=0}^{\lfloor \frac{a_n}{(p+1)\ell_n} \rfloor - 1} \text{Var}(\bar{\xi}_{p,j}^n) \\
&= a_n \frac{(p+1)\ell_n}{a_n} \sum_{j=0}^{\lfloor \frac{a_n}{(p+1)\ell_n} \rfloor - 1} \frac{1}{(p+1)\ell_n} \int_{\frac{d_{n,p}(j)}{a_n}}^{\frac{c_{n,p}(j+1)}{a_n}} \frac{\left(\frac{\partial}{\partial \theta} \mu(t, \theta_n) \right)^2}{\mu(t, \theta_n)} dt \leq \frac{K}{p+1}
\end{aligned}$$

where we have applied the martingale structure in the first equality as well as Condition 3.2.1(c) and the definitions of $c_{n,p}(j)$ and $d_{n,p}(j)$ for the final bound. Similarly,

$$\begin{aligned}
& \mathbb{E} \left(\left(a_n^{-1/2} \left(\int_{\lfloor \frac{a_n}{(p+1)\ell_n} \rfloor \frac{(p+1)\ell_n}{a_n}}^1 U_n(t, \theta_n) dN_n(t) \right. \right. \right. \\
& \quad \left. \left. \left. - \mathbb{E} \left(\int_{\lfloor \frac{a_n}{(p+1)\ell_n} \rfloor \frac{(p+1)\ell_n}{a_n}}^1 U_n(t, \theta_n) dN_n(t) \middle| \mathcal{F}_{\lfloor \frac{a_n}{(p+1)\ell_n} \rfloor \frac{(p+1)\ell_n}{a_n}} \right) \right) \right)^2 \right) \\
&= \int_{\lfloor \frac{a_n}{(p+1)\ell_n} \rfloor \frac{(p+1)\ell_n}{a_n}}^1 \frac{\left(\frac{\partial}{\partial \theta} \mu(t, \theta_n) \right)^2}{\mu(t, \theta_n)} dt \leq K \frac{(p+1)\ell_n}{a_n}.
\end{aligned}$$

By definition of ℓ_n is then easy to deduce

$$\lim_{p \rightarrow \infty} \limsup_{n \rightarrow \infty} \mathbb{P} \left(\left| a_n^{-1/2} S_n(\theta_n) - \sqrt{\frac{(p+1)\ell_n}{a_n}} \sum_{j=0}^{\lfloor \frac{a_n}{(p+1)\ell_n} \rfloor - 1} \bar{\xi}_{p,j}^n \right| \geq \eta \right) = 0$$

which (together with the uniform boundedness of the other factors appearing) finishes the first part of the proof.

The second part of the proof is slightly more involved. We need to reproduce most of the arguments given previously on one hand, but we also need to discuss the additional condition of $t_i \leq \frac{c_{n,p}(j+1)}{a_n}$. We will start with the former and, setting

$$\begin{aligned}
\tilde{\zeta}_{p,j}^n(f) &= \frac{1}{\sqrt{(p+1)\ell_n}} \sum_{i \geq 1} \langle k_n(u, \theta_n, t_{i-1}, t_i) - L(u), f(u) \rangle 1_{\left\{ \frac{c_{n,p}(j)}{a_n} < t_{i-1} \leq \frac{d_{n,p}(j)}{a_n} \right\}}, \\
\bar{\zeta}_{p,j}^n(f) &= \frac{1}{\sqrt{(p+1)\ell_n}} \sum_{i \geq 1} \langle k_n(u, \theta_n, t_{i-1}, t_i) - L(u), f(u) \rangle 1_{\left\{ \frac{d_{n,p}(j)}{a_n} < t_{i-1} \leq \frac{c_{n,p}(j+1)}{a_n} \right\}},
\end{aligned}$$

discuss

$$\begin{aligned}
& a_n^{-1/2} \sum_{i \geq 1} \langle k_n(u, \theta_n, t_{i-1}, t_i) - L(u), f(u) \rangle 1_{\{t_{i-1} \leq 1\}} - \sqrt{\frac{(p+1)\ell_n}{a_n}} \sum_{j=0}^{\lfloor \frac{a_n}{(p+1)\ell_n} \rfloor - 1} \tilde{\zeta}_{p,j}^n(f) \\
&= \sqrt{\frac{(p+1)\ell_n}{a_n}} \sum_{j=0}^{\lfloor \frac{a_n}{(p+1)\ell_n} \rfloor - 1} \bar{\zeta}_{p,j}^n(f) \\
&\quad + a_n^{-1/2} \sum_{i \geq 1} \langle k_n(u, \theta_n, t_{i-1}, t_i) - L(u), f(u) \rangle 1_{\{\lfloor \frac{a_n}{(p+1)\ell_n} \rfloor \frac{(p+1)\ell_n}{a_n} < t_{i-1} \leq 1\}}.
\end{aligned}$$

First, applying (3.17) with f in place of e_j gives

$$\mathbb{E} \left(\langle k_n(u, \theta_n, t_{i-1}, t_i) - L(u), f(u) \rangle 1_{\{\frac{c_{n,p}(j)}{a_n} < t_{i-1} \leq \frac{d_{n,p}(j)}{a_n}\}} \middle| \mathcal{F}_{\frac{c_{n,p}(j)}{a_n}} \right) = 0$$

after successive conditioning utilizing

$$\mathbb{E} (1_{\{R \leq S\}} X | \mathcal{F}_R) = \mathbb{E} (1_{\{R \leq S\}} \mathbb{E}(X | \mathcal{F}_S) | \mathcal{F}_R) \quad (3.28)$$

for a generic random variable X and generic stopping times R and S . By uniform boundedness of $\langle k_n(u, \theta_n, t_{i-1}, t_i) - L(u), f(u) \rangle$ for a fixed f we then get

$$\begin{aligned}
& \mathbb{E} \left(\left(\sqrt{\frac{(p+1)\ell_n}{a_n}} \sum_{j=0}^{\lfloor \frac{a_n}{(p+1)\ell_n} \rfloor - 1} \bar{\zeta}_{p,j}^n(f) \right)^2 \right) = \frac{(p+1)\ell_n}{a_n} \sum_{j=0}^{\lfloor \frac{a_n}{(p+1)\ell_n} \rfloor - 1} \text{Var}(\bar{\zeta}_{p,j}^n(f)) \\
& \leq \frac{1}{a_n} \sum_{j=0}^{\lfloor \frac{a_n}{(p+1)\ell_n} \rfloor - 1} \mathbb{E} \left(\left(N \left(\frac{c_{n,p}(j+1)}{a_n} \right) - N \left(\frac{d_{n,p}(j)}{a_n} \right) \right)^2 \right) \\
& \leq \frac{1}{a_n} \sum_{j=0}^{\lfloor \frac{a_n}{(p+1)\ell_n} \rfloor - 1} a_n \frac{K\ell_n}{a_n} \leq \frac{K}{p+1},
\end{aligned}$$

and we also have

$$a_n^{-1/2} \sum_{i \geq 1} \mathbb{E} \left(|\langle k_n(u, \theta_n, t_{i-1}, t_i) - L(u), f(u) \rangle| 1_{\{\lfloor \frac{a_n}{(p+1)\ell_n} \rfloor \frac{(p+1)\ell_n}{a_n} < t_{i-1} \leq 1\}} \right) \leq K \frac{(p+1)\ell_n}{\sqrt{a_n}}$$

which converges to zero as $n \rightarrow \infty$, by definition of ℓ_n . For these terms we can then conclude as in the first step of the proof, ignoring bounded factors again.

Finally, we need to bound

$$\begin{aligned} & \mathbb{E} \left(\left(\sqrt{\frac{(p+1)\ell_n}{a_n}} \sum_{j=0}^{\lfloor \frac{a_n}{(p+1)\ell_n} \rfloor - 1} \left(\tilde{\zeta}_{p,j}^n(f) - \zeta_{p,j}^n(f) \right) \right)^2 \right) \\ &= \frac{(p+1)\ell_n}{a_n} \sum_{j=0}^{\lfloor \frac{a_n}{(p+1)\ell_n} \rfloor - 1} \mathbb{E} \left(\left(\tilde{\zeta}_{p,j}^n(f) - \zeta_{p,j}^n(f) \right)^2 \right), \end{aligned}$$

where we have used the martingale structure for both summands again. Note that, applying (3.17) again,

$$\begin{aligned} \tilde{\zeta}_{p,j}^n(f) - \zeta_{p,j}^n(f) &= \frac{1}{\sqrt{(p+1)\ell_n}} \sum_{i \geq 1} \langle k_n(u, \theta_n, t_{i-1}, t_i) - L(u), f(u) \rangle \times \\ &\quad \left(1_{\left\{ \frac{c_{n,p}(j)}{a_n} < t_{i-1} \leq \frac{d_{n,p}(j)}{a_n}, t_i > \frac{c_{n,p}(j+1)}{a_n} \right\}} - \mathbb{E} \left(1_{\left\{ \frac{c_{n,p}(j)}{a_n} < t_{i-1} \leq \frac{d_{n,p}(j)}{a_n}, t_i > \frac{c_{n,p}(j+1)}{a_n} \right\}} \middle| \mathcal{F}_{\frac{c_{n,p}(j)}{a_n}} \right) \right). \end{aligned}$$

Clearly, for any fixed j the number of indices i satisfying $\frac{c_{n,p}(j)}{a_n} < t_{i-1} \leq \frac{d_{n,p}(j)}{a_n}$ and $t_i > \frac{c_{n,p}(j+1)}{a_n}$ is at most one. Thus, by uniform boundedness again,

$$\mathbb{E} \left(\left(\sqrt{\frac{(p+1)\ell_n}{a_n}} \sum_{j=0}^{\lfloor \frac{a_n}{(p+1)\ell_n} \rfloor - 1} \left(\tilde{\zeta}_{p,j}^n(f) - \zeta_{p,j}^n(f) \right) \right)^2 \right) \leq \frac{K}{(p+1)\ell_n} \quad (3.29)$$

which finishes the proof. \square

3.6.7 Proof of Theorem 3.5.9

According to Theorem 2.2.13 in Jean Jacod (2004) it is enough to prove

$$\sum_{j=0}^{\lfloor \frac{a_n}{(p+1)\ell_n} \rfloor - 1} \left(\frac{(p+1)\ell_n}{a_n} \right)^2 \mathbb{E} \left(\left| \frac{\langle \int_0^1 h(u, \theta_0, t) dt, f(u) \rangle}{\mathcal{I}(\theta_0)} \xi_{p,j}^n + \frac{1}{C(1, \theta_0)} \zeta_{p,j}^n(f) \right|^4 \right) = o(1)$$

as well as convergence of

$$\frac{(p+1)\ell_n}{a_n} \sum_{j=0}^{\lfloor \frac{a_n}{(p+1)\ell_n} \rfloor - 1} \mathbb{E} \left(\left(\frac{\langle \int_0^1 h(u, \theta_0, t) dt, f(u) \rangle}{\mathcal{I}(\theta_0)} \xi_{p,j}^n + \frac{1}{C(1, \theta_0)} \zeta_{p,j}^n(f) \right)^2 \middle| \mathcal{F}_{\frac{c_{n,p}(j)}{a_n}} \right)$$

towards

$$\begin{aligned} & \frac{p}{p+1} \int_0^r \left(\left(\frac{\langle \int_0^1 h(u, \theta_0, t) dt, f(u) \rangle}{\mathcal{I}(\theta_0)} \right)^2 \frac{\left(\frac{\partial}{\partial \theta} \mu(s, \theta_0) \right)^2}{\mu(s, \theta_0)} \right. \\ & \quad \left. + 2 \frac{\langle \int_0^1 h(u, \theta_0, t) dt, f(u) \rangle}{\mathcal{I}(\theta_0) C(1, \theta_0)} \Phi(f) \frac{\partial}{\partial \theta} \mu(s, \theta_0) + \frac{\Delta(f)}{C(1, \theta_0)^2} \mu(s, \theta_0) \right) ds, \end{aligned} \quad (3.30)$$

in probability as $n \rightarrow \infty$, the latter for any $r \in [0, 1]$, and everything for a fixed p and a fixed f . The proof is then finished as (3.30) equals $\frac{p}{p+1} \sigma^2(f)$ for $r = 1$. Regarding the terms involving $\zeta_{p,j}^n(f)$, note that we may replace them by $\tilde{\zeta}_{p,j}^n(f)$ for both claims because the same reasoning that was leading to (3.29) applies here as well.

For the fourth moments, note that we only need to prove uniform boundedness of $\mathbb{E}(|\xi_{p,j}^n|^4)$ and $\mathbb{E}(|\tilde{\zeta}_{p,j}^n(f)|^4)$. For the first one, recall basically from (3.27) that we can write

$$\xi_{p,j}^n = \frac{1}{\sqrt{(p+1)\ell_n}} \left(\int_{\frac{c_{n,p(j)}}{a_n}}^{\frac{d_{n,p(j)}}{a_n}} U_n(t, \theta_n) dN_n(t) - \mathbb{E} \left(\int_{\frac{c_{n,p(j)}}{a_n}}^{\frac{d_{n,p(j)}}{a_n}} U_n(t, \theta_n) dN_n(t) \middle| \mathcal{F}_{\frac{c_{n,p(j)}}{a_n}} \right) \right),$$

and (2.1.37) in Jean Jacod (2004) shows

$$\begin{aligned} & \mathbb{E}(|\xi_{p,j}^n|^4) \\ & \leq K \frac{1}{((p+1)\ell_n)^2} \times \left\{ a_n \int_{\frac{c_{n,p(j)}}{a_n}}^{\frac{d_{n,p(j)}}{a_n}} U_n^4(t, \theta_n) \mu(t, \theta_n) dt + \left(a_n \int_{\frac{c_{n,p(j)}}{a_n}}^{\frac{d_{n,p(j)}}{a_n}} U_n^2(t, \theta_n) \mu(t, \theta_n) dt \right)^2 \right\} \\ & \leq K \left(\frac{p}{(p+1)^2 \ell_n} + \frac{p^2}{(p+1)^2} \right) \leq K. \end{aligned}$$

Utilizing (3.17) we also have

$$\begin{aligned} & \mathbb{E} \left(\left| \tilde{\zeta}_{p,j}^n(f) \right|^4 \right) \\ & \leq K \frac{1}{((p+1)\ell_n)^2} \times \left\{ \sum_{i \geq 1} \mathbb{E} \left(\langle k_n(u, \theta_n, t_{i-1}, t_i) - L(u), f(u) \rangle^4 1_{\left\{ \frac{c_{n,p(j)}}{a_n} < t_{i-1} \leq \frac{d_{n,p(j)}}{a_n} \right\}} \right) \right. \\ & \quad \left. + \left(\sum_{i \geq 1} \mathbb{E} \left(\langle k_n(u, \theta_n, t_{i-1}, t_i) - L(u), f(u) \rangle^2 1_{\left\{ \frac{c_{n,p(j)}}{a_n} < t_{i-1} \leq \frac{d_{n,p(j)}}{a_n} \right\}} \right) \right)^2 \right\}. \end{aligned}$$

By uniform boundedness of $\langle k_n(u, \theta_n, t_{i-1}, t_i) - L(u), f(u) \rangle$ we then obtain

$$\mathbb{E}(|\tilde{\zeta}_{p,j}^n(f)|^4) \leq K \left(\frac{p}{(p+1)^2 \ell_n} + \frac{p^2}{(p+1)^2} \right) \leq K$$

as above.

We will finally discuss the convergence towards (3.30), but we will restrict ourselves to the case $r = 1$ as the proof is completely similar in the general setting. First, recalling the rules established in the beginning of the proof of Lemma 3.5.7,

$$\begin{aligned} \mathbb{E} \left(|\zeta_{p,j}^n|^2 \middle| \mathcal{F}_{\frac{c_{n,p}(j)}{a_n}} \right) &= \frac{1}{(p+1)\ell_n} \text{Var} \left(\int_{\frac{c_{n,p}(j)}{a_n}}^{\frac{d_{n,p}(j)}{a_n}} U_n(s, \theta_n) dN_n(s) \middle| \mathcal{F}_{\frac{c_{n,p}(j)}{a_n}} \right) \\ &= \frac{a_n}{(p+1)\ell_n} \int_{\frac{c_{n,p}(j)}{a_n}}^{\frac{d_{n,p}(j)}{a_n}} U_n^2(s, \theta_n) \mu(s, \theta_n) ds = \frac{a_n}{(p+1)\ell_n} \int_{\frac{c_{n,p}(j)}{a_n}}^{\frac{d_{n,p}(j)}{a_n}} \frac{\left(\frac{\partial}{\partial \theta} \mu(s, \theta_n) \right)^2}{\mu(s, \theta_n)} ds. \end{aligned}$$

Also, using (3.17) and (3.28) again,

$$\begin{aligned} \mathbb{E} \left(|\tilde{\zeta}_{p,j}^n(f)|^2 \middle| \mathcal{F}_{\frac{c_{n,p}(j)}{a_n}} \right) &= \frac{1}{(p+1)\ell_n} \times \\ &\sum_{i \geq 1} \mathbb{E} \left(\mathbb{E} \left(\langle k_n(u, \theta_n, t_{i-1}, t_i) - L(u), f(u) \rangle^2 \middle| \mathcal{F}_{t_{i-1}} \right) 1_{\left\{ \frac{c_{n,p}(j)}{a_n} < t_{i-1} \leq \frac{d_{n,p}(j)}{a_n} \right\}} \middle| \mathcal{F}_{\frac{c_{n,p}(j)}{a_n}} \right), \end{aligned}$$

and we also have

$$\mathbb{E} \left(\langle k_n(u, \theta_n, t_{i-1}, t_i) - L(u), f(u) \rangle^2 \middle| \mathcal{F}_{t_{i-1}} \right) = \mathbb{E} \left(\langle \exp(-uX) - L(u), f(u) \rangle^2 \right)$$

with $X \sim \exp(1)$ again. A use of Fubini's theorem proves

$$\begin{aligned} &\mathbb{E} \left(\langle \exp(-uX) - L(u), f(u) \rangle^2 \right) \\ &= \int_0^\infty \int_0^\infty \int_0^\infty \left(\exp(-ux) - \frac{1}{1+u} \right) \left(\exp(-vx) - \frac{1}{1+v} \right) \\ &\quad \exp(-x) dx \beta(u) f(u) du \beta(v) f(v) dv \\ &= \int_0^\infty \int_0^\infty \left(\frac{1}{1+u+v} - \frac{1}{(1+u)(1+v)} \right) \beta(u) f(u) \beta(v) f(v) du dv = \Delta(f). \end{aligned}$$

Hence,

$$\begin{aligned} \mathbb{E} \left(|\tilde{\zeta}_{p,j}^n(f)|^2 \middle| \mathcal{F}_{\frac{c_{n,p}(j)}{a_n}} \right) &= \frac{1}{(p+1)\ell_n} \Delta(f) \mathbb{E} \left(\left(N \left(\frac{d_{n,p}(j)}{a_n} \right) - N \left(\frac{c_{n,p}(j)}{a_n} \right) \right) \middle| \mathcal{F}_{\frac{c_{n,p}(j)}{a_n}} \right) \\ &= \frac{a_n}{(p+1)\ell_n} \Delta(f) \int_{\frac{c_{n,p}(j)}{a_n}}^{\frac{d_{n,p}(j)}{a_n}} \mu(s, \theta_n) ds. \end{aligned}$$

We finally have to discuss $\mathbb{E} \left(\xi_{p,j}^n \tilde{\zeta}_{p,j}^n(f) \middle| \mathcal{F}_{\frac{c_{n,p}(j)}{a_n}} \right)$, which becomes

$$\frac{1}{(p+1)\ell_n} \sum_{i_1, i_2 \geq 1} \mathbb{E} (U_n(t_{i_1-1}, \theta_n) \langle k_n(u, \theta_n, t_{i_2-1}, t_{i_2}) - L(u), f(u) \rangle \times \mathbf{1}_{\{\frac{c_{n,p}(j)}{a_n} < t_{i_1-1}, t_{i_2-1} \leq \frac{d_{n,p}(j)}{a_n}\}} \middle| \mathcal{F}_{\frac{c_{n,p}(j)}{a_n}}) \quad (3.31)$$

after applying (3.17). The same reasoning also proves that the conditional expectation above vanishes for $i_1 \leq i_2$. On the other hand, for any fixed i_2 we obtain

$$\begin{aligned} & \sum_{i_1 > i_2} \mathbb{E} (U_n(t_{i_1-1}, \theta_n) \langle k_n(u, \theta_n, t_{i_2-1}, t_{i_2}) - L(u), f(u) \rangle \times \\ & \quad \mathbf{1}_{\{\frac{c_{n,p}(j)}{a_n} < t_{i_1-1}, t_{i_2-1} \leq \frac{d_{n,p}(j)}{a_n}\}} \middle| \mathcal{F}_{\frac{c_{n,p}(j)}{a_n}}) \\ &= \mathbb{E} \left(U_n(t_{i_2}, \theta_n) \langle k_n(u, \theta_n, t_{i_2-1}, t_{i_2}) - L(u), f(u) \rangle \mathbf{1}_{\{\frac{c_{n,p}(j)}{a_n} < t_{i_2-1} < t_{i_2} \leq \frac{d_{n,p}(j)}{a_n}\}} \middle| \mathcal{F}_{\frac{c_{n,p}(j)}{a_n}} \right) \\ & \quad + \mathbb{E} \left(\sum_{i_1 > i_2+1} \mathbb{E} \left[U_n(t_{i_1-1}, \theta_n) \mathbf{1}_{\{t_{i_2} < t_{i_1-1} \leq \frac{d_{n,p}(j)}{a_n}\}} \middle| \mathcal{F}_{t_{i_2}} \right] \times \right. \\ & \quad \left. \langle k_n(u, \theta_n, t_{i_2-1}, t_{i_2}) - L(u), f(u) \rangle \mathbf{1}_{\{\frac{c_{n,p}(j)}{a_n} < t_{i_2-1} < t_{i_2} \leq \frac{d_{n,p}(j)}{a_n}\}} \middle| \mathcal{F}_{\frac{c_{n,p}(j)}{a_n}} \right]. \end{aligned}$$

From (3.26) the term above thus becomes

$$\begin{aligned} & \mathbb{E} \left(\mathbf{1}_{\{\frac{c_{n,p}(j)}{a_n} < t_{i_2-1} < t_{i_2} \leq \frac{d_{n,p}(j)}{a_n}\}} \langle k_n(u, \theta_n, t_{i_2-1}, t_{i_2}) - L(u), f(u) \rangle \right. \\ & \quad \left. \left(U_n(t_{i_2}, \theta_n) + \int_{t_{i_2}}^{\frac{d_{n,p}(j)}{a_n}} a_n \frac{\partial}{\partial \theta} \mu(r, \theta_n) dr \right) \middle| \mathcal{F}_{\frac{c_{n,p}(j)}{a_n}} \right) \\ &= \mathbb{E} \left(\mathbb{E} \left(\mathbf{1}_{\{t_{i_2-1} < t_{i_2} \leq \frac{d_{n,p}(j)}{a_n}\}} \langle k_n(u, \theta_n, t_{i_2-1}, t_{i_2}) - L(u), f(u) \rangle \right. \right. \\ & \quad \left. \left. \left(U_n(t_{i_2}, \theta_n) + \int_{t_{i_2}}^{\frac{d_{n,p}(j)}{a_n}} a_n \frac{\partial}{\partial \theta} \mu(r, \theta_n) dr \right) \middle| \mathcal{F}_{t_{i_2-1}} \right) \mathbf{1}_{\{\frac{c_{n,p}(j)}{a_n} < t_{i_2-1} \leq \frac{d_{n,p}(j)}{a_n}\}} \middle| \mathcal{F}_{\frac{c_{n,p}(j)}{a_n}} \right). \end{aligned}$$

We apply (3.24). Hence, setting

$$\begin{aligned} \alpha_n(t, u) &= \int_t^{\frac{d_{n,p}(j)}{a_n}} \left(\exp \left(-u \int_t^s a_n \mu(r, \theta_n) dr \right) - L(u) \right) \times \\ & \quad \left(U_n(s, \theta_n) + \int_s^{\frac{d_{n,p}(j)}{a_n}} a_n \frac{\partial}{\partial \theta} \mu(r, \theta_n) dr \right) \exp \left(- \int_t^s a_n \mu(r, \theta_n) dr \right) a_n \mu(s, \theta_n) ds \end{aligned}$$

and utilizing Fubini's theorem, (3.31) becomes

$$\begin{aligned} & \frac{1}{(p+1)\ell_n} \left\langle \mathbb{E} \left(\sum_{i_2 \geq 1} \alpha_n(t_{i_2-1}, u) 1_{\{\frac{c_{n,p}(j)}{a_n} < t_{i_2-1} \leq \frac{d_{n,p}(j)}{a_n}\}} \middle| \mathcal{F}_{\frac{c_{n,p}(j)}{a_n}} \right), f(u) \right\rangle \\ &= \frac{1}{(p+1)\ell_n} \left\langle \int_{\frac{c_{n,p}(j)}{a_n}}^{\frac{d_{n,p}(j)}{a_n}} a_n \alpha_n(t, u) \mu(t, \theta_n) dt, f(u) \right\rangle. \end{aligned}$$

Regarding the inner integral, we obtain

$$\begin{aligned} \int_{\frac{c_{n,p}(j)}{a_n}}^{\frac{d_{n,p}(j)}{a_n}} a_n \alpha_n(t, u) \mu(t, \theta_n) dt &= \int_{\frac{c_{n,p}(j)}{a_n}}^{\frac{d_{n,p}(j)}{a_n}} \frac{1}{1+u} \left(U_n(s, \theta_n) + \int_s^{\frac{d_{n,p}(j)}{a_n}} a_n \frac{\partial}{\partial \theta} \mu(r, \theta_n) dr \right) \times \\ &\quad \left(\exp \left(- \int_{\frac{c_{n,p}(j)}{a_n}}^s a_n \mu(r, \theta_n) dr \right) - \exp \left(- \int_{\frac{c_{n,p}(j)}{a_n}}^s (1+u) a_n \mu(r, \theta_n) dr \right) \right) a_n \mu(s, \theta_n) ds \end{aligned}$$

from Fubini's theorem first. Evaluating the latter integral is hard, but several applications of Condition 3.2.1(c) as well as ℓ_n being of the order a_n^ϱ , $0 < \varrho < 1/2$, allow to replace $\mu(s, \theta_n)$ by $\mu(\frac{c_{n,p}(j)}{a_n}, \theta_n)$ with an error of small order, and similarly for the derivatives. Also, the summand involving $U_n(s, \theta_n)$ is of small order as well. Hence the approximation

$$\begin{aligned} \int_{\frac{c_{n,p}(j)}{a_n}}^{\frac{d_{n,p}(j)}{a_n}} a_n \alpha_n(t, u) \mu(t, \theta_n) dt &= \int_{\frac{c_{n,p}(j)}{a_n}}^{\frac{d_{n,p}(j)}{a_n}} \frac{1}{1+u} a_n^2 \frac{\partial}{\partial \theta} \mu\left(\frac{c_{n,p}(j)}{a_n}, \theta_n\right) \left(\frac{d_{n,p}(j)}{a_n} - s \right) \times \\ &\quad \left(\exp \left(-a_n \mu\left(\frac{c_{n,p}(j)}{a_n}, \theta_n\right) \left(s - \frac{c_{n,p}(j)}{a_n} \right) \right) \right. \\ &\quad \left. - \exp \left(-a_n(u+1) \mu\left(\frac{c_{n,p}(j)}{a_n}, \theta_n\right) \left(s - \frac{c_{n,p}(j)}{a_n} \right) \right) \right) \mu\left(\frac{c_{n,p}(j)}{a_n}, \theta_n\right) ds (1 + o(1)) \end{aligned}$$

with a small order term uniform in θ and u holds (note again that p is fixed). To evaluate the latter integral we use

$$\int_a^b \exp(-K(s-a))(b-s) ds = \frac{(b-a)K - (1 - \exp(-(b-a)K))}{K^2}$$

for generic positive a, b and K , and we see that the latter fraction to first order equals $\frac{b-a}{K}$ in our setting. To summarize,

$$\int_{\frac{c_{n,p}(j)}{a_n}}^{\frac{d_{n,p}(j)}{a_n}} a_n \alpha_n(t, u) \mu(t, \theta_n) dt = \frac{1}{1+u} \left(1 - \frac{1}{1+u} \right) p \ell_n \frac{\partial}{\partial \theta} \mu\left(\frac{c_{n,p}(j)}{a_n}, \theta_n\right) (1 + o(1))$$

with a small order term as above. Using Condition 3.2.1(c) again we can then write

(3.31) as

$$\frac{p}{p+1} \Phi(f) \frac{\partial}{\partial \theta} \mu\left(\frac{c_{n,p}(j)}{a_n}, \theta_n\right) (1 + o(1)) = \frac{a_n}{(p+1)\ell_n} \Phi(f) \int_{\frac{c_{n,p}(j)}{a_n}}^{\frac{d_{n,p}(j)}{a_n}} \frac{\partial}{\partial \theta} \mu(s, \theta_n) ds (1 + o(1)).$$

The result is now easy to conclude from Condition 3.2.1(c) again. \square

References

- G. Jogesh Babu and C. R. Rao. Goodness-of-fit tests when parameters are estimated. *Sankhyā: The Indian Journal of Statistics (2003-2007)*, 66(1):63–74, 2004. ISSN 0972-7671. URL <http://www.jstor.org/stable/25053332>.
- Luc Bauwens and Nikolaus Hautsch. Modelling financial high frequency data using point processes. In *Handbook of Financial Time Series*, pages 953–979. Springer Berlin Heidelberg, 2009. doi: 10.1007/978-3-540-71297-8_41.
- M. S. Bebbington and C. D. Lai. On nonhomogeneous models for volcanic eruptions, jul 1996.
- Mark Bebbington. Models for temporal volcanic hazard. *Statistics in Volcanology*, 1:1–24, jan 2013. doi: 10.5038/2163-338x.1.1.
- A. N. Burkitt. A review of the integrate-and-fire neuron model: Ii. inhomogeneous synaptic input and network properties. *Biological Cybernetics*, 95(2):97–112, July 2006. ISSN 1432-0770. doi: 10.1007/s00422-006-0082-8.
- Axel Bücher and Ivan Kojadinovic. A note on conditional versus joint unconditional weak convergence in bootstrap consistency results. *Journal of Theoretical Probability*, 32(3):1145–1165, March 2018. ISSN 1572-9230. doi: 10.1007/s10959-018-0823-3.
- Giuseppe Cavaliere, Ye Lu, Anders Rahbek, and Jacob Stærk-Østergaard. Bootstrap inference for hawkes and general point processes. *Journal of Econometrics*, 235(1):133–165, July 2023. ISSN 0304-4076. doi: 10.1016/j.jeconom.2022.02.006.
- Feng Chen and Peter Hall. Inference for a nonstationary self-exciting point process with an application in ultra-high frequency financial data modeling. *Journal of Applied Probability*, 50(4):1006–1024, dec 2013. doi: 10.1239/jap/1389370096.

- E. S. Chornoboy, L. P. Schramm, and A. F. Karr. Maximum likelihood identification of neural point process systems. *Biological Cybernetics*, 59(4-5):265–275, sep 1988. doi: 10.1007/bf00332915.
- Claire L. Cooper, Graeme T. Swindles, Ivan P. Savov, Anja Schmidt, and Karen L. Bacon. Evaluating the relationship between climate change and volcanism. *Earth-Science Reviews*, 177:238–247, feb 2018. doi: 10.1016/j.earscirev.2017.11.009.
- D. A. Darling. The cramer-smirnov test in the parametric case. *The Annals of Mathematical Statistics*, 26(1):1–20, mar 1955. doi: 10.1214/aoms/1177728589.
- C. Dion-Blanc, D. Hawat, E. Lebarbier, and S. Robin. Multiple change-point detection for some point processes, February 2023.
- J. Durbin. Weak convergence of the sample distribution function when parameters are estimated. *The Annals of Statistics*, 1(2), mar 1973. doi: 10.1214/aos/1176342365.
- Philip Protter Jean Jacod. *Probability Essentials*. Springer Berlin Heidelberg, June 2004. ISBN 3540438718.
- A. Mark Jellinek, Michael Manga, and Martin O. Saar. Did melting glaciers cause volcanic eruptions in eastern california? probing the mechanics of dike formation. *Journal of Geophysical Research: Solid Earth*, 109(B9):n/a–n/a, sep 2004. doi: 10.1029/2004jb002978.
- M. Kac, J. Kiefer, and J. Wolfowitz. On tests of normality and other tests of goodness of fit based on distance methods. *The Annals of Mathematical Statistics*, 26(2): 189–211, jun 1955. doi: 10.1214/aoms/1177728538.
- Steffen. Kutterolf, Marion Jegen, Jerry X. Mitrovica, Tom Kwasnitschka, Armin Freundt, and Peter J. Huybers. A detection of milankovitch frequencies in global volcanic activity. *Geology*, 41(2):227–230, feb 2013. doi: 10.1130/g33419.1.
- Hubert W. Lilliefors. On the kolmogorov-smirnov test for normality with mean and variance unknown. *Journal of the American Statistical Association*, 62(318): 399–402, jun 1967. doi: 10.1080/01621459.1967.10482916.
- Simos Meintanis and Jan Swanepoel. Bootstrap goodness-of-fit tests with estimated parameters based on empirical transforms. *Statistics & Probability Letters*, 77 (10):1004–1013, jun 2007. doi: 10.1016/j.spl.2007.01.014.

- Yoshiko Ogata. The asymptotic behaviour of maximum likelihood estimators for stationary point processes. *Annals of the Institute of Statistical Mathematics*, 30(2):243–261, dec 1978. doi: 10.1007/bf02480216.
- Yoshihiko Ogata. Statistical models for earthquake occurrences and residual analysis for point processes. *Journal of the American Statistical Association*, 83(401):9–27, mar 1988. doi: 10.1080/01621459.1988.10478560.
- Julio Cesar Louzada Pinto, Tijani Chahed, and Eitan Altman. Trend detection in social networks using hawkes processes. In *Proceedings of the 2015 IEEE/ACM International Conference on Advances in Social Networks Analysis and Mining 2015*, ASONAM '15, pages 1441–1448. ACM, August 2015. doi: 10.1145/2808797.2814178.
- Michael R. Rampino, Stephen Self, and Rhodes W. Fairbridge. Can rapid climatic change cause volcanic eruptions? *Science*, 206(4420):826–829, nov 1979. doi: 10.1126/science.206.4420.826.
- Marian-Andrei Rizoiu, Young Lee, Swapnil Mishra, and Lexing Xie. *Hawkes processes for events in social media*, pages 191–218. Association for Computing Machinery and Morgan & Claypool, December 2017. ISBN 9781970001075. doi: 10.1145/3122865.3122874.
- Alan Robock. Volcanic eruptions and climate. *Reviews of Geophysics*, 38(2):191–219, may 2000. doi: 10.1029/1998rg000054.
- Jacopo Selva, Laura Sandri, Matteo Taroni, Roberto Sulpizio, Pablo Tierz, and Antonio Costa. A simple two-state model interprets temporal modulations in eruptive activity and enhances multivolcano hazard quantification. *Science Advances*, 8(44), nov 2022. doi: 10.1126/sciadv.abq4415.
- Aad W. van der Vaart and Jon A. Wellner. *Weak Convergence and Empirical Processes*. Springer New York, 1996. ISBN 9781475725452. doi: 10.1007/978-1-4757-2545-2.
- A.W. Van Der Vaart. *Asymptotic Statistics*. Cambridge Series in Statistical and Probabilistic Mathematics, 3. Cambridge University Press, 1998. ISBN 9780521496032. URL <https://books.google.de/books?id=udhfQgAACAAJ>.
- D. Vere-Jones. On the estimation of frequency in point-process data. *Journal of Applied Probability*, 19(A):383–394, 1982. doi: 10.2307/3213577.

Chapter 4

Cyclicity and distinction of geological processes from thickness and frequency of event beds: A compilation of international drilling legacy datasets

Chang, Y., **Kling, J.C.F.**, Schindlbeck-Belo, J.C., Mitchel, N., Hsiung, K.,
Kanamatsu, T.

To be submitted, work in progress.

Sediment successions around volcanic islands are archives of volcanoclastic material derived with different emplacement processes over long timescales. The deposits of these events have been used to unravel volcanic island histories (e.g., Chang et al., 2023; Masson et al., 2002; Wall-Palmer et al., 2014), emplacement processes (Chang et al., 2021a; Schindlbeck et al., 2013; Trofimovs et al., 2007), and dynamics of sediment flows (Migeon et al., 2012; Talling, 2001). In general, seafloor basins receive substantial volcanoclastic-rich sediments directly from volcanic processes during the volcano growth stage, such as pyroclastic fallout, sea entering pyroclastic flows and reworked sediment gravity flow deposits (e.g., Chang et al., 2021a; Gill et al., 2018; Schmincke and Sumita, 1998). However, awareness must be given while interpreting the deposits because diverse factors can influence depositional records. For instance, the emplaced sediments can be obscured or diminished after extensive transport, high degrees of bypass or erosion (e.g., Hunt et al., 2013; Sinclair and Cowie, 2003) and bioturbation (e.g., Berger and Heath, 1968). The geomorphological settings that sediments have gone through (submarine canyon and depositional basins) also affect distributed areas and thicknesses of turbidites (e.g., Wall-Palmer et al., 2014).

The ages and volumes of the volcanoclastic-rich deposits in the Madeira Abyssal Plain were used to reconstruct the evolution history of the adjacent Meteor-Cruiser Seamount Complex (Hunt and Jarvis, 2020). High frequencies (i.e., event occurrence) of volcanoclastic event bed were interpreted to reflect the growth of volcanoes. Calciclastic turbidites outnumbering tephra fallout and volcanoclastic turbidites were interpreted as a shifting of generation mechanism from volcanism to slope failure results. Thick volcanic beds broadly deposited proximal to volcanic islands indicate recurrent large volcanic flank collapses (e.g., Garcia, 1996; Hunt and Jarvis, 2017) and ignimbrite eruptions (e.g., Chang et al., 2023; Pimentel et al., 2021; Schmincke and Segschneider, 1998).

Thickness-frequency distributions of event beds have been used to characterize the depositional records (Hiscott et al., 1992; Talling, 2001) and related to the physical processes generating sediment flow (Beattie and Dade, 1996). For example, the Oligocene succession of those sandy volcanoclastic beds thicker than 10 cm in the Izu forearc basin shows the thickness-frequency distribution with a power-law slope gradient of about -1.0, similar to the scaling relationship observed in earthquake magnitudes if equating magnitude, which scales logarithmically with earthquake energy, with \log_{10} (thickness). This similar scaling suggests that earthquakes or earthquake-induced slope failures could be the mechanisms responsible for the observed inverse power-law distribution of event beds (Beattie and Dade, 1996;

Chen and Hiscott, 1999).

However, the thickness and frequency of event beds do not always adhere to such scaling relationships. Instead, diverse types of distributions have been found in various settings. For instance, truncated Gaussian (Mizutani and Hattori, 1972), exponential (Drummond and Wilkinson, 1996), log-normal (Aitchison and Brown, 1981; Carlson and Grotzinger, 2001; Drummond and Wilkinson, 1996; Talling, 2001; Turcotte, 1991) and power-law (Carlson and Grotzinger, 2001; Chen and Hiscott, 1999; Sinclair and Cowie, 2003) have exhibited in the siliciclastic sandstone and mudstone formations. Log-normal and power-law distributions appear more common among these (Talling, 2001). Moreover, distributions do not always follow these parametric models. Instead, they can be complex, likely due to the involvements of multiple influential factors (e.g., Pantopoulos et al., 2018, 2013; Talling, 2001), although blended distribution models can resolve some of them (Pantopoulos et al., 2013).

Variations among different thickness-frequency distributions have been explained to arise from different generation mechanisms (Beattie and Dade, 1996) or from different influences on the sedimentary flows from source to depositional areas, such as initial volume (Pirmez and Imran, 2003), flow rheological properties (Talling, 2001), transportation distance (Carlson and Grotzinger, 2001), and basin geometry (Marini et al., 2016; Prekopová and Janočko, 2009; Sinclair and Cowie, 2003). Engagement of multiple factors and the uneven contributions from different factors usually make the adjustment of distribution not inherently predictable (Talling, 2001). Although some factors have been discussed (e.g., Marini et al., 2016; Talling, 2001) and simulated (e.g., Carlson and Grotzinger, 2001; Sinclair and Cowie, 2003) in some specific settings (e.g., submarine fans and basins) based on a simplified monotonous generation mechanism of sediment flows. Despite the complications, thickness and frequency distribution analyses have successfully applied to produce turbidite reservoir models (e.g., Pantopoulos et al., 2018), to characterize the subdivisions of depositional environments (Chen and Hiscott, 1999; Carlson and Grotzinger, 2001; Pantopoulos et al., 2013), and to assess the relative probability of large hazards (e.g., Chang et al., 2021a).

The periodicities of event bed emplacements could also reflect the processes governing event generation. For example, fluctuations of solar radiation can affect the growth of ice-sheets and sea-level height, recurring the adjustments of loading stress on the magma body. The cyclical orbital movements, also known as Milankovitch cycles, are thought to be the cause of long-term climate cycles (Berger, 1988) and have been suggested to be responsible for the observed volcanic and

tectonic cycles (Gudmundsson, 1986; Jellinek et al., 2004; Jull and McKenzie, 1996; Nowell et al., 2006; Rawson et al., 2016). The repetitive high eruption frequency at Santorini Volcano during the cooling periods of the last 360 kyr for example has been interpreted to result from more frequent dyke injections encouraged by the eustasy-induced stress reduction (Satow et al., 2021), although the causality is still under debate

(Walker et al., 2023). The 100-kyr eccentricity 115 cycle (i.e., the orbital shape of Earth) coincides with the significant frequency peak of tephra beds from the Izu Arc emplaced over the last 1 Myr . Finding an unequivocal causative link between Earth's climate and volcanism remains challenging, especially when the data span insufficient glacial-interglacial cycles or where other factors impact more on bed emplacements. The complexity suggests that extensive geological records and datasets with adequate knowledge of geological backgrounds from source to depositional areas need to be justified such links.

In this study, extensive depositional records with comprehensive event beds have been extracted for seven oceanic drilling sites to explore thickness-frequency and periodicity analyses (Fig. 4.1 and Table 4.1). Their relatively proximal localities and nearly stationary distances to the source areas over the evolution also allow these sites to record the temporal variations in the source areas. This research aims to: 1) Characterize and compare the thickness frequency distributions of event beds across different volcano development stages and geological settings using a combination of statistical analyses, and 2) compute the power spectrum to determine the cycles of event frequency. Those results are intended to: 1. broaden the understanding of how different geological factors modulate the features of thickness-frequency distributions. 2. address the difficulty in comparing depositional records that do not follow parametric distribution models, and reveal the recurrence periods of event cycles and assess the mechanisms causing them.

4.1 Geological background

Sediment successions of four volcanic settings (Fig. 4.1) sampled by the International Ocean Discovery Program (IODP) and the Ocean Drilling Program (ODP) are investigated. The sites lie within, the Lesser Antilles Arc (IODP Exp. 340), the Izu Arc (IODP Exp. 350), and Kyushu-Palau Ridge (IODP Exp. 351) and the Canary Islands (ODP Leg 157).

Exp. / Leg No.	Site No.	Water depth (mbsl)	Distance to main source areas (km)	Total cored interval (m)	Studied interval (m)	Valid sedi- ment records (%) ¹	Analysed age span (Ma)	Number of event beds	Details of age range, location and dating methods where available.
351	U1438	4700	≈ 80	1604.1	1461.08	≈ 77	0-48.7	2024	Located at the Kyushu-Palau arc, experiencing subduction initiation (52–50 Ma), arc growth (40.2–28.8), to back-arc spreading (24.3 Ma–present).
350	U1437	2117	≈ 50	1798.6	1306.38	≈ 80	0-8.75	2026	Located at the Izu-Bonin rear arc where extension has developed in between the rear and front arcs since 3 Ma. About 1 Myr high-resolution climate records (14 glacial cycles) dated with $\delta^{18}O$ and tephrostratigraphy.
350	U1436	1776	≈ 60	70.3	70.29	≈ 99	0–0.9	168	Located at the Izu-Bonin arc front.
340	U1394	1115	≈ 13	181.4	153.77	≈ 73	0–0.3	141	≈ 300 kyr of high-resolution climate records (4 glacial cycles) dated with $\delta^{18}O$.
157	953	3578	≈ 68	1158.7	201.5	≈ 66	13.35–14	59	Located south of Gran Canaria Island. The selected studied interval is from the active volcano growth stage, with volcanoclastic sediments mainly sourced from Gran Canaria. Sediments were channelled from the highly dissected volcano shield on the northern part of island.
157	955	2854	≈ 56	599.4	96.1	≈ 65	13.35–14	70	Located south of Gran Canaria Island. The selected studied interval is from the active volcano growth stage, with volcanoclastic sediments mainly sourced from Gran Canaria. A gentle and undissected volcanic apron on the southern island results in a more moderate concentric sediment dispersal.
157	956	3442	≈ 45	703.5	125.4	≈ 46	13.35–14	48	Located south of Gran Canaria Island. The selected studied interval is from the active volcano growth stage, with volcanoclastic sediments mainly sourced from Gran Canaria. A gentle and undissected volcanic apron on the southern island resulted in a more concentric sediment dispersal.

Table 4.1: Details of core information. ¹Percentage of stratigraphy available for interpretation considering core recovery and core disturbance.

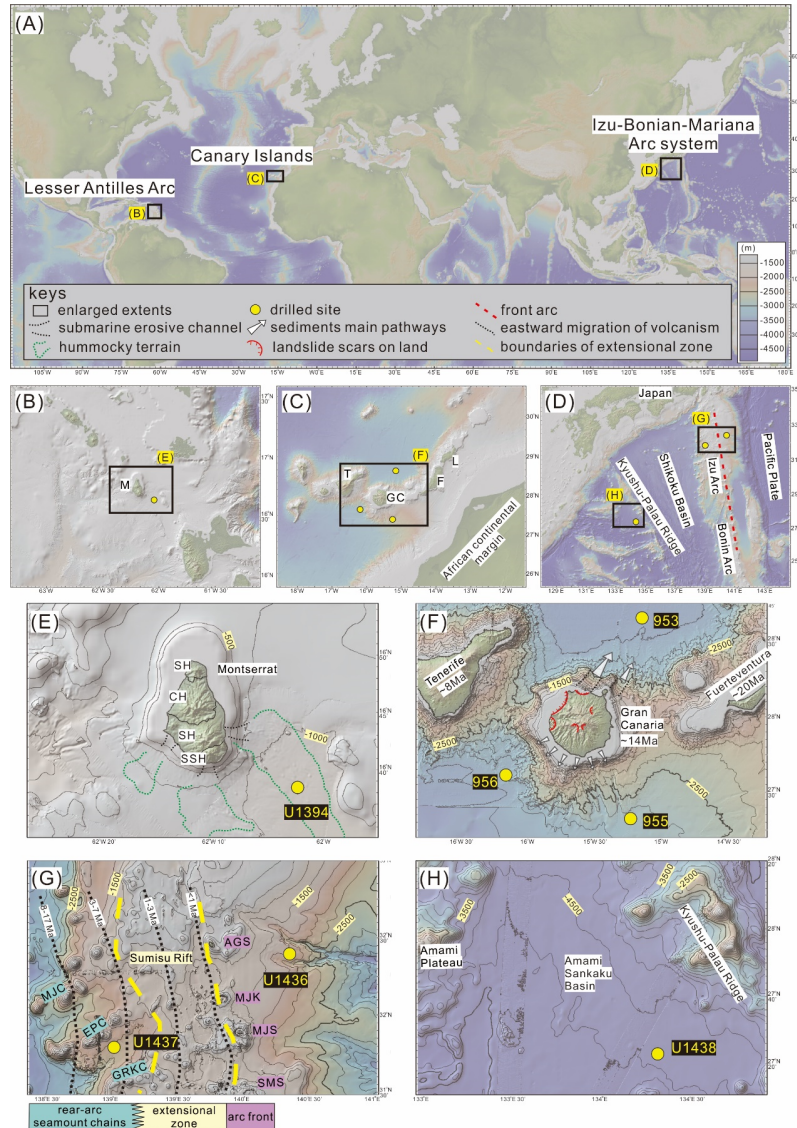


Figure 4.1: Maps of research areas. (a) Global map of study areas (black rectangles). Enlargements with drilling sites (yellow dots) include (b) Montserrat, (c) Gran Canaria, and (d) Izu-Bonin Arc and Kyushiu-Palau Ridge. M, GC, T, F and L in (b) and (c) represent Montserrat, Gran Canaria, Tenerife, Fuerteventura and Lanzarote Islands. More detailed enlargements annotated with geological features encompass drilling Sites (e) U1394, (f) 953, 955 and 956, (g) U1436 and U1437 and (h) U1438. SH, CH, SH, SSH MJC, EPC, GRKC, AGS, MJK, MJS and SMS in (e) and (g) represent Silver Hills, Centre Hills, South Soufrière Hills, and Soufrière Hills, Manji Chain, Enpo Chain, Genroku Chain, Aogashima, Myojin Knoll, Myojinsho and Sumisu, respectively. Basemaps were generated with GeoMapApp (www.geomapapp.org; Ryan et al., 2009) and have a contour interval of 250 m.

4.1.1 Montserrat, Lesser Antilles arc

Montserrat, located at the northern arc of the Lesser Antilles arc, evolved chronologically from the north to the south of island (Harford et al., 2002, ; Fig. 4.1E): Silver Hills (2600-1200 ka), Centre Hills (550-950 ka), and South Soufrière Hills-Soufrière Hills (≈ 170 ka to present). The long-term erosional processes on the island north have formed a broad, flat, shallow submarine shelf in the north (Le Friant et al., 2004). In contrast, intense volcanisms such as dome-forming eruptions (Cole et al., 2001), collapses of subaerial edifices (Voight et al., 2002; Young et al., 2002) and periodical seismic crisis (Perret, 1939; Shepherd et al., 1971) still occur in the south of the island during the last 300 years (Robertson et al., 2000; Shepherd et al., 1971).

IODP site U1394 (offshore Montserrat)

Site U1394, located ≈ 24 km off the southeast of Montserrat, was drilled on the basin seafloor with the presence of debris avalanche (IOD, 2012, ; Fig. 4.1E), indicating the history of repetitive flank collapse (Lebas et al., 2011). About 300 kyr high-resolution climate records (4 glacial-interglacial cycles) were reconstructed by the $\delta 18\text{O}$ of the calcareous nannofossils and planktonic foraminifers (Coussens et al., 2016, ; Fig. 4.2A). Marine sedimentation offshore Montserrat is directly influenced by volcanism (i.e., dome-forming eruptions since 1995; Trofimovs et al. (2006, 2007) and remobilized sediments from slope collapses (≈ 14 ka carbonate platform failure; Trofimovs et al. (2011), which could be triggered by destructive earthquakes (e.g., Chang et al., 2021b; Watt et al., 2014) or climate responses (Chang et al., 2023; Quidelleur et al., 2008).

4.1.2 Izu arc

The Izu Arc constitutes the northern segment of the current Izu-Bonin-Mariana (IBM) Arc (Fig. 4.1H). The Neogene IBM arc initiation began around 22 Ma, following the spreading of the Kyushu-Palau Ridge (Ishizuka et al., 2003). Between 24.3 and 17 Ma, mild magmatism drove the IBM arc front slightly westward from its Eocene-Oligocene position (i.e., Kyushu-Palau Ridge), while magmatism in the rear arc seemed to cease during this period (Ishizuka et al., 2011; Taylor, 1992). Volcanisms became dynamic since 13 Ma in the frontal arc and within 12-9 Ma in the back arc (Ishizuka et al., 2003; Sato et al., 2020), producing parallel seamount chains (Fig. 4.1G). Despite the eastward-migrating of the rear arc front, volcanism persisted across the broader rear arc area (Ishizuka et al., 2003, ; Fig. 4.1G). Volcanic

deposits were coarse, and the sediment transportation to the arc front was prohibited due to the seafloor topography during this period (Hochstaedter et al., 2001; Tamura et al., 2007). Nonetheless, fine-grained ashfall can still be carried by the surface current to the arc front (i.e., Gill et al., 2018). From 3 Ma to the present, a ≈ 100 km wide extensional zone developed behind the arc front (Fig. 4.1G), overlapping the eastern half of the rear-arc seamount (Ishizuka et al., 2003). Small rift-type volcanoes (back-arc knolls) developed on the extensional zone during this period and discharged bimodal compositions of volcanoclastic particles through density and surface currents into both arc sides (Hochstaedter et al., 2001).

IODP sites U1436 and U1437 (Izu arc)

Site U1436 is located at ≈ 60 km from the Izu arc front area and drilled on a slope semi-confined by a fork-shape canyon (Fig. 4.1G). A ≈ 1 -Myr history of explosive volcanism of the late Pleistocene arc front was derived from the ≈ 70 m sediment cores (Tamura et al., 2015, ; Fig. 4.2B). Site U1437 is located in the Izu rear arc 30-60 km to the volcanism areas and drilled in a downward dipping semi-confined basin similar to U1436. In total 1.8 km of sediments were recovered providing a ≈ 9 -Myr archive of rear arc volcanism. At least 14 interglacial-glacial cycles over the last 1 Myr have been resolved by the high-resolution $\delta^{18}\text{O}$ (U1436; Vautravers et al. (2016) and tephrostratigraphic time markers (U1437; Schindlbeck et al. (2018b) age-depth models.

4.1.3 Kyushu-Palau ridge

The Kyushu-Palau Ridge is the Oligocene remnant of a proto Izu-Bonin-Mariana arc. It is located approximately 600 km west of the current IBM arc (Fig. 4.1D). About 50 Myr depositional history has been reconstructed through high-resolution magnetostratigraphy at Site U1438 (Maffione and Morris, 2022) and the dating of volcanic rocks (Arculus et al., 2015; Ishizuka et al., 2006a,b, 2011, 2018). The subduction of the Pacific plate started around 52-50 Ma (e.g., Ishizuka et al., 2018), followed by rear-arc magmatism and diffusive pre-arc volcanism between 48.7 and 45.6 Ma (Robert J. Stern, 1992). The Kyushu-Palau Ridge began to develop around 43.2 Ma and peaked at 28.8 Ma (Maffione and Morris, 2022), characterized by the coarsest grain size proximal volcanic edifice (Johnson et al., 2021). Subsequently, the arc experienced rifting, leading to the gradual cessation until seafloor spreading at 24.3 Ma (Ishizuka et al., 2011), marking the shutdown of the Kyushu-Palau Ridge and separation from the present IBM arc.

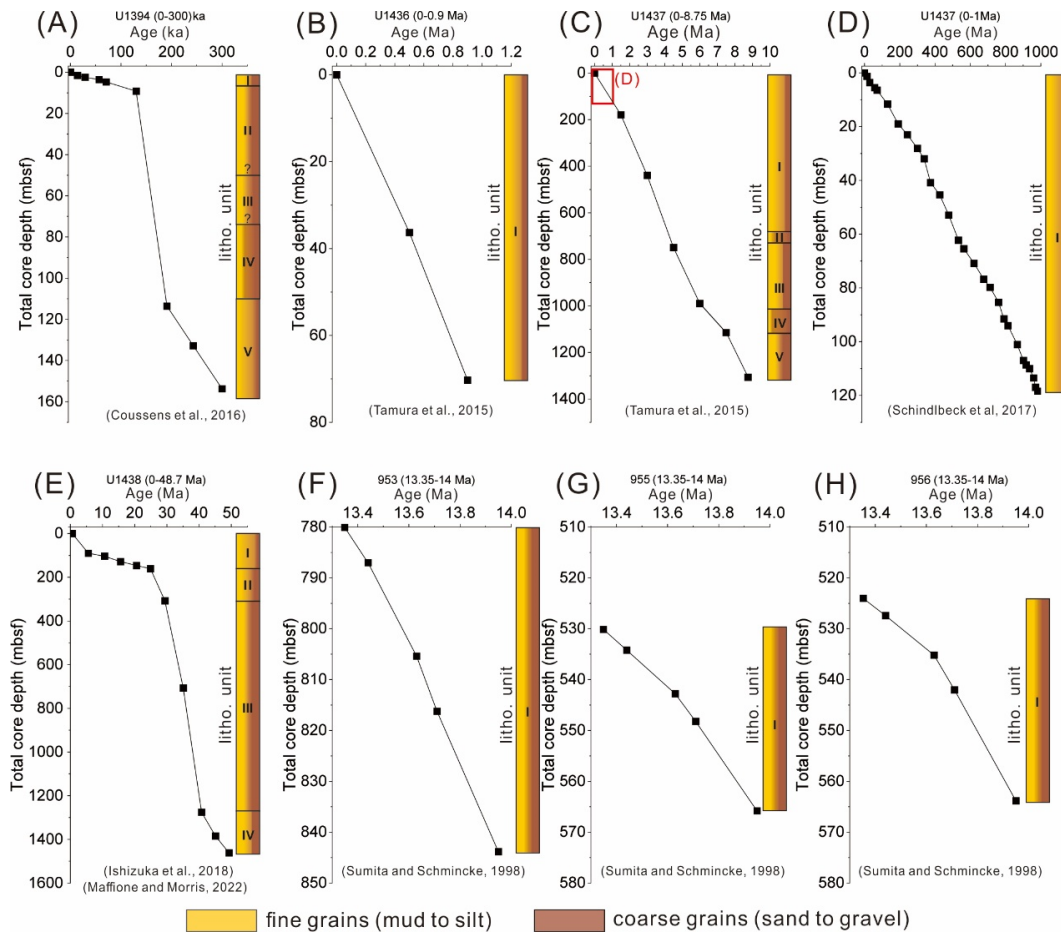


Figure 4.2: Compiled age-depth models and simplified lithostratigraphic units of cores: (a) Site U1394, (b) Site U1436, (c) Site U1437, (d) Site U1437 (0–1 Ma only), (e) Site U1438, (f) Site 953, (g) Site 955, (h) Site 956. At all sites, cores comprise hemipelagites and event beds. Black squares are age constraints (references below each panel). Colors represent the relative proportions of fine and coarse grains. Question marks in (a) represent indistinct boundaries. Note that the scales differ between panels and the stratigraphy top are not all zero.

IODP site U1438 (Kyushu-Palau ridge)

Site U1438 is located ≈ 80 km west of the Kyushu-Palau Ridge (Fig. 4.1H) and drilled within the Amami Sankaku Basin, where no complex structures developed (Expedition 351 Scientists, 2014). At site U1438 1.6 km sediments have been recovered which comprise the last ≈ 50 -Myr of arc development (Fig. 4.2E) (Arculus et al., 2015; Ishizuka et al., 2006a,b, 2011, 2018; Maffione and Morris, 2022). The present inactive geological environments around U1438 were explored by deep submerging in 1996 (Shinkai 6500 Dive 337), showing altered volcanic particles on the seafloor covered by hemipelagic particles (Fujioka et al., 1997).

4.1.4 Gran Canaria, Canarian archipelago

Gran Canaria is the center of the Canarian archipelago align offshore northwestern Africa (Fig. 4.1C). According to a unifying model (Anguita and Hernán, 2000), the evolution of Gran Canaria involved three stages (Schmincke, 1976): a shield volcano stage (14.5-9 Ma), a volcanic hiatus stage (9-5 Ma), and a rejuvenated volcanism stage (5 Ma to present). In this study, only the sediments from the Mogán group (14-13.3 Ma) of the shield volcano stage were investigated, characterized by intense and frequent explosive eruptions. The trachytic to rhyolitic lava and ignimbrite preserved in the Mogán group represent the most active stage Gran Canaria (Schmincke and Segschneider, 1998) with the largest volume of felsic volcanic rocks (300-500 km³ dense rock equivalent; DRE) and a giant caldera collapse (≈ 20 km in diameter).

ODP sites 953, 955 and 956

Sites 953, 955, and 956 are located northeast, southeast, and southwest of Gran Canaria, respectively (Fig. 4.1F). These sites were drilled into the flat volcanic apron with simple structures. Volcaniclastic particles mainly originated from Gran Canaria during the shield volcano stage (H.U. Schmincke, 1998), with minor siliciclastic sediments from the African margin. Site 953 includes deposits from the Mogán group that are twice as thick as those at Sites 955 and 956 (Fig. 4.2F, G, H). The thickness difference can be explained by highly dissected canyons on the northern island (Paris, 2002) efficiently channeling sediment into the sea, in contrast to the broad and moderate concentric sediment dispersal system on the island south.

4.2 Materials and methods

In sum 3.65-km of sediment records (Table 4.1) were collected during IODP Expeditions 340, 350 and 351 (Sites U1394, U1436, U1437, and U1438), located relatively proximal to their volcanic source areas. Depositional timespans range from 300 kyr to 50 Myr with an overall good sediment recovery (Table 4.1). Event bed identification and thickness measurement relied on the integration of visual core descriptions, core scanning images, and expedition published stratigraphy. Digitized data was obtained from the IODP open access archive systems: Descriptive Information LIMS Report (<https://web.iodp.tamu.edu/DESCReport/>), IMAGES directories and expedition chapters. Diverse non-genetic descriptive data were

extracted, including depths, (sub)-dominant lithologies, sedimentary structures, grain size, sorting, roundness, bulk compositions, microfossil abundance, bioturbation, and nature of boundary contacts.

4.2.1 Rationale of event bed discrimination

In this study, an "event bed" refers to a bed formed over a short interval (i.e., seconds to a few days) due to volcanic (e.g., eruptions) or non-volcanic processes (e.g., slope failures induced by various causes). Conversely, a "non-event bed" refers to clay-rich and burrowed mud sedimentation during the quiescent interval (e.g., pelagite and hemipelagite). "Event beds" from "non-event beds" were differentiated based on the integrations of diverse data, following the criteria used in Chang et al. (2021a). Event beds in volcanic settings are characterized by high percentages of volcanic particles (>75%), tractional structures and low abundances of intact microfossils. Shelf-origin biogenic fragments could also be found for those originating from slope failures. Conversely, non-event beds are determined by clay-rich successions, bioturbated structures, and moderate to high abundances of intact microfossils. Event bed discrimination in many cases challenging due to post-depositional processes (e.g., bioturbation), obscuring primary sedimentary structures. This underscores that bed-type discrimination should rely on combined considerations rather than a single criterion.

4.2.2 Data quality check - validity rates of sediment records

The validity rates of sediment records are calculated by dividing the "effectively-used" sediment interval by the total lengths of the core barrel. Factors that may affect the rates are also considered. For example, unconsolidated soft sediments from the

shallow depth may experience expansion after being recovered. Onboard core procedures directly sampled small portions of sediment (e.g., 10-15 cm) approximately every ten meters. Both factors are considered mild compared to the influences caused by drilling procedures. Core drilling and handling processes could cause diverse disturbances (e.g., Jutzeler et al., 2014), including fall in, basal flow-in, polymictic textures, and ruptured structures. These disturbances could greatly smear, distort, destroy and remove beds (e.g., Yang et al., 2019), making the event discrimination, frequency counting, and thickness measurement challenging. In this study, those severe and destroyed sediment intervals from the analyses have been excluded.

4.2.3 Data processing

Three processing steps (i.e., trimming, revising and classifying) are employed to adapt the inconsistently descriptive records across different expeditions.

Trimming: removing repeated documentation

The sub-intervals and the whole thick sediment interval are repeatedly documented and must be removed to prevent double counting.

Revising: merging successions and subdividing amalgamated beds

Over- and under-segmentation of sediments are found in the logging sheets. The prior could result in bed thickness underestimates and event frequency overestimates, while the latter causes opposite results. In this study, sub-intervals are merged if (1) fine-grained sediments grade upward immediately above the coarse-grained interval, (2) similar sediment features or a gradual change appears at the bottom and the top of two adjacent cores, (3) a short sediment segment is missed in the middle of a consistent long segment due to onboard sampling (e.g., whole-round multisensor logger and palaeomagnetism) or coring processes. In contrast, segments are separated if (1) erosional surfaces, sudden grain size changes, or repeated sequences of sedimentary structures are found in the amalgamated sediment beds (e.g., Mattern, 2002; Walker, 1967), (2) long sediment segments are documented by only marking the structures of intercalated/interbedded (stratified) beds.

Classifying: sorting event beds

A decision tree was constructed for sorting event beds by considering sediment composition, grain size, sedimentary structures, and biogenic content (Fig. 4.2).

Accommodating a relaxed range for the core descriptions with similar characteristics is necessary due to the non-entire consistent naming schemes, logging details, and descriptive terms in different sites.

4.2.4 Statistical analyses

To comprehensively demonstrate the temporal-spatial differences of event bed frequency and thickness, different statistical charts and tests of subsets informed by geological history are provided.

Box-and-whisker plots (Fig. 4.4) summarize the characteristics and dispersion of the event bed thicknesses in each subset at a glance. Scatter plots with marginal histograms (Fig. 4.5) illustrate the variations in event frequency and thickness through different sub-intervals. Histograms allow the thorough thickness distributions in each geological period.

Event bed thicknesses are tested against some common distribution models (e.g., log-normal and exponential) by means of the Kolmogorov-Smirnov test (Fig. 4.6), one of the most widely used goodness-of-fit tests for non-normal distributions (Davis, 1986). Although resolving complex patterns is beyond the scope of this work, such analysis help to ensure whether a uniform and consistent parametric model could be applied to the volcanic settings. The gradient (β) of the complementary cumulative distribution functions (CCDFs) for the thick-bedded part (>30cm) could also provide insights into the relative importance of large and small turbidite beds.

T-tests were used to examine whether sediment records under the distinct geological influences show significantly different thickness means by accounting for the variability and size of samples (Fig. 4.7). The age-established subsets allow the sediment records formed by distinct governing processes to be compared. Among different t-tests, Welch's t-test is particularly suited for comparing differences between two independent groups, while the independent two-sample t-test could be more appropriate if the variances between two samples are equal. If the p-value returned by the test is lower than the significance level ($\alpha < 0.05$), the null hypothesis ($\mu_1 = \mu_2$) is rejected, indicating that the two distributions are not the same. T-test does not directly assess the similarity of the distribution shapes, so a combination of statistical charts (e.g., histograms) is still required to justify the comparability between datasets.

Lastly, the frequency analysis of event occurrences during the volcano active periods is presented. Event timings were interpolated linearly within constrained dates, with uncertainties mostly ranging from a few hundred to several thousand years

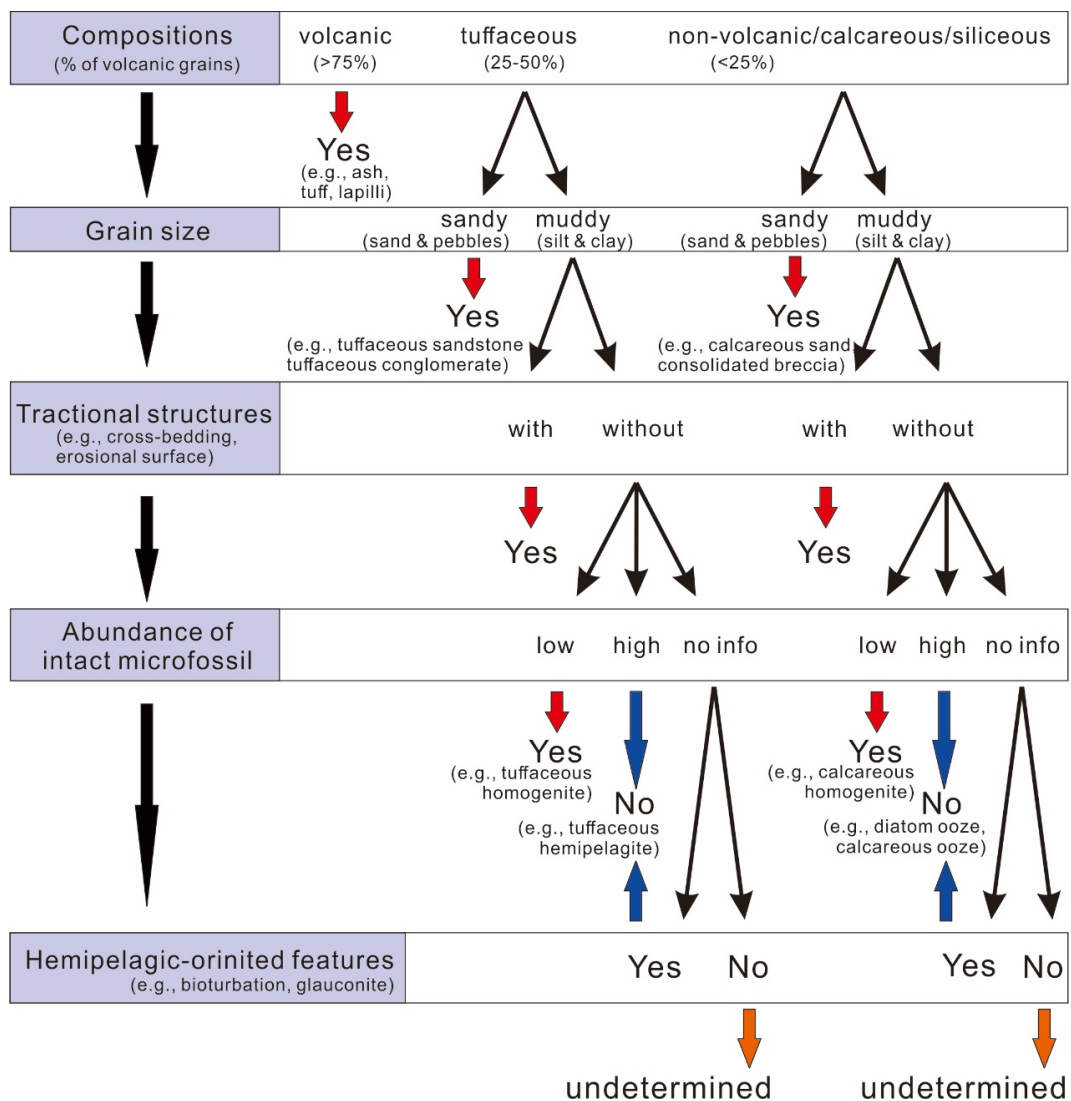


Figure 4.3: The workflow of event bed discrimination. Event beds are separated from hemipelagite in five steps (purple rectangles). Red, blue, and orange arrows represent interpretations of event beds, hemipelagic beds, and undetermined beds, respectively.

(Fig. 4.8). The power spectra of the event occurrence data were computed to detect significant periodic components (Fig. 4.9). The derived periods were compared with the frequencies simulated by 10,000 Poisson processes, which assumed complete independence of individual events (Fig. 4.10). Periods were considered relevant if the magnitude of their corresponding frequency component exceeded those obtained from Poisson process simulations. These analyses were performed using the methods implemented in `PointProcessTools.jl`, and a more detailed explanation can be found in Kling et al. (2024).

4.3 Results

4.3.1 Logistics of data set grouping

Datasets have been subdivided based on different geological and non-geological concerns. In the following, the grouping logistics and the encompassing intervals are described.

a. Montserrat (Site U1394): This data set was divided into glacial and interglacial periods over the last 300 kyr.

b. Izu Arc (Sites U1436 and U1437): The front and rear Izu Arcs were divided into four groups of subsets based on different considerations:

(b-1) The first follows the exact logistics as did for the Montserrat group, though the whole timespan is 1 Ma.

(b-2) The second aims to compare four subsets from the two sides of the arc (U1436 and U1437) at the same geological stage (0-0.9 Ma). Each subset spans ≈ 0.5 Myr.

(b-3) The third aims to compare six subsets from the rear Izu Arc (Site U1437) at the geological stage under similar geological influences (0-8.75 Ma). Each subset spans ≈ 1.5 Myr.

(b-4) The fourth aims to test the sensitivity of the t-test analysis by dividing the 1.5 Myr interval in the third group into 0.5 Myr intervals by also excluding those with low validity rates of sediment records.

c. Kyushu-Palau Ridge (Site U1438): This data set was divided into six subsets based on the volcanic evolution stages, as suggested by Maffione and Morris (2022). Each stage spans 4-6 Myr, except for the latest stage. The stages are:

1. 44.5-48.7 Ma: Pre-arc diffuse volcanism
2. 40.2-44.5 Ma: Early arc volcanism

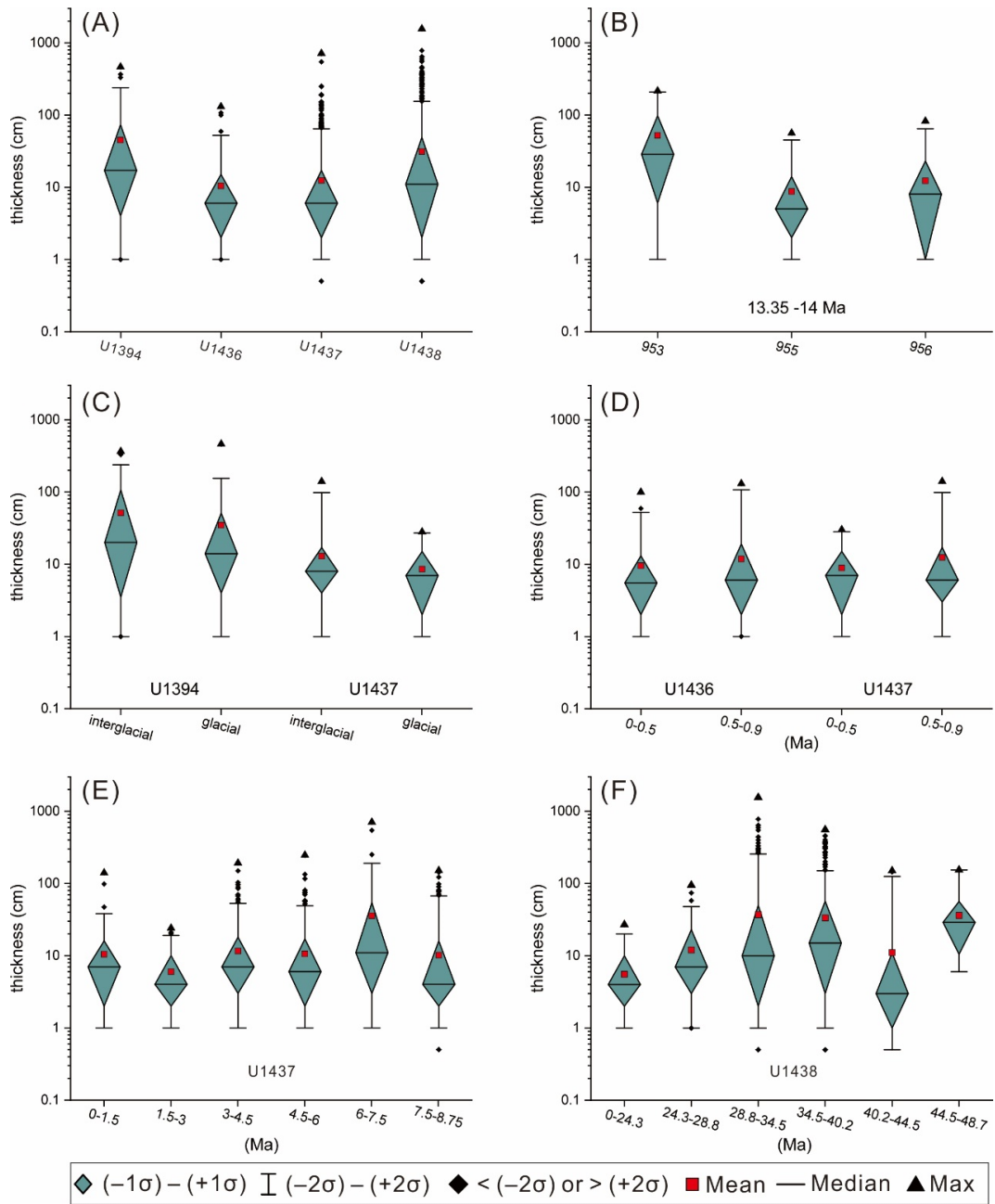


Figure 4.4: Box-and-whisker plots of event bed thicknesses for (a) Sites U1394, U1436, U1437 and U1438; (b) Sites 955A, 956B and 953C (13.35–14 Ma); (c) Sites U1394 and U1437 (selected glacial and interglacial intervals), (d) Sites U1436 and U1437 (0 to 0.9 Ma only); (e) Site U1437 (Six subsets within 8.75 Ma); (f) Site U1438 (Six subsets within 48.7 Ma). Note that vertical axes are logarithmic.

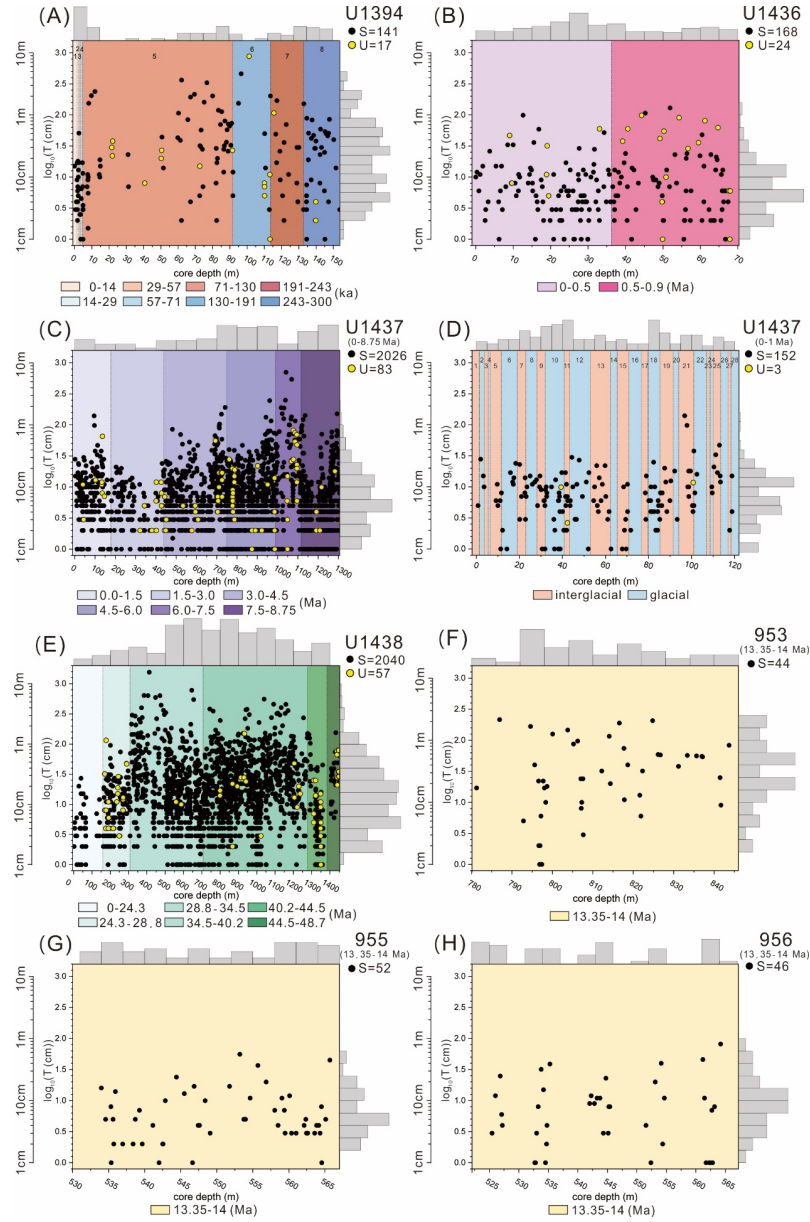


Figure 4.5: All event beds data for Sites (a) U1394, 1164 (b) U1436, (c) U1437 (0–8.75 Ma), (d) U1437 (0–1 Ma), (e) U1438, (f) 953C, (g) 955A, and (h) 956B. Colored blocks separate the designated sub-intervals. Black dots represent the core depths and thicknesses of the interpreted event beds extracted using the discrimination process (Fig. 4.3). Yellow dots are event beds unselected due to severe drilling disturbance. In (a) and (d), warm and cold coloured blocks represent interglacial and glacial stages, respectively (numbers near tops of the columns are the marine isotope stages). The counts of selected (S) and unselected (U) event beds are shown at the upper right. Marginal histograms show the relative frequencies of the counts (top) and the thickness (right) for individual sites. Note that the vertical axes are logarithmic. No data on drilling disturbance were provided by Schindlbeck et al. (2018a), so points in (f) to (h) are all treated as selected.

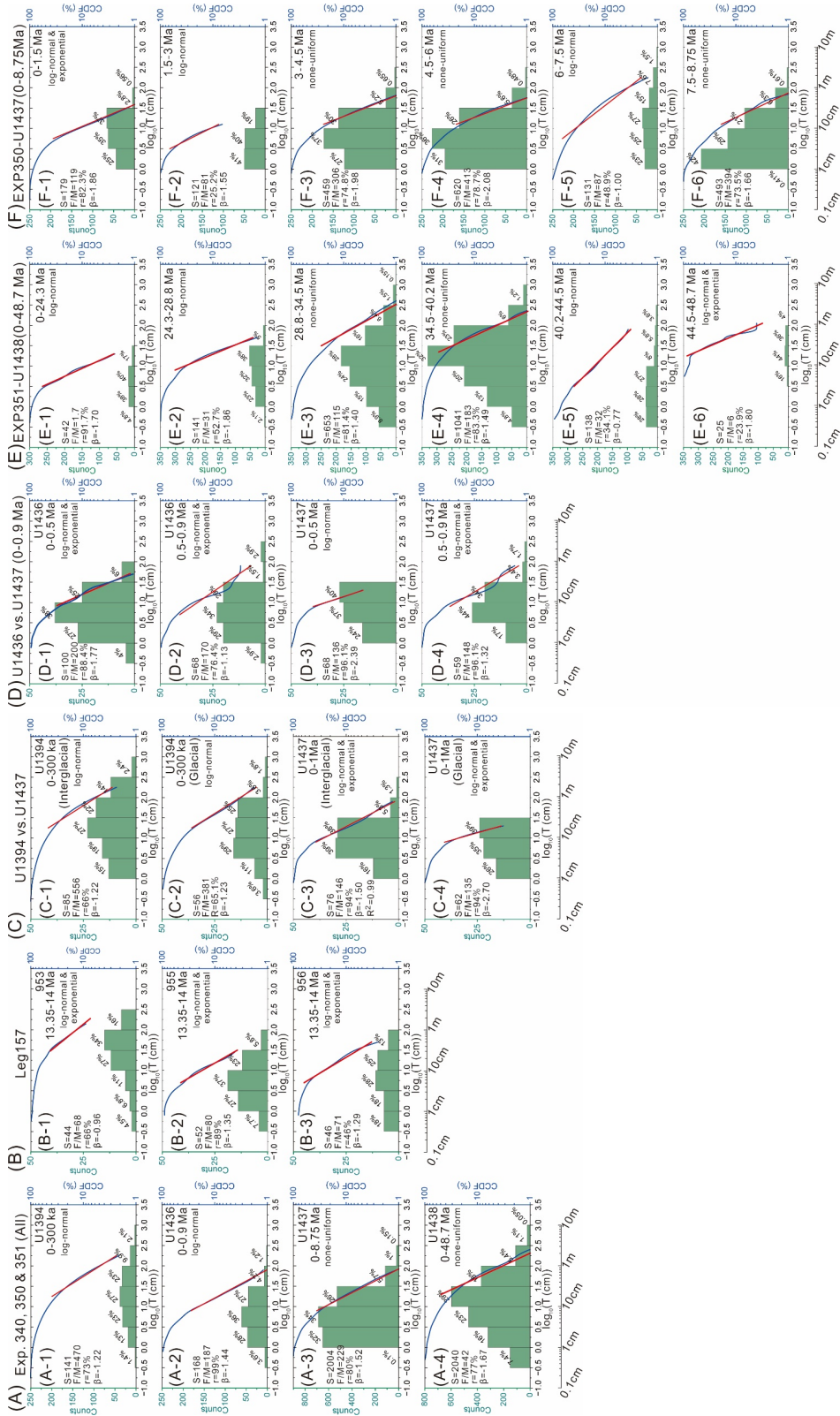


Figure 4.6: Histograms (green bars) and complementary cumulative distribution functions (CCDFs, blue curves) of the thicknesses of event beds in the studied intervals for Sites (a) U1398, U1436, U1437 and U1438; (b) 953, 955 and 956 (13.35 and 14 Ma); (c) U1394 (0–300 ka) and U1437 (0–1 Ma) (d) U1436 and U1437 (0–0.9 Ma); (e) U1437 (0–8.75 Ma); (f) U1438 (0–8.75 Ma). Red straight lines present regressions fitted by least squares through the frequencies of the thicker beds (i.e., the fourth quarter of the event inventory). Values on the left sides are counts of selected event beds (S), frequency of event per kilo year (f/k), the validity rates of sediment records (r), and the distribution gradient (β) of the regression line. Note that, in each panel, both axes are logarithmic and text in upper-right represents the best model for the distribution.

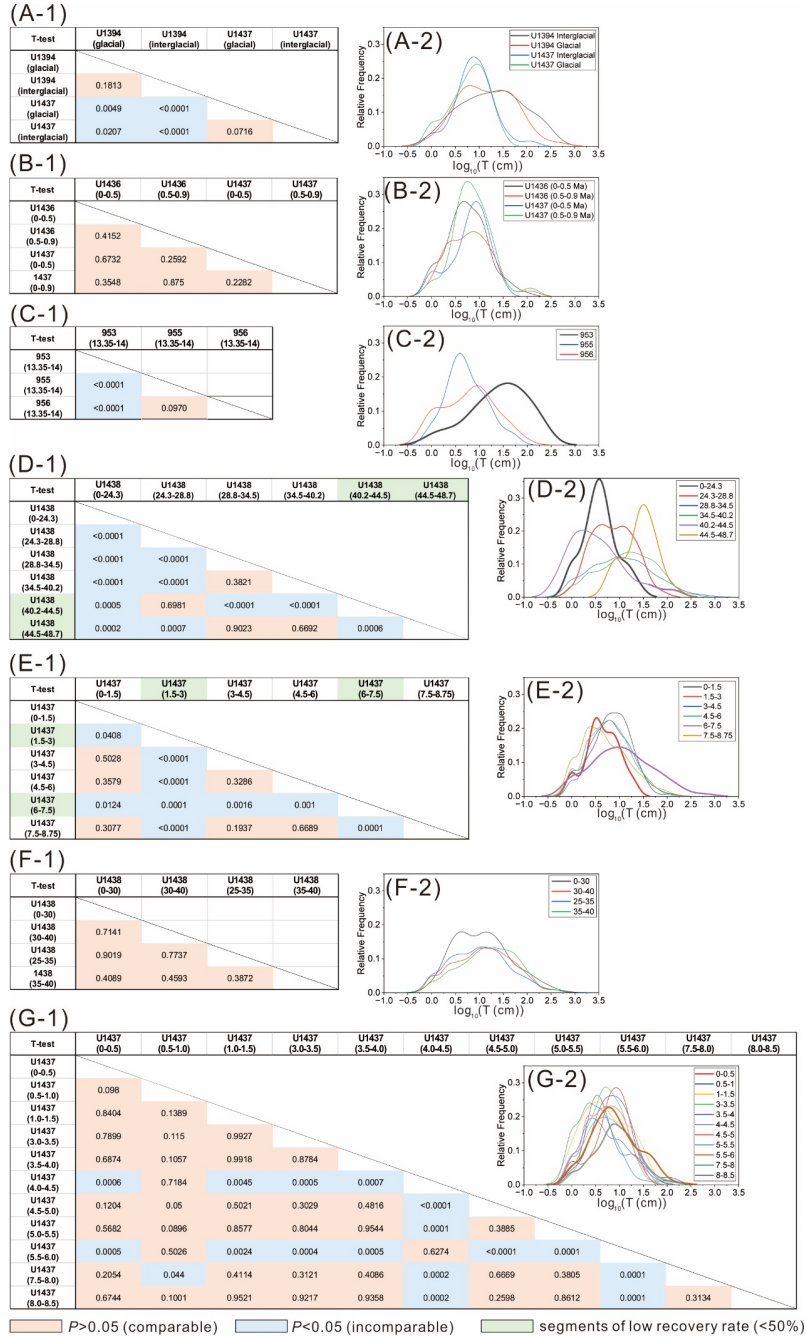


Figure 4.7: Student T-test results and frequency distribution curves corresponding with the graphs in Fig. 4.6. Light orange and light blue cells indicate that the two subsets are comparable or incomparable, respectively. Green cells represent segments with low valid rates of sediment records. The frequency distribution curves of the incomparable subsets are thickened for emphasis. (f) The segments with low validity rates of sediment records in (1.5–3 and 6–7.5 Ma) are excluded from the T-test.

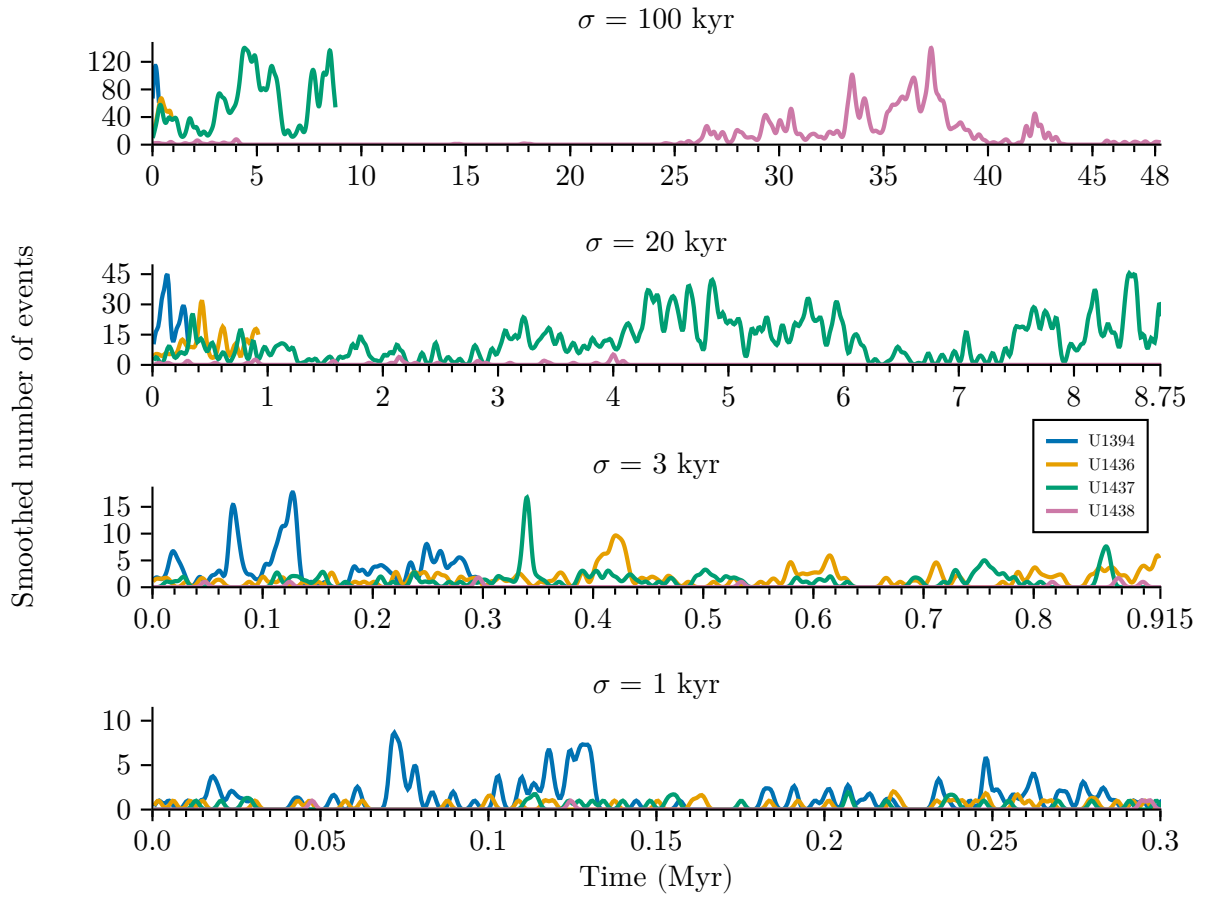


Figure 4.8: Chronostratigraphies of event frequencies. Event counts have been smoothed with a normalized Gaussian kernel (values of the variance σ specified at the top of each plot) to improve visual impression of bed emplacement episodicity for (a) 0-0.3 Ma, (b) 0-9 Ma (c) 0-8.75 Ma and (d) 0-48.7 Ma.

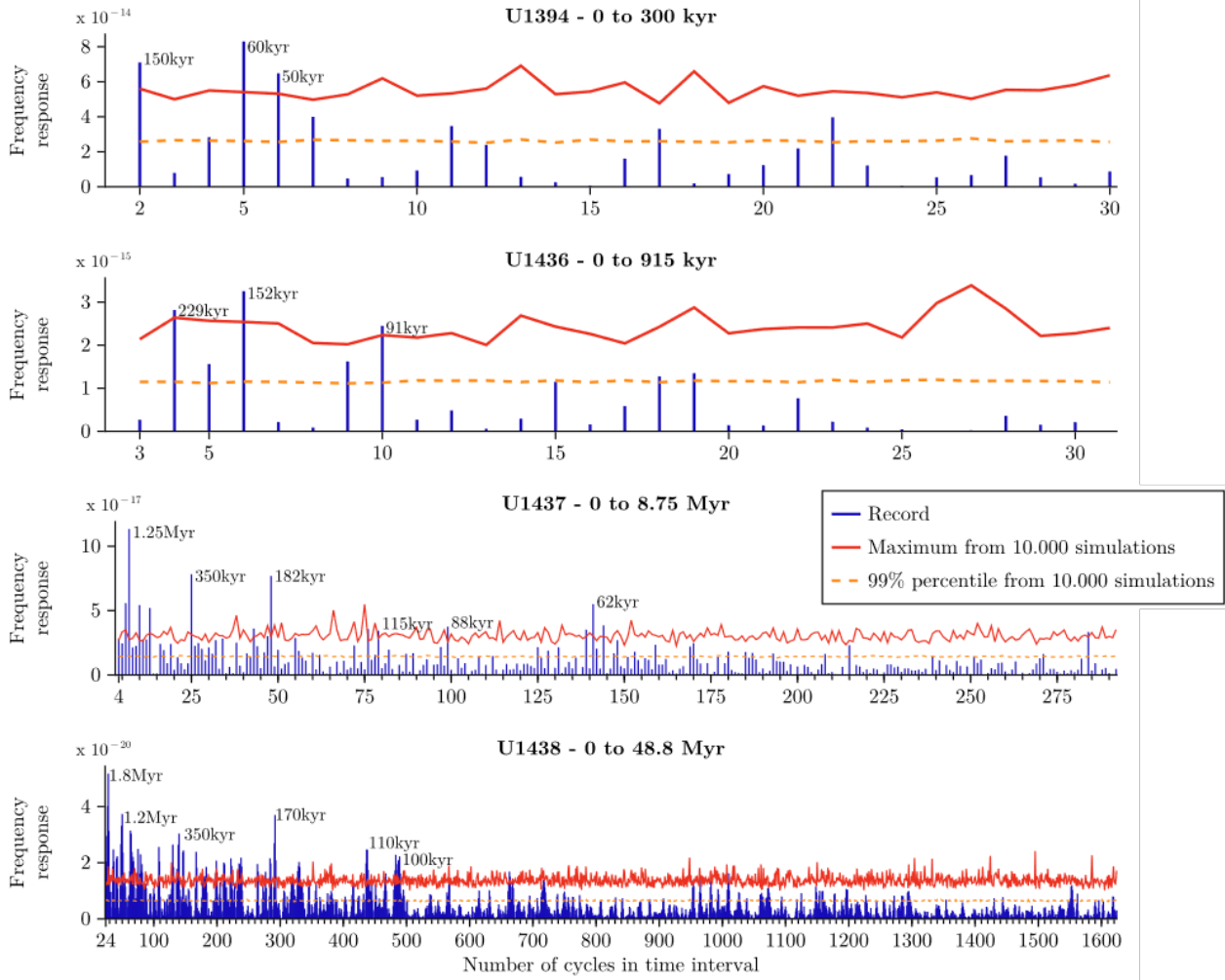


Figure 4.9: Power spectra for preserved geological periods. Blue bars represent the frequency content of raw datasets. Periodicities corresponding to a specific component can be calculated as the total length of the interval (specified in the titles) divided number of cycles in the time interval (x-axis). Red curves represent the maximum values after 10,000 simulations of Poisson processes. (a) Montserrat, (b) the front Izu Arc (c) the rear Izu Arc (d) Kyushu-Palau Ridge.

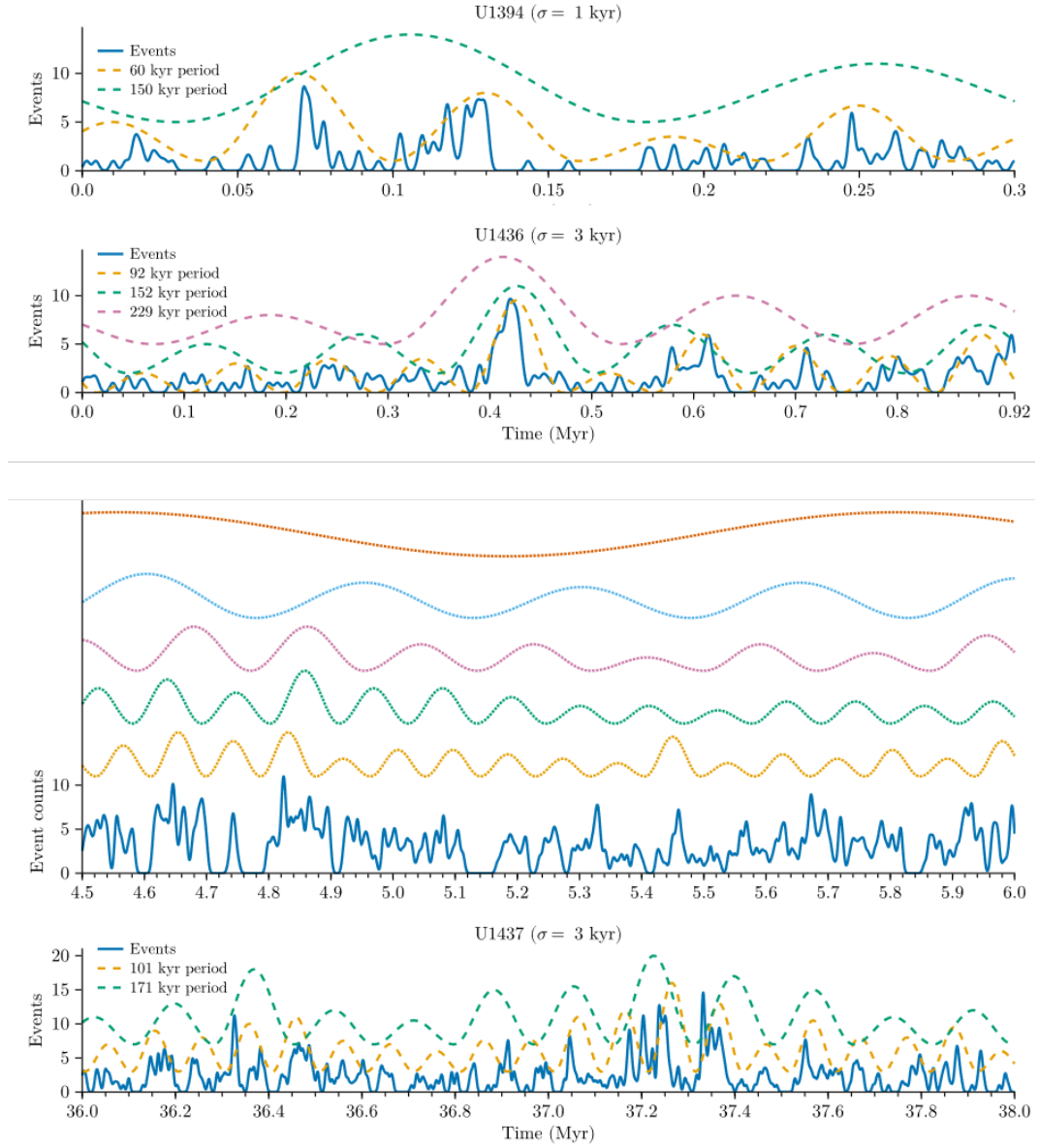


Figure 4.10: Smoothed event occurrences aligned with model periodic cycles derived from Fig 4.9. The phases of the periodic components were calculated with amplitudes change for visualization improvement. (a) Montserrat, 0–0.3 Ma, (b) The front Izu Arc, 0–9 Ma (c) the rear Izu Arc, 4.5–6 Ma and (d) Kyushu-Palau Ridge, 34.5–40.2 Ma. Intervals of (c) and (d) are confined for better visualization.

3. 34.4-40.2 Ma: First two episodes of arc development
4. 28.8-34.5 Ma: Last two episodes of arc development
5. 24.2-28.8 Ma: Arc rifting and demise
6. 0-24 Ma: Back-arc seafloor spreading

d. Gran Canaria (Sites 953, 955, and 956): Three sites are located on the north (956) and south (953 and 955) of the island, where submarine canyon systems only developed on the north of the island.

4.3.2 Box-and-whisker plot

Montserrat and Kyushu-Palau Ridge have broader thickness ranges and higher proportions of thick beds (>30 cm) than the Izu Arc datasets (Fig. 4.4A). The south of Gran Canaria has narrower thickness ranges and a lower portion of the thick beds than the north. Although similar thickness ranges are found between the two sites in the south, the southwestern site has a greater proportion of thin beds (Fig. 4.4B). Offshore Montserrat has all measurements higher than the rear Izu Arc in both glacial and interglacial periods. Both interglacial periods obtain higher proportions of thick beds than the glacial periods (Fig. 4.4C). Although the measurements of the 0.5-0.9 Ma subsets in the front and rear Izu Arc are slightly higher than 0-0.5 Ma subsets, their thickness distributions within 16%-84% are similar (Fig. 4.4D). The rear Izu Arc subsets are similar except for 1.5-3 Ma and 6-7.5 Ma subsets. The 1.5-3 Ma subset exhibits the narrowest thickness range and lowest portion of thick beds, while the 6-7.5 Ma shows the opposite (Fig. 4.4E). Subsets of Kyushu-Palau Ridge exhibit diverse thickness distributions (Fig. 4.4F). The 44.5-48.7 Ma subset has the highest mean and median but a narrow range. The 40.2-44.5 Ma subset has the lowest mean and median, but the thickness range is broad. The 28.8-34.5 Ma and 34.5-40.2 Ma subsets have measurements similar to and larger than the other four. Very thick event beds (>1m) are also commonly identified. Thickness values and distributions gradually become smaller and narrower for the two subsets after 28.8 Ma (i.e., 24.3-28.8 and 0-24.3 Ma).

4.3.3 Scatter plots with marginal histograms

A total of 4698 event beds were derived, including 4517 selected event beds and 181 beds deselected from the severely disturbed beds (Fig. 4.5). The unselected event beds should not largely interfere with the frequency probabilities across different

subintervals because of their low percentages (i.e., 2-14 %) and relatively random spread.

A total of 141 selected beds were identified in Montserrat for the last 300 ka. The probability of event frequencies has been higher since 71 ka, but most of them are thin beds in contrast to the stages before 71 ka (Fig. 4.5A). A total of 168 selected beds were identified in the front Izu Arc over the last 0.9 Ma (Fig. 4.5B). Frequency variations are mild along the depth and slightly peak at the depth of 25-30 m. A total of 2026 selected beds were identified in the rear Izu Arc for the last 48.7 Ma (Fig. 4.5C). Event frequencies appear low at 1.5-3 Ma and 6-7.5 Ma, but bed thicknesses are greatly thinner at 1.5-3 Ma than at 6-7.5 Ma. Though the event frequencies are different in the other four subsets, their thickness distributions appear to be similar. A total of 152 selected beds were identified in the rear Izu Arc within 0-1 Ma (Fig. 4.5D). The event frequencies are high around the stages of MIS 10-11 (374-425ka) and MIS 18-19 (760-790ka). Very few thick beds are found. A total of 2040 selected beds were identified in Kyushu-Palau Ridge for the last 48.7 Ma. Event frequencies have gradually increased from 48.7 to 28.8 Ma, with cyclicities of frequency changes in between (Fig. 4.5E). Frequencies have subsequently dropped toward the present. Thick beds mostly occur during the frequency increasing periods. A total of 52, 46 and 44 beds were identified in different sites around Gran Canaria within 13.35-14 Ma (Fig. 4.5F to h). Event frequencies of the three sites all appear to fluctuate along the core depth, though the beds in Site 953 are much thicker than Sites 953 and 955.

4.3.4 Thickness-frequency distributions

Thickness-frequency distributions demonstrated counts and percentages in different thickness intervals (Fig. 4.6). The event frequency per kilo years (f/k), the validity rates of sediment records (r), the curve of complementary cumulative distribution function (CCDF), and the gradient (β) of the regression line, and parametric distribution-fitting results were also displayed in the panels.

Thicknesses between 1 and 30 cm are most common in all subsets, except the site in northern Gran Canaria (953), where 30-100 cm beds are dominant. The highest f/k (0.47) and gentle β (from -1 to -1.35) of Montserrat indicate more frequent and higher proportions of thicker beds than the rear Izu Arc and Kyushu Palau Ridge (Fig. 4.6A). The similar f/k but flat β (> -1) of the north of Gran Canaria represent similar event frequencies but a higher percentage of thick beds than the other two in the south during the same geological stage (Fig. 4.6B). The differences in f/k and β between interglacial and glacial stages from the same sites are mild. The

differences are high between Montserrat and the rear Izu Arc (Fig. 4.6C). The f/k of the front Izu Arc subsets are slightly higher (0.02-0.05) than those in the rear arc. The values of β are all steeper in the subsets of 0-0.5 Ma, meaning fewer proportions of thick beds (Fig. 4.6D). The variations of f/k reflected the evolution history of the Kyushu-Palau Ridge (Fig. 4.6E). The f/k increased from the magmatism initiation (48.7 Ma), experienced a rapid rise during the arc growth (28.8-40.2 Ma) and then followed by a sharp decrease after arc demise and rifting (0-28.8 Ma). The high f/k (>0.1) and moderate β for the two arc growth stages are similar but distinct from the other substages (f/k : 0.03-0.002). The low r for the stages 40.2-44.5 Ma and 44.5-48.7 Ma could undermine the representative of the results. Stages of 0-1.5, 3-4.5, 4.5-6 and 7.5-8.75 Ma of the rear Izu Arc all have steeper β (>1.65) and general high f/k (>0.1), though f/k of the 0-1.5 Ma is relatively low. In contrast, the two low r stages (1.5-3 and 6-7.5 Ma) show low f/k and gentler β than the other four stages (Fig. 4.6F).

Different parametric distribution models (log-normal, exponential, and power-law) were tested for different subsets. We conclude that no single distribution model fits all 27 subsets. Among them, ten subsets fit the log-normal model, another ten fit both log-normal and exponential models, and the remaining seven cannot fit any uniform distribution model.

4.3.5 T-test analysis

The similarity of distributions under different influential factors are examined by the t-tests (Fig. 4.7). Smoothing thickness distributions were also provided to visualize the probability spectrum of different thickness intervals.

Climate stages (Fig. 4.7A)

The glaciation and interglaciation subsets appear to have similar thickness distributions within the same settings (Montserrat or the rear Izu Arc) and cannot be differentiated by t-tests. The subsets between Montserrat and the rear Izu Arc are distinct even in the same climatic stage.

Tectonic locations (Fig. 4.7B)

The rear and the front of the Izu Arcs for the last 0.9 Ma cannot be differentiated by t-tests. The smoothed curves also show similar distribution ranges and probability

spectra, though the peak probability is slightly lower in the rear Izu Arc subset within 0.5-0.9 Ma.

Geomorphological “filter” (Fig. 4.7C)

T-tests differentiate the subset of the northern Gran Canaria from the two in the south, while two cannot be differentiated from each other. Smoothed distributions also show a wider range and thicker bed thickness for the northern site.

Volcano evolution stages (Fig. 4.7D)

The low p-values reflect the distinction between the seafloor spreading stage (0-24.3 Ma) and the other five stages. The two volcanic arc growth stages (28.8-34.5 Ma and 34.5-40.2 Ma) cannot be differentiated from each other by t-test but the other four stages. The low completeness of depositional records ($r < 35\%$) undermine the validity of t-test results between the waning (24.3-28.8 Ma) and waxing (40.2-44.5 Ma) volcanic stages. The same concerns also given to the subset of the earliest stage (44.5-48.7 Ma).

Subintervals undergo similar geological influences (Fig. 4.7E)

The 1.5-Myr subsets show similar thickness distributions and cannot be differentiated by the t-tests, except those with low completeness of records (1.5-3 and 6-7.5 Ma), showing different distribution coverage and the shapes.

Analyzed subset interval (Fig. 4.7F)

T-tests suggest nine out of eleven finer-interval subsets maintain high p-values instead of two subsets of 4-4.5 Ma and 5.5-6 Ma. Nonetheless, these two subsets obtain p-values >0.05 and cannot be differentiated by t-test.

4.3.6 Time-dependent frequency analysis

Chronostratigraphies of event frequencies were smoothed using Gaussian kernel bandwidths of 1, 3, 20, and 100 kyrs, tailored to the respective temporal resolutions (Fig. 4.8). In sites with depositional records spanning millions of years, small crenulate cycles were observed superimposed on broader basal sinuous curves (e.g., the rear Izu Arc and Kyushu-Palau Ridge). Poisson-process simulations resolved the periods of event occurrence rates, revealing periodic intervals across the studied

settings (Fig. 4.9). Periods of 150-180 kyr were identified in all four settings, while periods of 88-110 kyr were found on Kyushu-Palau Ridge and both sides of the Izu Arc and. Additionally, 350 kyr and 1.2 Myr periods were detected in the rear Izu Arc and Kyushu-Palau Ridge. The modeled periodic cycles aligned well with the smoothed curves of event occurrences (Fig. 4.10).

4.4 Discussion

4.4.1 Factors that can modify thickness-frequency distributions

Thickness-frequency distributions could be affected by various factors. Understanding their effects is crucial for determining the dominant influences in the studied areas. This section aims to compile and discuss the impacts of these factors (Table 4.2).

Allochthonous ash beds

Depositional basins can sometimes transported from distal areas. Theoretically, such allochthonous ash beds should be excluded while assessing the characteristics of the studied areas using thickness distribution. Although event beds from both near and far-field sources were included in this study, a unique data set of volcanic glass composition from the rear Izu Arc over the last 2.7 Ma (King, 2021; Schindlbeck et al., 2018a) allows the effects of the allochthonous sources to be briefly discussed.

In the last 2.7 Ma, only 7% (22 out of 300) of tephra beds in the rear Izu Arc were geochemically determined to originate from the distal southwestern Japan arc. These beds are mostly < 5 cm, except one with 22 cm. T-tests cannot differentiate the datasets that include and exclude these beds (data not shown). The involvement of far-field ashes should slightly increase the event frequency and mildly upward bend the thin-bedded part of cumulative distributions but still retain the original characteristics (Table 4.2). Nevertheless, the allochthonous contribution is perhaps more important in areas or stages where no governing local process generates event beds (e.g., Kyushu-Palau Ridge after 24.3 Ma).

Measurement noise

Measurement noise arises from ambiguous boundaries due to bioturbation, indistinct lithostratigraphic changes, inability to distinguish thin turbidites, or lateral variability in bed thickness (e.g., Freundt et al., 2021; Mahony et al., 2014). Carlson and

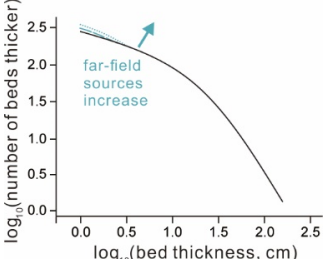
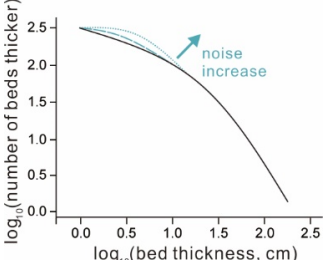
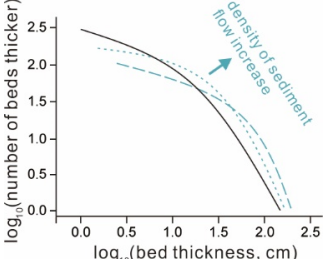
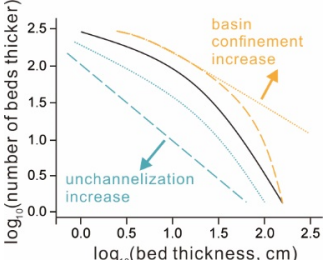
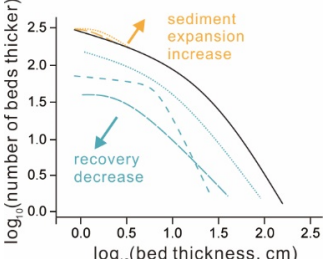
Factors	Details	Event count changes	Thickness variations / bed	Anticipated effect on distribution	Influence level
Allochthonous source	Far-field ash transported by air or current	Mildly increase	Usually <10 cm, occasionally >20 cm		Generally low
Measurement noise	Ambiguous or obscured boundary due to bioturbation, inability to distinguish thin turbidites from each other	None to medium decrease	Generally <10 cm		Usually low, but could be medium in distal areas
Sedimentary flow processes	Sediment flow properties (grain size and concentration) and dynamics (amalgamation, erosion, bypass, ponding)	Mild to medium decrease	A few cm to tens of cm, sometimes > 1 m		Medium
Geomorphological "filter"	Effect of seabed geometry on sediment flows (e.g., channelization, basin confinement, slope gradient)	Mild to severely decrease	A few cm to several m		Medium - high
Drilling procedures	Proportion of sediment records intact, associated with incomplete core recovery, drilling disturbance, flow-in, and expansion	None to severely decrease	A few mm to tens of cm, sometimes some m		low - high

Table 4.2: Factors that could adjust the thickness-frequency distribution.

Grotzinger (2001) simulated this influence by adding a Gaussian thickness distribution with zero mean and specified different standard deviations. Their simulations demonstrated that the measurement noise slightly upward bent the thin-bedded part (<20 cm) and mildly increased the standard deviation with no change in the event frequency (Table 4.2).

Sedimentary flow properties

Different depositional processes could also be due to the changes in rheological properties of sediment flows (Talling, 2001) dependent on grain parameters (size, density, and shape) and sediment flow concentrations (e.g., Jeong, 2010; Sadler, 1982; Talling, 2001). Although concurrent changes also play a role, turbidite thickness was found to be positively correlated with basal grain size (Lowe, 1982). The rapid inertial settling in coarse grained divisions of high-density sediment intends to form thick beds rather than the viscous settling observed in fine-grained divisions of low-density sediment flows (Lowe, 1982; Sadler, 1982).

Geomorphological “filters”

Geomorphological "filters" reflect the effect of seabed geometry on sediment flows. Thin and fine-grained turbidites preferably deposits where sediment flows are diluted and depleted due to progressive dissipation and sorting after long transportation (Walker, 1967), such as offshore and deep-water unchanneled environments (e.g., Hodgson et al., 2006; Hsiung et al., 2023). They can also be formed close to the source areas where a portion of sediment flows has been fractionated and deposited on relatively high or distal places, such as overbank spillage on the channel levee (e.g., Hansen et al., 2015; Kane et al., 2010) and the sediment suspension on the fringe of submarine lobes (e.g., Flint et al., 2011; Pr  lat and Hodgson, 2013).

Simulation of cumulative distributions from the upper to lower submarine suggested the decrease of event frequency and the proportion changes in different thickness intervals (Carlson and Grotzinger, 2001). Geometry and confinement of depositional basins were also found to impact the preservation of bed thickness (Malinverno, 1997; Marini et al., 2016; Sinclair and Cowie, 2003). Sinclair and Cowie (2003) suggested that a confined and unfilled basin tends to trap incoming sediment flow, resulting in ponded and thick beds. Conversely, basins with reduced confining barriers enhance the stripping and bypassing of sediment flows, preventing thick turbidite deposited in the basin (Table 4.2).

Modifications of sedimentary flow processes (e.g., amalgamation, erosion, bypass, ponding) are also interdependent on seabed geometry. Thickness and frequency of event beds mildly decrease if the erosion and sediment bypass are weak. Intense erosion can remove intra-turbidite muds and turbidites below (e.g., Casciano et al., 2018) but may encourage bed amalgamation, resulting in an increase in thick beds but a decrease in thin beds. For instance, bed amalgamations are commonly found in settings with frequent occurrence of intense sediment flows at channels (Macauley and Hubbard, 2013) and rapid deposition due to abrupt sediment flow deceleration at the base of the slope (García, 1993; Lee et al., 2002). Field-data-tied simulations for an active submarine fan system (Carlson and Grotzinger, 2001) agree with this inference (4.2).

Drilling procedures

Drilling procedures can significantly destroy and obscure sediment beds due to core damage and fluid circulation (e.g., Yang et al., 2019), undermining event bed recognition and measurement. Fluid-circulation-induced sediment loss preferably occurs in permeable coarse grained beds, potentially affecting the thick-bedded end. Sediment flow-in creates thick artificial beds, but they can be differentiated by their thick, structureless, and homogeneous features. The effects of drilling procedures could be mild or drastic, so the influence on the distribution changes could be diverse and less predictable. Though sediment cores suffering from severe drilling disturbances and sediment loss might still provide some primary characteristics, we do not recommend directly using them.

4.4.2 Implications of the t-test analysis

It was examined whether t-tests (Fig. 4.7) combined with thickness-frequency distribution features (Figs. 4.5 and 4.6) can reflect the distinct geological and non-geological factors behind the compared subsets. Schematic models were summarized in Fig. 4.11.

Climate changes

The undifferentiated thickness distributions and high p-values (Figs. 4.7A and 4.11A) suggest that the generation mechanism of event beds during glacial and interglacial periods could be similar, though the intensity could be strong during the interglacial stages considering the slightly higher event bed frequencies (Fig. 4.6C).

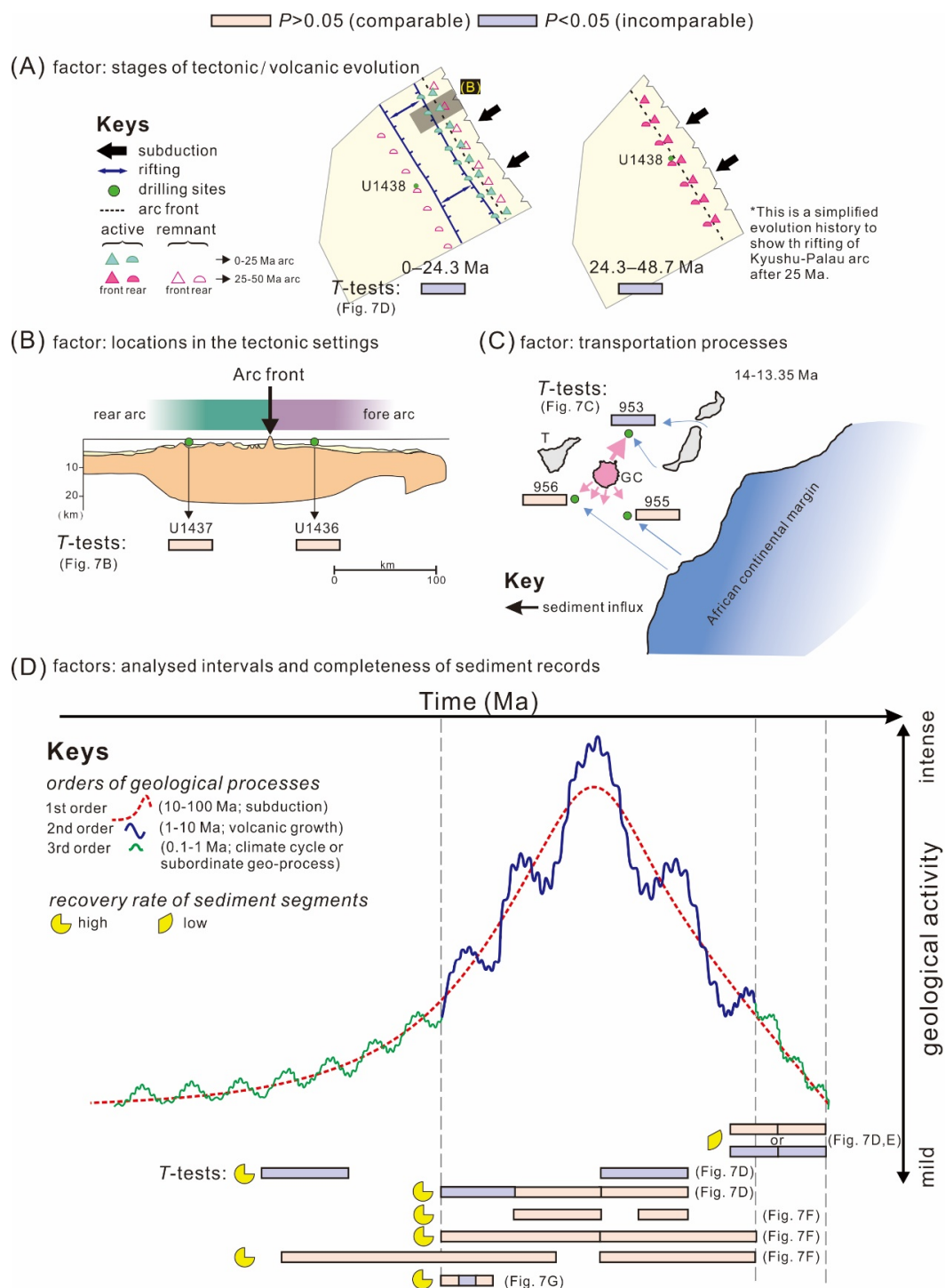


Figure 4.11: Summary of two-sample t-test analysis results and factors (a-c) interpreted to explain the associations.

Tectonic locations

The inseparable depositional records between the front and the rear Izu Arc for the last 0.9 Ma (Figs. 4.7B and 4.11B) could be attributed to the development of the extensional zone since the last 3 Ma. Contributions from the extensional zone after 3 Ma mingle the previous distinct sediment and chemical compositions deposited in the two arc sides (Hochstaedter et al., 2001). The higher event frequency in the front arc (Fig. 4.6D) likely inherit from its more explosive nature, attributed to higher water content and the volatile-rich composition of the subducting slab. These differences were probably more pronounced earlier than 3 Ma, when the sources of volcanoclastic bed arcs were not intermixed.

Geomorphological “filter”

Discrimination was found between the site in the north of Gran Canaria and the sites in the south during the same volcanic stage when Gran Canaria was actively growing (Figs. 4.7C and 4.11C). The similar event frequency reflects the same source area. However, twice thicker sediments (Figs. 4.6B and 4.7C) can be explained by the more efficient sediment channelization through submarine canyons in the north (Paris, 2002).

Volcano evolution stages

The incompatibility between the Kyushu-Palau Ridge subsets of 28.8-40.2 Ma and the subset of 0-24.3 Ma likely results from much fewer events (Figs. 4.7D and 4.11A), low thickness means and the lack of thick event beds during the volcano inactive stage (Figs. 4.6E-1 and 4.6E-2). These differences conform to the distinct geological scenes between the active and inactive volcanic stages. Conversely, the comparability between the subsets 28.8-34.5 Ma and 34.5-40.2 Ma complies with our expectations of similar event frequency and distribution patterns during the same volcanic arc development stages.

Completeness of sediment records

Subsets with poor sediment preservation (green cells in Fig. 4.7) are mostly distinct from those with good preservation due to the destruction and obscuration of sediment beds, resulting in unrepresentative and biased thickness distributions. For example, the subset with 23.9% r from the Kyushu-Palau Ridge only has 25 events recovered and shows a drastic downturn in the CCDF (Fig. 4.6E). Therefore, results

often cannot be justified by the characteristics of thickness distributions and the corresponding influential factors. Based on the datasets used in this study, a 65% validity rate should be able to establish reliable thickness distribution characteristics.

Analyzed subset interval

Nine out of eleven 0.5-Myr subsets from the rear Izu arc maintain high p-values after subdivided from the 1.5-Myr subsets (Fig. 4.7F), suggesting a generally similar depositional record within the same geological stages. Indeed, the narrower analyzed interval may allow the effects of short-term processes to suppress the long-term process, resulting in the differentiation between the subsets. For instance, the appearance of lapilli-stone beds at 4.3-4.4 Ma was explained as a temporary active volcanic stage (Tamura et al., 2015), increasing the thickness mean in the 4-4.5 Ma subset.

Our analyses suggest that an appropriate analysis interval is needed to encompass the characteristics of the testing processes that govern the depositional records.

4.4.3 Alternative interpretations for differences in thickness-frequency distributions

Variations in thickness-frequency distributions preserve the information about the changing factors that sediment flows have experienced (e.g., Pantopoulos et al., 2013; Talling, 2001). Previous studies usually focused on the effects of spatial differences due to limited record timespans. These comparisons often based on simplifying initial conditions to power-law inputs (e.g., Carlson and Grotzinger, 2001; Sinclair and Cowie, 2003) or resulting conditions to log-normal outputs (Drummond and Wilkinson, 1996; Murray et al., 1996). Such assumptions implicitly suggest that sediment flow generation and emplacement mechanisms at the source and depositional areas remain unchanged over time and space. This raises the question of whether sediment flow inputs can vary across different geological stages.

The data set of the Kyushu-Palau Ridge, with its ≈ 50 Myr evolution history, provides a unique opportunity to explore these questions. Our analyses indicate that two volcanic active stages (i.e., 28.8-34.5 Ma and 34.5-40.2 Ma) cannot be differentiated. However, they are distinct from the volcanic demise and seafloor spreading stages (i.e., 0-24.3 Ma and 24.3-28.8 Ma) regarding event frequency, proportions of thick beds, and thickness distribution. Given the nearly constant distance to the source areas and the similar deep-sea floor environment, the effects of transportation distances and seabed geometry on distribution modification should be constant.

Therefore, the observed distribution variations can be attributed to the volcanic evolution from active to inactive stages. This likely involves weakening contributions from pyroclastic flows, decreasing discharged volumes and coarse-grained sediment flows, and lengthening recurrence intervals. Such evolving processes of sediment flow generation, transitioning from primarily volcanic activity to other non-volcanic processes, have been observed in other volcanic settings (e.g., Chang et al., 2022; Corry-Saavedra et al., 2019; Mosher et al., 2004; Mulder et al., 2003; Porcile et al., 2020). Although no simple parametric model can describe the thickness distribution during volcanic growth stages, sediment flow generation characteristics vary over time were concluded. Any simplified assumptions of initial input and resulting output should be justified by reliable reasons.

4.4.4 Periods of event frequency

Time-dependent frequency analyses indicate the presence of kyr- and Myr-scale cyclicities within the datasets during active volcano stages. Hence, the identified event periodicities should preserve the effects of different driving forces acting on the response to volcanic activity. This section focuses on the periods that appear consistently across multiple sites, as these are more likely to be driven by broader-scale processes.

Kilo-year periods (Milankovitch cycles)

The 100-kyr short-term periodicity of Earth's eccentricity has been recognized in the rear Izu Arc (U1437) over the last 1.1 Ma, using detailed tephra and $\delta^{18}\text{O}$ records (Schindlbeck et al., 2018b). This study extended this observation by identifying periods close to 100 kyr across the Izu Arc and Kyushu-Palau Ridge (Fig. 4.9) but in much longer depositional records (Fig. 4.8). These cycles are considered to be related to eccentricity periods. The slight deviations from 100 kyr potentially arise from dating uncertainties and the linear age-depth model, as age uncertainties usually increase for older samples due to poor and low preservation of dating material. Another possibility is that the volcanic responses to the eccentricity effects occur over a relatively broad interval rather than being confined to a narrow range, a similar finding shown in the multi-taper spectral analysis by Schindlbeck et al. (2018a) (see Fig. 4 therein).

The discovery of the 150-180 kyr event periods at all sites is likely related to the 173-kyr cycle of Earth-Saturn obliquity (e.g., Boulila et al., 2018; Charbonnier et al., 2018; Zhang et al., 2022), which are modulated by gravitational interactions. Such

cycles have been identified in middle Eocene carbonate-rich sequences from the North Atlantic Southeast Newfoundland Ridge Boulila et al. (2018) and in an eolian red clay sequence in the eastern Chinese Loess Plateau from the Late Miocene to Pliocene (Zhang et al., 2022). If the correlation is valid, our datasets could be the first to identify such Earth-Saturn cycle using volcanic ash records.

The 350-kyr periods observed in the rear Izu Arc and Kyushu-Palau Ridge may result from the 405-kyr long eccentricity cycles, given that this is the only well-established mechanism of this age scale. However, the larger time difference is challenging to explain solely by age uncertainties, which typically account for variations of a few to ten thousand years. This discrepancy suggests that additional volcanic or tectonic cycles might also be involved with the 350-kyr periods, necessitating a more comprehensive understanding of the geological history.

Our analysis suggests that the duration of volcanic responses to orbital cycles tens of millions of years ago could be similar to those of the present (i.e., 100-, 173-, and 405-kyr cycles), though the mechanisms and impacts may differ. Typically, climate cycles are extensively documented within the Quaternary period (e.g., Lattaud et al., 2019; Nádor et al., 2003; Shackleton et al., 1984), with some studies extending these cycles beyond the Quaternary (e.g., Caballero-Gill et al., 2019; Herbert et al., 2010; Lisiecki and Raymo, 2005). The limitations in extending these records are due to the decreasing availability and resolution of climate proxies over extended timespans (Lisiecki and Raymo, 2005), non-linear responses to orbital forcing (e.g., Tziperman et al., 2006), and shifts in dominant climate cycles (e.g., Mid-Pleistocene Transition; Medina-Elizalde and Lea (2005)). Addressing these questions will require further studies utilizing similarly extensive climate proxy records and advanced Earth systems modeling.

Million-year periods

The superimposition of Myr orbital cycles on shorter-period orbital cycles within extensive depositional records has been previously documented (e.g., van Dam et al., 2006), supporting our findings. Notably, the 1.2-Myr cyclicities identified in the Kyushu-Palau Ridge and the rear Izu Arc coincide with the interval of Earth-Mars obliquity modulation cycles (Qin et al., 2022; van Dam et al., 2006). These Earth-Mars obliquity cycles have been traced back to 50 Ma (Crampton et al., 2018; Hinnov, 2000; Laskar et al., 2004; Pälike et al., 2004), corresponding to the timespan of our study. However, the reasons for why long-term orbital cycles might produce more prominent periodic signals compared to shorter-term cycles remain unclear.

Further investigations to understand the underlying mechanisms are needed, if the correlation is valid.

Another possibility of this Myr-cycle is perhaps associated with recurring high-volume magmatic events occurring in subduction zones (e.g., Ducea et al., 2015). Several mechanisms have been proposed to explain such periodic magmatic flare-ups, including retro-arc or trench thickening (Ducea and Barton, 2007), steepening of the subduction slab (e.g., Ferrari et al., 2007), and repeated magmatic underplating (Dufek and Bergantz, 2005). The repeated magmatic underplating for explaining the observed Myr cycles are favored for two reasons. First, the required interval for this mechanism (<5 Myr) closely matches our findings, unlike the other two tectonic processes, which typically span tens of millions of years. Second, the repeated intrusion of hot, low-velocity mantle fingers within the mantle wedge (Tamura, 2003) could resolve the origin of replenish underplated and pre-existing crustal materials, driving frequent volcanic activity at the surface. Further studies should investigate whether such million-year periods also occur in other oceanic island arcs.

4.5 Conclusions

In this study, over 4,500 event beds were analyzed, spanning the last 50 Myr of deposition from seven scientific drilling sites near Montserrat, the Izu Arc, the Kyushu-Palau Ridge, and Gran Canaria. These datasets were divided into groups based on distinct factors to discuss the effects of climate, tectonic, seabed geometry, volcano evolution, completeness of sediment records and analyzed intervals. Subsets were characterized using Box-and-Whisker plots, scatter plots with marginal histograms, and thickness-frequency distributions to understand the impacts of different factors. The dissimilarity between the compared subsets was determined by t-test, and the periods of event frequencies were assessed by frequency analysis.

The factors include:

1. Climate Stage: Event frequencies of Montserrat and the rear Izu Arc subsets were slightly lower during glacial stages than interglacial stages (0.1-0.01 event/ky). The thickness probability distributions and mean values between the two climate stages did not significantly differ, as indicated by a t-test.

2. Tectonic Location: Event frequency was slightly higher in the front Izu Arc compared to the rear Izu Arc (0.02-0.06 event/ky). Other statistical characteristics did not significantly different, which was unexpected. The inseparability is attributed to the studied age when sediments greatly sourcing from the same extensional zone in the middle of the arc sides.

3. Seabed geometry: Event frequencies at sites around Gran Canaria were almost the same because sediments sourced from the same island. However, probability of thick beds and dispersion range are significantly higher in the northern site and are distinguishable by the t-test. The thicker beds were originating from the submarine canyons developed, enhancing the transportation efficacy.

4. Volcano evolution stage: Even frequencies, thickness dispersion ranges and probabilities of thick beds in the two volcano growth stages of the Kyushu-Palau Ridge are similarly high but significantly different from its demise and spreading stage, as also indicated by t-tests.

5. Non-geological factors: Incomplete sediment records could cause unusually low event frequency and non-systematic modifications on the thickness distributions, leading inconsistent t-test results between subsets. Statistical characteristics of the subsets with different analyzed intervals from the same governed processes mostly remain similar, though temporally processes more likely to become evident and be differentiated by t-test for subsets with finer intervals.

Frequency analysis identifies Milankovitch cyclicities across the studied regions. The 173 kyr Earth-Saturn obliquity cycle was observed in all sites. The 100-kyr and 405-kyr Earth orbital cycles were consistently found in the Izu Arc and Kyushu-Palau Ridge, extending from the past 1 million years to tens of millions of years. Additionally, 1.2 Myr cycles in these regions may be linked to deeper Earth magmatic processes or the obliquity of Earth and Mars.

This study confirms that thickness-frequency distribution analyses combined with t-tests help discriminate depositional records affected by distinct geological processes. Time-dependent frequency analysis helps uncover the climate and crustal-scale geological cycles in event thickness-frequency records. The proposed examination methods are likely also broadly applicable to other kinds of data that requires source areas and mechanisms discrimination.

References

Lesser Antilles Volcanism and Landslides: Implications for hazard assessment and long-term magmatic evolution of the arc. Integrated Ocean Drilling Program, June 2012. doi: 10.2204/iodp.pr.340.2012.

John Aitchison and James A. C. Brown. *The lognormal distribution*. Number 5. Cambridge Univ. Press, 1981. ISBN 0521040116.

F. Anguita and F. Hernán. The canary islands origin: a unifying model. *Journal of*

Volcanology and Geothermal Research, 103(1-4):1–26, December 2000. ISSN 0377-0273. doi: 10.1016/s0377-0273(00)00195-5.

Richard J. Arculus, Osamu Ishizuka, Kara A. Bogus, Michael Gurnis, Rosemary Hickey-Vargas, Mohammed H. Aljahdali, Alexandre N. Bandini-Maeder, Andrew P. Barth, Philipp A. Brandl, Laureen Drab, Rodrigo do Monte Guerra, Morihisa Hamada, Fuqing Jiang, Kyoko Kanayama, Sev Kender, Yuki Kusano, He Li, Lorne C. Loudin, Marco Maffione, Kathleen M. Marsaglia, Anders McCarthy, Sebastián Meffre, Antony Morris, Martin Neuhaus, Ivan P. Savov, Clara Sena, Frank J. Tepley III, Cees van der Land, Gene M. Yogodzinski, and Zhaohui Zhang. A record of spontaneous subduction initiation in the Izu-Bonin-Mariana arc. *Nature Geoscience*, 8(9):728–733, August 2015. ISSN 1752-0908. doi: 10.1038/ngeo2515.

P. D. Beattie and W. B. Dade. Is scaling in turbidite deposition consistent with forcing by earthquakes? *Journal of Sedimentary Research*, 66(5):909–915, 09 1996. ISSN 1527-1404. doi: 10.1306/D4268437-2B26-11D7-8648000102C1865D. URL <https://doi.org/10.1306/D4268437-2B26-11D7-8648000102C1865D>.

A. Berger. Milankovitch theory and climate. *Reviews of Geophysics*, 26(4):624–657, November 1988. ISSN 1944-9208. doi: 10.1029/rg026i004p00624.

W. H. Berger and G. R. Heath. Vertical mixing in pelagic sediments. *Journal of Marine Research*, 23, 1968.

Slah Boulila, Maximilian Vahlenkamp, David De Vleeschouwer, Jacques Laskar, Yuhji Yamamoto, Heiko Pälike, Sandra Kirtland Turner, Philip F. Sexton, Thomas Westerhold, and Ursula Röhl. Towards a robust and consistent middle eocene astronomical timescale. *Earth and Planetary Science Letters*, 486:94–107, March 2018. ISSN 0012-821X. doi: 10.1016/j.epsl.2018.01.003.

R. P. Caballero-Gill, T. D. Herbert, and H. J. Dowsett. 100-kyr paced climate change in the Pliocene warm period, southwest Pacific. *Paleoceanography and Paleoclimatology*, 34(4):524–545, April 2019. ISSN 2572-4525. doi: 10.1029/2018pa003496.

J. Carlson and J. P. Grotzinger. Submarine fan environment inferred from turbidite thickness distributions. *Sedimentology*, 48(6):1331–1351, December 2001. ISSN 1365-3091. doi: 10.1046/j.1365-3091.2001.00426.x.

- Claudio I. Casciano, Marco Patacci, Sergio G. Longhitano, Marcello Tropeano, William D. McCaffrey, and Claudio Di Celma. Multi-scale analysis of a migrating submarine channel system in a tectonically-confined basin: The miocene gorgoglione flysch formation, southern italy. *Sedimentology*, 66(1):205–240, July 2018. ISSN 1365-3091. doi: 10.1111/sed.12490.
- Yu-Chun Chang, Neil C. Mitchell, Thor H. Hansteen, Julie C. Schindlbeck-Belo, and Armin Freundt. Volcaniclastic deposits and sedimentation processes around volcanic ocean islands: the central azores. *Geological Society, London, Special Publications*, 520(1):523–546, November 2021a. ISSN 2041-4927. doi: 10.1144/sp520-2021-62.
- Yu-Chun Chang, Neil C. Mitchell, and Rui Quartau. Landslides in the upper submarine slopes of volcanic islands: The central azores. *Geochemistry, Geophysics, Geosystems*, 22(10), September 2021b. ISSN 1525-2027. doi: 10.1029/2021gc009833.
- Yu-Chun Chang, Neil Mitchell, Rui Quartau, Christian Hübscher, Liliana Rusu, and Fernando Tempera. Asymmetric abundances of submarine sediment waves around the azores volcanic islands. *Marine Geology*, 449:106837, July 2022. ISSN 0025-3227. doi: 10.1016/j.margeo.2022.106837.
- Yu-Chun Chang, Neil C. Mitchell, Julie C. Schindlbeck-Belo, Thor H. Hansteen, Armin Freundt, Christian Hübscher, and Rui Quartau. Emplacement history of volcaniclastic turbidites around the central azores volcanic islands: Frequencies of slope landslides and eruptions. *Geosphere*, 19(3):654–675, March 2023. ISSN 1553-040X. doi: 10.1130/ges02570.1.
- Guillaume Charbonnier, Slah Boulila, Jorge E. Spangenberg, Thierry Adatte, Karl B. Föllmi, and Jacques Laskar. Obliquity pacing of the hydrological cycle during the oceanic anoxic event 2. *Earth and Planetary Science Letters*, 499:266–277, October 2018. ISSN 0012-821X. doi: 10.1016/j.epsl.2018.07.029.
- C. Chen and R. N. Hiscott. Statistical analysis of facies clustering in submarine-fan turbidite successions. *Journal of Sedimentary Research*, 69(2):505–517, March 1999. ISSN 1527-1404. doi: 10.2110/jsr.69.505.
- P. D. Cole, J. E. Guest, A. M. Duncan, and J. M. Pacheco. Capelinhos 1957-1958, faial, azores: deposits formed by an emergent surtseyan eruption. *Bulletin of Volcanology*, 63(2-3):204–220, June 2001. ISSN 1432-0819. doi: 10.1007/s004450100136.

Kate Corry-Saavedra, Julie C. Schindlbeck, Susanne M. Straub, Masafumi Murayama, Louise L. Bolge, Arturo Gómez-Tuena, Yoshitaka Hashimoto, and Jon D. Woodhead. The role of dispersed ash in orbital-scale time-series studies of explosive arc volcanism: insights from iodp hole u1437b, northwest pacific ocean. *International Geology Review*, 61(17):2164–2183, March 2019. ISSN 1938-2839. doi: 10.1080/00206814.2019.1584770.

Maya Coussens, Deborah Wall-Palmer, Peter. J. Talling, Sebastian. F. L. Watt, Michael Cassidy, Martin Jutzeler, Michael A. Clare, James. E. Hunt, Michael Manga, Thomas. M. Gernon, Martin. R. Palmer, Stuart. J. Hatter, Georges Boudon, Daisuke Endo, Akihiko Fujinawa, Robert Hatfield, Matthew. J. Hornbach, Osamu Ishizuka, Kyoko Kataoka, Anne Le Friant, Fukashi Maeno, Molly McCanta, and Adam. J. Stinton. The relationship between eruptive activity, flank collapse, and sea level at volcanic islands: A long-term ≥ 1 ma record offshore montserrat, lesser antilles. *Geochemistry, Geophysics, Geosystems*, 17(7):2591–2611, July 2016. ISSN 1525-2027. doi: 10.1002/2015gc006053.

James S. Crampton, Stephen R. Meyers, Roger A. Cooper, Peter M. Sadler, Michael Foote, and David Harte. Pacing of paleozoic macroevolutionary rates by milankovitch grand cycles. *Proceedings of the National Academy of Sciences*, 115(22):5686–5691, May 2018. ISSN 1091-6490. doi: 10.1073/pnas.1714342115.

John C. Davis. *Statistics and data analysis in geology*. Wiley, New York; NY [u.a.], 2. ed. edition, 1986. ISBN 0471080799. Literaturangaben.

Carl N. Drummond and Bruce H. Wilkinson. Stratal thickness frequencies and the prevalence of orderedness in stratigraphic sequences. *The Journal of Geology*, 104(1):1–18, 1996. doi: 10.1086/629798. URL <https://doi.org/10.1086/629798>.

M. N. Ducea, S. R. Paterson, and P. G. DeCelles. High-volume magmatic events in subduction systems. *Elements*, 11(2):99–104, March 2015. ISSN 1811-5217. doi: 10.2113/gselements.11.2.99.

Mihai N. Ducea and Mark D. Barton. Igniting flare-up events in cordilleran arcs. *Geology*, 35(11):1047, 2007. ISSN 0091-7613. doi: 10.1130/g23898a.1.

J. Dufek and G. W. Bergantz. Lower crustal magma genesis and preservation: a stochastic framework for the evaluation of basalt-crust interaction. *Journal of Petrology*, 46(11):2167–2195, June 2005. ISSN 0022-3530. doi: 10.1093/petrology/egi049.

Luca Ferrari, Martín Valencia-Moreno, and Scott Bryan. *Magmatism and tectonics of the Sierra Madre Occidental and its relation with the evolution of the western margin of North America*. Geological Society of America, 2007. ISBN 9780813724225. doi: 10.1130/2007.2422(01).

S.S. Flint, D.M. Hodgson, A.R. Sprague, R.L. Brunt, W.C. Van der Merwe, J. Figueiredo, A. Prélat, D. Box, C. Di Celma, and J.P. Kavanagh. Depositional architecture and sequence stratigraphy of the karoo basin floor to shelf edge succession, laingsburg depocentre, south africa. *Marine and Petroleum Geology*, 28(3): 658–674, March 2011. ISSN 0264-8172. doi: 10.1016/j.marpetgeo.2010.06.008.

Armin Freundt, Julie C. Schindlbeck-Belo, Steffen Kutterolf, and Jenni L. Hopkins. Tephra layers in the marine environment: a review of properties and emplacement processes. *Geological Society, London, Special Publications*, 520(1):595–637, December 2021. ISSN 2041-4927. doi: 10.1144/sp520-2021-50.

Kantaro Fujioka, Toshiya Kanamatsu, Ai Sasaki, Yasuhiko Ohara, Izumi Sakamoto, Satoru Haraguchi, and Teruaki Ishii. Morphology and geology of extinct spreading center in the philippine sea plate-results of the yokosuka y96-11 cruise. *JAMSTEC Journal of Deep Sea Research*, (13):155–194, 1997. ISSN 13407848.

Marcelo H. García. Hydraulic jumps in sediment-driven bottom currents. *Journal of Hydraulic Engineering*, 119(10):1094–1117, October 1993. ISSN 1943-7900. doi: 10.1061/(asce)0733-9429(1993)119:10(1094).

Michael O. Garcia. Turbidites from slope failure on hawaiian volcanoes. *Geological Society, London, Special Publications*, 110(1):281–294, January 1996. ISSN 2041-4927. doi: 10.1144/gsl.sp.1996.110.01.22.

J. B. Gill, E. M. Bongiolo, T. Miyazaki, C. Hamelin, M. Jutzeler, S. DeBari, A-S. Jonas, B. S. Vaglarov, L. S. Nascimento, and M. Yakavonis. Tuffaceous mud is a volumetrically important volcanoclastic facies of submarine arc volcanism and record of climate change. *Geochemistry, Geophysics, Geosystems*, 19(4): 1217–1243, April 2018. ISSN 1525-2027. doi: 10.1002/2017gc007300.

Agust Gudmundsson. Mechanical aspects of postglacial volcanism and tectonics of the reykjanes peninsula, southwest iceland. *Journal of Geophysical Research: Solid Earth*, 91(B12):12711–12721, November 1986. ISSN 0148-0227. doi: 10.1029/jb091ib12p12711.

- Larissa A.S. Hansen, Richard H.T. Callow, Ian A. Kane, Fabiano Gamberi, Marzia Rovere, Bryan T. Cronin, and Benjamin C. Kneller. Genesis and character of thin-bedded turbidites associated with submarine channels. *Marine and Petroleum Geology*, 67:852–879, November 2015. ISSN 0264-8172. doi: 10.1016/j.marpetgeo.2015.06.007.
- CL Harford, MS Pringle, RSJ Sparks, and SR Young. *The volcanic evolution of Montserrat using $^{40}\text{Ar}/^{39}\text{Ar}$ geochronology*, volume Memoir 21, pages 93 – 114. Geological Society of London, United Kingdom, 2002.
- Timothy D. Herbert, Laura Cleaveland Peterson, Kira T. Lawrence, and Zhonghui Liu. Tropical ocean temperatures over the past 3.5 million years. *Science*, 328 (5985):1530–1534, June 2010. ISSN 1095-9203. doi: 10.1126/science.1185435.
- Linda A. Hinnov. New perspectives on orbitally forced stratigraphy. *Annual Review of Earth and Planetary Sciences*, 28(1):419–475, May 2000. ISSN 1545-4495. doi: 10.1146/annurev.earth.28.1.419.
- R.N. Hiscott, A. Colella, P. Pezard, M.A. Lovell, and A. Malinverno. *Sedimentology of Deep-Water Volcaniclastics, Oligocene Izu-Bonin Forearc Basin, Based on Formation MicroScanner Images*. Ocean Drilling Program, August 1992. doi: 10.2973/odp.proc.sr.126.118.1992.
- Alfred Hochstaedter, Jim Gill, Robert Peters, Phil Broughton, Pete Holden, and Brian Taylor. Across-arc geochemical trends in the izu-bonin arc: Contributions from the subducting slab. *Geochemistry, Geophysics, Geosystems*, 2(7), July 2001. ISSN 1525-2027. doi: 10.1029/2000gc000105.
- D. M. Hodgson, S. S. Flint, D. Hodgetts, N. J. Drinkwater, E. P. Johannessen, and S. M. Luthi. Stratigraphic evolution of fine-grained submarine fan systems, tanqua depocenter, karoo basin, south africa. *Journal of Sedimentary Research*, 76(1): 20–40, January 2006. ISSN 1527-1404. doi: 10.2110/jsr.2006.03.
- Kan-Hsi Hsiung, Toshiya Kanamatsu, Ken Ikehara, Masafumi Murayama, and Yuhji Yamamoto. Active sediment transport along trench axis: insights from x-ray fluorescence core scanning and magnetic analysis of marine sediments in the southwestern ryukyu trench. *Geoscience Letters*, 10(1), October 2023. ISSN 2196-4092. doi: 10.1186/s40562-023-00303-9.
- M. Sumita H.U. Schmincke. Volcanic evolution of gran canaria reconstructed from apron sediments; synthesis of vicap project drilling. In *Proceedings of the Ocean Drilling Program, Scientific Results 157*, 1998.

- James E. Hunt and Ian Jarvis. Prodigious submarine landslides during the inception and early growth of volcanic islands. *Nature Communications*, 8(1), December 2017. ISSN 2041-1723. doi: 10.1038/s41467-017-02100-3.
- James E. Hunt, Russell B. Wynn, P.J. Talling, and D.G. Masson. Frequency and timing of landslide-triggered turbidity currents within the agadir basin, offshore nw africa: Are there associations with climate change, sea level change and slope sedimentation rates? *Marine Geology*, 346:274–291, December 2013. ISSN 0025-3227. doi: 10.1016/j.margeo.2013.09.004.
- J.E. Hunt and I. Jarvis. The lifecycle of mid-ocean ridge seamounts and their prodigious flank collapses. *Earth and Planetary Science Letters*, 530:115867, January 2020. ISSN 0012-821X. doi: 10.1016/j.epsl.2019.115867.
- O Ishizuka, J Kimura, Y Li, R Stern, M Reagan, R Taylor, Y Ohara, S Bloomer, T Ishii, and U Hargroveiii. Early stages in the evolution of izu-bonin arc volcanism: New age, chemical, and isotopic constraints. *Earth and Planetary Science Letters*, 250(1-2):385–401, October 2006a. ISSN 0012-821X. doi: 10.1016/j.epsl.2006.08.007.
- Osamu Ishizuka, Kozo Uto, and Makoto Yuasa. Volcanic history of the back-arc region of the izu-bonin (ogasawara) arc. *Geological Society, London, Special Publications*, 219(1):187–205, January 2003. ISSN 2041-4927. doi: 10.1144/gsl.sp.2003.219.01.09.
- Osamu Ishizuka, Rex N. Taylor, J. Andy Milton, Robert W. Nesbitt, Makoto Yuasa, and Izumi Sakamoto. Variation in the mantle sources of the northern izu arc with time and space - constraints from high-precision pb isotopes. *Journal of Volcanology and Geothermal Research*, 156(3-4):266–290, September 2006b. ISSN 0377-0273. doi: 10.1016/j.jvolgeores.2006.03.005.
- Osamu Ishizuka, Rex N. Taylor, Makoto Yuasa, and Yasuhiko Ohara. Making and breaking an island arc: A new perspective from the oligocene kyushu-palau arc, philippine sea. *Geochemistry, Geophysics, Geosystems*, 12(5), May 2011. ISSN 1525-2027. doi: 10.1029/2010gc003440.
- Osamu Ishizuka, Rosemary Hickey-Vargas, Richard J. Arculus, Gene M. Yogodzinski, Ivan P. Savov, Yuki Kusano, Anders McCarthy, Philipp A. Brandl, and Masafumi Sudo. Age of izu-bonin-mariana arc basement. *Earth and Planetary Science Letters*, 481:80–90, January 2018. ISSN 0012-821X. doi: 10.1016/j.epsl.2017.10.023.

- A. Mark Jellinek, Michael Manga, and Martin O. Saar. Did melting glaciers cause volcanic eruptions in eastern california? probing the mechanics of dike formation. *Journal of Geophysical Research: Solid Earth*, 109(B9):n/a–n/a, sep 2004. doi: 10.1029/2004jb002978.
- Sueng Won Jeong. Grain size dependent rheology on the mobility of debris flows. *Geosciences Journal*, 14(4):359–369, December 2010. ISSN 1598-7477. doi: 10.1007/s12303-010-0036-y.
- Kyle Johnson, Kathleen M. Marsaglia, Philipp A. Brandl, Andrew P. Barth, Ryan Waldman, Osamu Ishizuka, Morihisa Hamada, Michael Gurnis, and Ian Ruttenberg. Intra-oceanic submarine arc evolution recorded in an 1-km-thick rear-arc succession of distal volcanoclastic lobe deposits. *Geosphere*, 17(4):957–980, May 2021. ISSN 1553-040X. doi: 10.1130/ges02321.1.
- M. Jull and D. McKenzie. The effect of deglaciation on mantle melting beneath iceland. *Journal of Geophysical Research: Solid Earth*, 101(B10):21815–21828, October 1996. ISSN 0148-0227. doi: 10.1029/96jb01308.
- Martin Jutzeler, James D. L. White, Peter J. Talling, Molly McCanta, Sally Morgan, Anne Le Friant, and Osamu Ishizuka. Coring disturbances in iodp piston cores with implications for offshore record of volcanic events and the missoula megafloods. *Geochemistry, Geophysics, Geosystems*, 15(9):3572–3590, September 2014. ISSN 1525-2027. doi: 10.1002/2014gc005447.
- I. A. Kane, W. D. McCaffrey, and J. Peakall. On the origin of paleocurrent complexity within deep marine channel levees. *Journal of Sedimentary Research*, 80(1):54–66, January 2010. ISSN 1527-1404. doi: 10.2110/jsr.2010.003.
- Cassandra King. Reidentifying sources of tephra in the izu-bonin arc: Recognizing recent rear-arc volcanism 1.1 - 2.7 ma, 2021.
- José Kling, Mathias Vetter, Julie Schindlbeck-Belo, Marion Jegen, and Steffen Kutterolf. Pointprocesstools.jl (software), 2024.
- J. Laskar, P. Robutel, F. Joutel, M. Gastineau, A. C. M. Correia, and B. Levrard. A long-term numerical solution for the insolation quantities of the earth. *Astronomy & Astrophysics*, 428(1):261–285, November 2004. ISSN 1432-0746. doi: 10.1051/0004-6361:20041335.
- Julie Lattaud, Li Lo, Christian Zeeden, Ya-Jun Liu, Sheng-Rong Song, Marcel T.J. van der Meer, Jaap S. Sinninghe Damsté, and Stefan Schouten. A multiproxy

- study of past environmental changes in the sea of okhotsk during the last 1.5 ma. *Organic Geochemistry*, 132:50–61, June 2019. ISSN 0146-6380. doi: 10.1016/j.orggeochem.2019.04.003.
- A. Le Friant, C.L. Harford, C. Deplus, G. Boudon, R.S.J. Sparks, R.A. Herd, and J.C. Komorowski. Geomorphological evolution of montserrat (west indies): importance of flank collapse and erosional processes. *Journal of the Geological Society*, 161(1):147–160, January 2004. ISSN 2041-479X. doi: 10.1144/0016-764903-017.
- E. Lebas, A. Le Friant, G. Boudon, S. F. L. Watt, P. J. Talling, N. Feuillet, C. Deplus, C. Berndt, and M. E. Vardy. Multiple widespread landslides during the long-term evolution of a volcanic island: Insights from high-resolution seismic data, montserrat, lesser antilles. *Geochemistry, Geophysics, Geosystems*, 12(5), May 2011. ISSN 1525-2027. doi: 10.1029/2010gc003451.
- Simon E Lee, Peter J Talling, Gerald G.J Ernst, and Andrew J Hogg. Occurrence and origin of submarine plunge pools at the base of the us continental slope. *Marine Geology*, 185(3-4):363–377, June 2002. ISSN 0025-3227. doi: 10.1016/S0025-3227(01)00298-5.
- Lorraine E. Lisiecki and Maureen E. Raymo. A pliocene-pleistocene stack of 57 globally distributed benthic $\delta^{18}O$ records. *Paleoceanography*, 20(1):n/a–n/a, jan 2005. doi: 10.1029/2004pa001071.
- Donald R. Lowe. Sediment gravity flows: Ii depositional models with special reference to the deposits of high-density turbidity currents. *SEPM Journal of Sedimentary Research*, Vol. 52, 1982. ISSN 1527-1404. doi: 10.1306/212f7f31-2b24-11d7-8648000102c1865d.
- Ryan V. Macauley and Stephen M. Hubbard. Slope channel sedimentary processes and stratigraphic stacking, cretaceous tres pasos formation slope system, chilean patagonia. *Marine and Petroleum Geology*, 41:146–162, March 2013. ISSN 0264-8172. doi: 10.1016/j.marpetgeo.2012.02.004.
- Marco Maffione and Antony Morris. Timing of tectonic and magmatic events in the philippine sea plate since 50 ma from high-resolution magnetostratigraphy of iodp site u1438. *Geochemistry, Geophysics, Geosystems*, 23(10), October 2022. ISSN 1525-2027. doi: 10.1029/2022gc010598.

- Sue H. Mahony, R.S.J. Sparks, and Nick H. Barnard. Quantifying uncertainties in marine volcanic ash layer records from ocean drilling cores. *Marine Geology*, 357: 218–224, November 2014. ISSN 0025-3227. doi: 10.1016/j.margeo.2014.08.010.
- Alberto Malinverno. On the power law size distribution of turbidite beds. *Basin Research*, 9(4):263–274, December 1997. ISSN 1365-2117. doi: 10.1046/j.1365-2117.1997.00044.x.
- Mattia Marini, Fabrizio Felletti, Salvatore Milli, and Marco Patacci. The thick-bedded tail of turbidite thickness distribution as a proxy for flow confinement: Examples from tertiary basins of central and northern apennines (italy). *Sedimentary Geology*, 341:96–118, July 2016. ISSN 0037-0738. doi: 10.1016/j.sedgeo.2016.05.006.
- D.G Masson, A.B Watts, M.J.R Gee, R Urgeles, N.C Mitchell, T.P Le Bas, and M Canals. Slope failures on the flanks of the western canary islands. *Earth-Science Reviews*, 57(1-2):1–35, January 2002. ISSN 0012-8252. doi: 10.1016/s0012-8252(01)00069-1.
- F. Mattern. Amalgamation surfaces, bed thicknesses, and dish structures in sand-rich submarine fans: numeric differences in channelized and unchannelized deposits and their diagnostic value. *Sedimentary Geology*, 150(3-4):203–228, July 2002. ISSN 0037-0738. doi: 10.1016/s0037-0738(01)00180-4.
- Martín Medina-Elizalde and David W. Lea. The mid-pleistocene transition in the tropical pacific. *Science*, 310(5750):1009–1012, November 2005. ISSN 1095-9203. doi: 10.1126/science.1115933.
- Sébastien Migeon, Thierry Mulder, Bruno Savoye, and Françoise Sage. Hydrodynamic processes, velocity structure and stratification in natural turbidity currents: Results inferred from field data in the var turbidite system. *Sedimentary Geology*, 245-246:48–62, March 2012. ISSN 0037-0738. doi: 10.1016/j.sedgeo.2011.12.007.
- S. Mizutani and I. Hattori. Stochastic analysis of bed-thickness distribution of sediments. *Journal of the International Association for Mathematical Geology*, 4 (2):123–146, June 1972. ISSN 1573-8868. doi: 10.1007/bf02080298.
- David C. Mosher, David J. W. Piper, D. Calvin Campbell, and Kimberley A. Jenner. Near-surface geology and sediment-failure geohazards of the central scotian slope. *AAPG Bulletin*, 88(6):703–723, June 2004. ISSN 0149-1423. doi: 10.1306/01260403084.

Thierry Mulder, James P.M. Syvitski, Sébastien Migeon, Jean-Claude Faugères, and Bruno Savoye. Marine hyperpycnal flows: initiation, behavior and related deposits. a review. *Marine and Petroleum Geology*, 20(6-8):861–882, June 2003. ISSN 0264-8172. doi: 10.1016/j.marpetgeo.2003.01.003.

C. J. Murray, D. R. Lowe, S. A. Graham, P. A. Martinez, J. Zeng, A. R. Carroll, R. Cox, M. Hendrix, C. Heubeck, D. Miller, I. W. Moxon, E. Sobel, J. Wendebourg, and T. Williams. Statistical analysis of bed-thickness patterns in a turbidite section from the great valley sequence, cache creek, northern california. *Journal of Sedimentary Research*, 66(5):900–908, September 1996. ISSN 1527-1404. doi: 10.2110/jsr.66.900.

David A. G. Nowell, M. Chris Jones, and David M. Pyle. Episodic quaternary volcanism in france and germany. *Journal of Quaternary Science*, 21(6):645–675, June 2006. ISSN 1099-1417. doi: 10.1002/jqs.1005.

Annamária Nádor, Miklós Lantos, Ágnes Tóth-Makk, and Edit Thamó-Bozsó. Milankovitch-scale multi-proxy records from fluvial sediments of the last 2.6ma, pannonian basin, hungary. *Quaternary Science Reviews*, 22(20):2157–2175, October 2003. ISSN 0277-3791. doi: 10.1016/s0277-3791(03)00134-3.

Heiko Pälike, Jacques Laskar, and Nicholas J. Shackleton. Geologic constraints on the chaotic diffusion of the solar system. *Geology*, 32(11):929, 2004. ISSN 0091-7613. doi: 10.1130/g20750.1.

G. Pantopoulos, B.C. Kneller, A.D. McArthur, S. Courivaud, A.E. Grings, and J. Kuchle. Turbidite bed thickness statistics of architectural elements in a deep-marine confined mini-basin setting: Examples from the grès d’annot formation, se france. *Marine and Petroleum Geology*, 95:16–29, August 2018. ISSN 0264-8172. doi: 10.1016/j.marpetgeo.2018.04.008.

George Pantopoulos, Ioannis Vakalas, Angelos Maravelis, and Avraam Zelilidis. Statistical analysis of turbidite bed thickness patterns from the alpine fold and thrust belt of western and southeastern greece. *Sedimentary Geology*, 294:37–57, August 2013. ISSN 0037-0738. doi: 10.1016/j.sedgeo.2013.05.007.

Raphael Paris. *Rythmes de construction et de destruction des édifices volcaniques de point chaud : l'exemple des Iles Canaries (Espagne)*. Theses, Université Panthéon-Sorbonne - Paris I, December 2002. URL <https://theses.hal.science/tel-00123713>.

F.A. Perret. *The Volcano-seismic Crises at Montserrat, 1933-1937*. Carnegie Institution Washington, DC: Carnegie Institution of Washington publication. Carnegie Institution of Washington, 1939. URL <https://books.google.de/books?id=6uQKAQAIAAJ>.

Adriano Pimentel, Stephen Self, José M. Pacheco, Adam J. Jeffery, and Ralf Ger-tisser. Eruption style, emplacement dynamics and geometry of peralkaline ignimbrites: Insights from the lajes-angra ignimbrite formation, terceira island, azores. *Frontiers in Earth Science*, 9, June 2021. ISSN 2296-6463. doi: 10.3389/feart.2021.673686.

Carlos Pirmez and Jasim Imran. Reconstruction of turbidity currents in amazon channel. *Marine and Petroleum Geology*, 20(6-8):823–849, June 2003. ISSN 0264-8172. doi: 10.1016/j.marpetgeo.2003.03.005.

Gaetano Porcile, Michele Bolla Pittaluga, Alessandro Frascati, and Octavio E. Sequeiros. Typhoon-induced megarips as triggers of turbidity currents offshore tropical river deltas. *Communications Earth & Environment*, 1(1), August 2020. ISSN 2662-4435. doi: 10.1038/s43247-020-0002-1.

Marta Prekopová and Juraj Janočko. Quantitative approach in environmental interpretations of deep-marine sediments (dukla unit, western carpathian flysch zone). *Geologica Carpathica*, 60(6):485–494, December 2009. ISSN 1335-0552. doi: 10.2478/v10096-009-0035-y.

Amandine Prélat and David M. Hodgson. The full range of turbidite bed thickness patterns in submarine lobes: controls and implications. *Journal of the Geological Society*, 170(1):209–214, January 2013. ISSN 2041-479X. doi: 10.1144/jgs2012-056.

Jie Qin, Rui Zhang, Vadim Kravchinsky, Jean-Pierre Valet, Leonardo Sagnotti, Jianxing Li, Yong Xu, Taslima Anwar, and Leping Yue. 1.2-million-year band of earth-mars obliquity modulation on the evolution of cold late miocene to warm early pliocene climate. *JGR solid Earth*, February 2022. doi: 10.1002/essoar.10510387.2.

X. Quidelleur, A. Hildenbrand, and A. Samper. Causal link between quaternary paleoclimatic changes and volcanic islands evolution. *Geophysical Research Letters*, 35(2), January 2008. ISSN 1944-8007. doi: 10.1029/2007gl031849.

Harriet Rawson, David M. Pyle, Tamsin A. Mather, Victoria C. Smith, Karen Fontijn, Stefan M. Lachowycz, and José A. Naranjo. The magmatic and eruptive response of arc volcanoes to deglaciation: Insights from southern chile. *Geology*, 44(4): 251–254, feb 2016. doi: 10.1130/g37504.1.

Sherman H. Bloomer Robert J. Stern. Subduction zone infancy: Examples from the eocene izu-bonin-mariana and jurassic california arcs. *GSA Bulletin*, 1992.

R. E. A. Robertson, W. P. Aspinall, R. A. Herd, G. E. Norton, R. S. J. Sparks, and S. R. Young. The 1995-1998 eruption of the soufrière hills volcano, montserrat, wi. *Philosophical Transactions of the Royal Society of London. Series A: Mathematical, Physical and Engineering Sciences*, 358(1770):1619–1637, May 2000. ISSN 1471-2962. doi: 10.1098/rsta.2000.0607.

William B. F. Ryan, Suzanne M. Carbotte, Justin O. Coplan, Suzanne O’Hara, Andrew Melkonian, Robert Arko, Rose Anne Weissel, Vicki Ferrini, Andrew Goodwillie, Frank Nitsche, Juliet Bonczkowski, and Richard Zemsky. Global multi-resolution topography synthesis. *Geochemistry, Geophysics, Geosystems*, 10(3), 2009. doi: <https://doi.org/10.1029/2008GC002332>. URL <https://agupubs.onlinelibrary.wiley.com/doi/abs/10.1029/2008GC002332>.

Peter M. Sadler. Bed-thickness and grain size of turbidites. *Sedimentology*, 29(1):37–51, February 1982. ISSN 1365-3091. doi: 10.1111/j.1365-3091.1982.tb01707.x.

Tomoki Sato, Takashi Miyazaki, Yoshihiko Tamura, James B. Gill, Martin Jutzeler, Ryoko Senda, and Jun-Ichi Kimura. The earliest stage of izu rear-arc volcanism revealed by drilling at site u1437, international ocean discovery program expedition 350. *Island Arc*, 29(1), January 2020. ISSN 1440-1738. doi: 10.1111/iar.12340.

Chris Satow, Agust Gudmundsson, Ralf Gertisser, Christopher Bronk Ramsey, Mohsen Bazargan, David M. Pyle, Sabine Wulf, Andrew J. Miles, and Mark Hardiman. Eruptive activity of the santorini volcano controlled by sea-level rise and fall. *Nature Geoscience*, 14(8):586–592, August 2021. ISSN 1752-0908. doi: 10.1038/s41561-021-00783-4.

J.C. Schindlbeck, S. Kutterolf, A. Freundt, R.P. Scudder, K.T. Pickering, and R.W. Murray. Emplacement processes of submarine volcanoclastic deposits (iodp site c0011, nankai trough). *Marine Geology*, 343:115–124, September 2013. ISSN 0025-3227. doi: 10.1016/j.margeo.2013.06.017.

- Julie C. Schindlbeck, Marion Jegen, Armin Freundt, Steffen Kutterolf, Susanne M. Straub, Maryline J. Mleneck-Vautravers, and Jerry F. McManus. 100 kyr cyclicity in volcanic ash emplacement: evidence from a 1.1 myr tephra record from the NW pacific. *Scientific Reports*, 8(1), mar 2018a. doi: 10.1038/s41598-018-22595-0.
- Julie Christin Schindlbeck, Steffen Kutterolf, Susanne M. Straub, Graham D. M. Andrews, Kuo-Lung Wang, and Maryline J. Mleneck-Vautravers. One million years tephra record at IODP sites u1436 and u1437: Insights into explosive volcanism from the japan and izu arcs. *Island Arc*, 27(3), feb 2018b. doi: 10.1111/iar.12244.
- H.-U. Schmincke and B. Segschneider. *Shallow submarine to emergent basaltic shield volcanism of Gran Canaria: evidence from drilling into the volcanic apron*. Ocean Drilling Program, June 1998. doi: 10.2973/odp.proc.sr.157.110.1998.
- H.-U. Schmincke and M. Sumita. *Tephra event stratigraphy and emplacement of volcanoclastic sediments, Mogán and Fataga stratigraphic intervals, Part II: origin and emplacement of volcanoclastic layers*. Ocean Drilling Program, June 1998. doi: 10.2973/odp.proc.sr.157.113.1998.
- Hans-Ulrich Schmincke. *The Geology of the Canary Islands*, pages 67–184. Springer Netherlands, 1976. ISBN 9789401015660. doi: 10.1007/978-94-010-1566-0_4.
- N. J. Shackleton, J. Backman, H. Zimmerman, D. V. Kent, M. A. Hall, D. G. Roberts, D. Schnitker, J. G. Baldauf, A. Desprairies, R. Homrighausen, P. Huddlestun, J. B. Keene, A. J. Kaltenback, K. A. O. Krumsiek, A. C. Morton, J. W. Murray, and J. Westberg-Smith. Oxygen isotope calibration of the onset of ice-rafting and history of glaciation in the north atlantic region. *Nature*, 307(5952):620–623, February 1984. ISSN 1476-4687. doi: 10.1038/307620a0.
- J. B. Shepherd, J. F. Tomblin, and D. A. Woo. Volcano-seismic crisis in montserrat, west indies, 1966-67. *Bulletin Volcanologique*, 35(1):143–162, March 1971. ISSN 1432-0819. doi: 10.1007/bf02596813.
- H. D. Sinclair and P. A. Cowie. Basin-floor topography and the scaling of turbidites. *The Journal of Geology*, 111(3):277–299, May 2003. ISSN 1537-5269. doi: 10.1086/373969.
- Peter J. Talling. On the frequency distribution of turbidite thickness. *Sedimentology*, 48(6):1297–1329, December 2001. ISSN 1365-3091. doi: 10.1046/j.1365-3091.2001.00423.x.

- Y. Tamura. Some geochemical constraints on hot fingers in the mantle wedge: evidence from ne japan. *Geological Society, London, Special Publications*, 219(1): 221–237, January 2003. ISSN 2041-4927. doi: 10.1144/gsl.sp.2003.219.01.11.
- Y. Tamura, K. Tani, Q. Chang, H. Shukuno, H. Kawabata, O. Ishizuka, and R. S. Fiske. Wet and dry basalt magma evolution at torishima volcano, izu-bonin arc, japan: the possible role of phengite in the downgoing slab. *Journal of Petrology*, 48 (10):1999–2031, August 2007. ISSN 0022-3530. doi: 10.1093/petrology/egm048.
- Y. Tamura, C.J. Busby, P. Blum, G. Guèrin, G.D.M. Andrews, A.K. Barker, J.L.R. Berger, E.M. Bongiolo, M. Bordiga, S.M. DeBari, J.B. Gill, C. Hamelin, J. Jia, E.H. John, A.-S. Jonas, M. Jutzeler, M.A.C. Kars, Z.A. Kita, K. Konrad, S.H. Mahony, M. Martini, T. Miyazaki, R.J. Musgrave, D.B. Nascimento, A.R.L. Nichols, J.M. Ribeiro, T. Sato, J.C. Schindlbeck, A.K. Schmitt, S.M. Straub, M.J. Vautravers, , and Y. Yang. *Expedition 350 summary*. International Ocean Discovery Program, May 2015. doi: 10.14379/iodp.proc.350.101.2015.
- B. Taylor. *Rifting and the Volcanic-Tectonic Evolution of the Izu-Bonin-Mariana Arc*. Ocean Drilling Program, August 1992. doi: 10.2973/odp.proc.sr.126.163.1992.
- J. Trofimovs, L. Amy, G. Boudon, C. Deplus, E. Doyle, N. Fournier, M.B. Hart, J.C. Komorowski, A. Le Friant, E.J. Lock, C. Pudsey, G. Ryan, R.S.J. Sparks, and P.J. Talling. Submarine pyroclastic deposits formed at the soufrière hills volcano, montserrat (1995-2003): What happens when pyroclastic flows enter the ocean? *Geology*, 34(7):549, 2006. ISSN 0091-7613. doi: 10.1130/g22424.1.
- J. Trofimovs, C. Foster, R. S. J. Sparks, S. Loughlin, A. Le Friant, C. Deplus, L. Porritt, T. Christopher, R. Luckett, P. J. Talling, M. R. Palmer, and T. Le Bas. Submarine pyroclastic deposits formed during the 20th may 2006 dome collapse of the soufrière hills volcano, montserrat. *Bulletin of Volcanology*, 74(2):391–405, September 2011. ISSN 1432-0819. doi: 10.1007/s00445-011-0533-5.
- Jessica Trofimovs, R. Stephen John Sparks, and Peter J. Talling. Anatomy of a submarine pyroclastic flow and associated turbidity current: July 2003 dome collapse, soufrière hills volcano, montserrat, west indies. *Sedimentology*, 55(3): 617–634, November 2007. ISSN 1365-3091. doi: 10.1111/j.1365-3091.2007.00914.x.
- Donald L. Turcotte. ractals in geology: What are they and what are they good for? *GSA Today*, 1991.

Eli Tziperman, Maureen E. Raymo, Peter Huybers, and Carl Wunsch. Consequences of pacing the pleistocene 100 kyr ice ages by nonlinear phase locking to milankovitch forcing. *Paleoceanography*, 21(4), November 2006. ISSN 1944-9186. doi: 10.1029/2005pa001241.

Jan A. van Dam, Hayfaa Abdul Aziz, M. Ángeles Álvarez Sierra, Frederik J. Hilgen, Lars W. van den Hoek Ostende, Lucas J. Lourens, Pierre Mein, Albert J. van der Meulen, and Pablo Pelaez-Campomanes. Long-period astronomical forcing of mammal turnover. *Nature*, 443(7112):687–691, October 2006. ISSN 1476-4687. doi: 10.1038/nature05163.

Maryline Vautravers, Yoshihiko Tamura, Cathy Busby, Peter Blum, Graham Andrews, Débora Nascimento, Abigail Barker, Myriam Kars, Robert Musgrave, James Gill, S. Straub, Susan DeBari, Gilles Guerin, S.H. Mahoney, Julia Ribeiro, Alexandra Yang, Alex Nichols, and Manuela Bordiga. *Data report: Pleistocene planktonic foraminiferal oxygen and carbon stable isotope records and their use to improve the age model of Hole U1436C cores recovered east of the Aogashima Volcano*. 04 2016.

B. Voight, J-C. Komorowski, G. E. Norton, A. B. Belousov, M. Belousova, G. Boudon, P. W. Francis, W. Franz, P. Heinrich, R. S. J. Sparks, and S. R. Young. The 26 december (boxing day) 1997 sector collapse and debris avalanche at soufrière hills volcano, montserrat. *Geological Society, London, Memoirs*, 21(1): 363–407, January 2002. ISSN 2041-4722. doi: 10.1144/gsl.mem.2002.021.01.17.

R. G. Walker. Turbidite sedimentary structures and their relationship to proximal and distal depositional environments. *Journal of Sedimentary Research*, 37(1):25–43, March 1967. ISSN 1527-1404. doi: 10.1306/74d71645-2b21-11d7-8648000102c1865d.

R. J. Walker, S. P. A. Gill, C. Greenfield, K. J. W. McCaffrey, and T. L. Stephens. Sensitivity of santorini eruption model predictions to input conditions. *Nature Geoscience*, 16(10):851–853, September 2023. ISSN 1752-0908. doi: 10.1038/s41561-023-01268-2.

Deborah Wall-Palmer, Maya Coussens, Peter J. Talling, Martin Jutzeler, Michael Cassidy, Isabelle Marchant, Martin R. Palmer, Sebastian F. L. Watt, Christopher W. Smart, Jodie K. Fisher, Malcolm B. Hart, Andrew Fraass, Jessica Trofimovs, Anne Le Friant, Osamu Ishizuka, Tatsuya Adachi, Mohammed Aljahdali, Georges Boudon, Christoph Breitkreuz, Daisuke Endo, Akihiko Fujinawa, Robert Hatfield,

- Matthew J. Hornbach, Kyoko Kataoka, Sara Lafuerza, Fukashi Maeno, Michael Manga, Michael Martinez-Colon, Molly McCanta, Sally Morgan, Takeshi Saito, Angela L. Slagle, Adam J. Stinton, K. S. V. Subramanyam, Yoshihiko Tamura, Benoit Villemant, and Fei Wang. Late pleistocene stratigraphy of iodp site u1396 and compiled chronology offshore of south and south west montserrat, lesser antilles. *Geochemistry, Geophysics, Geosystems*, 15(7):3000–3020, July 2014. ISSN 1525-2027. doi: 10.1002/2014gc005402.
- Sebastian Watt, Peter Talling, and James Hunt. New insights into the emplacement dynamics of volcanic island landslides. *Oceanography*, 27(2):46–57, June 2014. ISSN 1042-8275. doi: 10.5670/oceanog.2014.39.
- Tao Yang, Xixi Zhao, Katerina Petronotis, Mark J. Dekkers, and Huiru Xu. Anisotropy of magnetic susceptibility (ams) of sediments from holes u1480e and u1480h, iodp expedition 362: Sedimentary or artificial origin and implications for paleomagnetic studies. *Geochemistry, Geophysics, Geosystems*, 20(11): 5192–5215, November 2019. ISSN 1525-2027. doi: 10.1029/2019gc008721.
- S. R. Young, B. Voight, J. Barclay, R. A. Herd, J.-C. Komorowski, A. D. Miller, R. S. J. Sparks, and R. C. Stewart. Hazard implications of small-scale edifice instability and sector collapse: a case history from soufrière hills volcano, montserrat. *Geological Society, London, Memoirs*, 21(1):349–362, January 2002. ISSN 2041-4722. doi: 10.1144/gsl.mem.2002.021.01.16.
- Rui Zhang, Xiaojuan Li, Yong Xu, Jianxing Li, Lu Sun, Leping Yue, Feng Pan, Feng Xian, Xiaohao Wei, and Yuge Cao. The 173-kyr obliquity cycle pacing the asian monsoon in the eastern chinese loess plateau from late miocene to pliocene. *Geophysical Research Letters*, 49(2), January 2022. ISSN 1944-8007. doi: 10.1029/2021gl097008.

Chapter 5

Conclusion

This project developed a robust framework for the analysis of temporal distribution of eruptions, building on the concept of point processes, leveraging its well established base of statistical methods. Providing formal treatment of the data and the questions of interest enabled the improvement of methods present in the literature.

In the case of detection of periodicities, it was possible to develop a procedure more general, precise and with better performance than the previously used ones. Additionally, analysis of simulated data improves the robustness of results.

The goodness-of-fit test, the main methodological advancement in this work, was motivated by limitations of existing procedures and fills a long-standing gap in the literature. Along with the development of models combining point process and continuous time series, this procedure offers a flexible and statistically sound method for the analysis of the distribution of eruptive events.

The effectiveness of our framework was demonstrated in the analysis of real data, supporting the evidence for the relation between climate and volcanism. For the Izu-Bonin arc, not only previous observations of periodicity coinciding with the Milankovitch cycle of eccentricity were corroborated, but the new goodness-of-fit test showed a direct correlation between occurrence of explosive eruptions and the $\delta^{18}O$ climate proxy.

Still, there are several possible expansions of this project, which can be roughly divided in two categories. The first is application centered, and involves using the already developed tools to analyze new data sets. The second is focused on the development of the methodology, by creating new tests or extending the existing ones to new situations. We conclude with some ideas that were already considered and the challenges that must still be overcome.

5.1 Analysis of additional eruption records

An immediate extension of Section 2 would be to test the hypothesis of correlation between deglaciation and occurrence of eruption in a much broader array of data sets to determine if the findings from Section 2.5 are a local phenomenon or if they can be observed globally. The analyzes would then be done either for a large global compilation record or for several local records covering many geological settings. The main challenge, however, is the careful curation of the data.

For the analysis of local records, the main difficulty is finding records with reliable dating, consistent recovery rate, and large enough number of events (≈ 100) for our test to be reliable. Additionally, the interval covered in the records should be comparable, which would allow drawing conclusions from the observation of multiple processes.

For global compilation records, except for the number of events, the difficulties mentioned above still apply. The periods covered by each of the individual data sets as well as their recovery rates may vary greatly, introducing biases to the analysis that must be accounted for. The Pacific Ring of Fire compilation presented in Kutterolf et al. (2013) is a good example of a carefully assembled data set accounting for these issues, however, a large bias towards recent events can be observed, due to the recent tephra layers being more likely to be preserved as well as the varying intervals covered by the local datasets.

5.2 Models including underreporting

It is a well known issue that eruption records may present different degrees of underreporting, depending on location, eruption magnitudes, and age of events (Simkin, 1993). Models for underreporting have been proposed by Coles and Sparks (2006) and Deligne et al. (2010) consisting, essentially, of a presence function $p(t)$ representing the probability of an eruption at instant t to actually be recorded.

Assume (t_1, t_2, \dots) is a point process over $[0, T]$ with conditional intensity function $\lambda(t)$. The presence of underreporting means that (t_1, t_2, \dots) is not directly observable, instead, each t_i has a probability $p(t_i)$ to be included in the record and, therefore, we only have access to a subset of the events. However, it can be shown that this new process $N_p(t)$, to which we have access to, has conditional intensity function $p(t)\lambda(t)$.

If both $\lambda(t)$ and $p(t)$ are parametric functions, then, in principle, it would be possible to adapt the goodness-of-fit test (Section 2.3) to this context. This only

works, however, for Poisson processes. For any process in which the intensity function depends on past events, it is unclear how to properly perform the estimation of parameters with incomplete data or how to circumvent this issue.

5.3 Test for marked point processes

In many eruption records, not only the age of the eruptions is listed, but also the magnitude. The record, in this case, is not a list of times, but a list of time-magnitude pairs $(t_1, m_1), (t_2, m_2), \dots, (t_N, m_N)$, and can be modeled as marked point processes (Wang et al., 2019).

In the simplest case, (t_1, \dots, t_N) follow a Poisson process and m_1, \dots, m_N are i.i.d. random variables, therefore, timings and magnitudes are independent of each other. A possible strategy for a goodness-of-fit test could be to perform two tests separately, one for the timings, as in Section 2.3 or 3.1, and one for the magnitudes, perhaps using the same statistic as in the mentioned sections, returning two p-values p_t and p_m . The final p-value of the test could then be $p_t \cdot p_m$, although additional studies are necessary to confirm its consistency.

For most applications, however, it is assumed that timings and magnitudes interact with each other, making models and, consequently, the algorithms for estimation and testing, much more complex.

References

- Stuart G. Coles and R. Stephen J. Sparks. Extreme value methods for modelling historical series of large volcanic magnitudes. In *Statistics in Volcanology*, pages 47–56. The Geological Society of London on behalf of The International Association of Volcanology and Chemistry of the Earth's Interior, 2006. doi: 10.1144/iavcei001.5.
- N. I. Deligne, S. G. Coles, and R. S. J. Sparks. Recurrence rates of large explosive volcanic eruptions. *Journal of Geophysical Research*, 115(B6), jun 2010. doi: 10.1029/2009jb006554.
- Steffen. Kutterolf, Marion Jegen, Jerry X. Mitrovica, Tom Kwasnitschka, Armin Freundt, and Peter J. Huybers. A detection of milankovitch frequencies in global volcanic activity. *Geology*, 41(2):227–230, feb 2013. doi: 10.1130/g33419.1.
- T Simkin. Terrestrial volcanism in space and time. *Annual Review of Earth and*

Planetary Sciences, 21(1):427–452, May 1993. ISSN 1545-4495. doi: 10.1146/annurev.ea.21.050193.002235.

Ting Wang, Matthew Schofield, Mark Bebbington, and Koji Kiyosugi. Bayesian modelling of marked point processes with incomplete records: Volcanic eruptions. *Journal of the Royal Statistical Society Series C: Applied Statistics*, 69(1):109–130, October 2019. ISSN 1467-9876. doi: 10.1111/rssc.12380.

Erklärung

Hiermit erkläre ich, dass ich die vorliegende Dissertation – abgesehen von der Beratung durch meinen Betreuer Herrn Prof. Dr. Mathias Vetter – nach Inhalt und Form eigenständig angefertigt habe. Dabei habe ich die Regeln guter wissenschaftlicher Praxis der Deutschen Forschungsgemeinschaft eingehalten. Die Arbeit hat weder ganz noch zum Teil einer anderen Stelle im Rahmen eines Prüfungsverfahrens vorgelegen und ist weder ganz noch zum Teil veröffentlicht oder zur Veröffentlichung eingereicht worden.

José Carlos Fontanesi Kling. Kiel, 17. Januar 2025